University of Strathclyde
Department of
Electronic and Electrical Engineering

Design and Control of Photovoltaic Systems in Distributed Generation

by

Bader Nasser Alajmi
B.Sc., M.Sc.

A thesis presented in fulfilment of the requirements for the degree
of Doctor of Philosophy

January 2013

Abstract

The design and control of a photovoltaic system for stand-alone and grid-connected applications is accomplished. The stand-alone photovoltaic system is designed to improve the photovoltaic output power by using a new maximum power point tracking method. The proposed algorithm improves the hill climbing search method by fuzzifying the rules, thereby eliminating some of the disadvantages associated with the method. Modification of the proposed maximum power point tracker is proposed to increase photovoltaic system performance during partially shaded operation. Also, a new mathematical model is derived to represent the behaviour of the photovoltaic system characteristic under partial shading conditions. A single-phase single-stage current source inverter based photovoltaic system for grid connection is proposed. This system utilizes transformerless single-stage conversion for tracking the maximum power point and interfacing the photovoltaic array to the grid. The maximum power point is achieved with the proposed maximum power point tracking method. A proportional-resonant controller is used to control the current injected into the grid. Simulation and experimental results validate the proposed systems.

Dedication

To my mother, my father, my wife and my children

Acknowledgements

Many thanks to my supervisors Prof. Barry W. Williams, Prof. Stephen J. Finney, and Dr. Khaled H. Ahmad for their extensive guidance, support and help throughout my PhD period. Also their comments and suggestions during the writing of this thesis are highly appreciated.

I also would like to thank Dr. Grain P. Adam for his support and advice throughout my PhD study.

I would like to acknowledge staff and colleagues in the Department of Electronic and Electrical Engineering in Strathclyde University for their assistance and support during the years of research.

Finally, a heartfelt gratitude goes to my family for all the sacrifices they had to make and for their support and encouragement.

Bader Nasser Alajmi
December 2012

List of Symbols

A	dimensionless junction material factor
C	capacitance (F)
D	duty cycle
I_{dc}	dc link current (A)
I_g	grid current (A)
I_o	reverse saturation current (A)
I_{ph}	light generated current (A)
I_{pv}	photovoltaic array output current (A)
I_{sc}	photovoltaic array open circuit current (A)
k	Boltzmann constant ($1.38\text{x}10^{-23} J/K$)
K_i	integral gain
K_p	proportional gain
L	inductance (H)
M	modulation index
n_s^s	number of cells connected in series for shaded modules
n_s^{us}	number of cells connected in series for unshaded modules
n_p	number of cells connected in parallel
n_s	number of cells connected in series
P	photovoltaic array output power (W)
P_m	global maximum power point (W)

q	electron charge ($1.6\text{x}10^{-19}C$)
R_s	solar cell series resistances (Ω)
R_{sh}	solar cell shunt resistances (Ω)
T	temperature (K)
V_{dc}	dc link voltage (V)
V_g	grid voltage (V)
V_{oc}	photovoltaic array short circuit voltage (V)
V_{pv}	photovoltaic array output voltage (V)
λ	sun radiation levels (W/m^2)
λ^s	sun radiation levels for shaded PV module (W/m^2)
λ^{us}	sun radiation levels for unshaded PV module (W/m^2)
ω	angular frequency (rad/s)

List of Abbreviations

ac	Alternating Current
COA	Centre of Area Algorithm
CPWM	Carrier Based Pulse-Width Modulation
CSI	Current Source Inverter
dc	Direct Current
FLC	Fuzzy Logic Controller
IEEE	Institute of Electrical and Electronics Engineers
IGBT	Insulated Gate Bipolar Transistor
M2I	Modular Multilevel Inverter
MPP	Maximum Power Point
MPPT	Maximum Power Point Tracker (Tracking)
NB	Negative Big
NM	Negative Medium
NS	Negative Small
P&O	Perturbation and Observation
PB	Positive Big
PI	Proportional Integral
PM	Positive Medium
PR	Proportional-Resonant
PS	Positive Small
PV	Photovoltaic (cell)

PWM	Pulse-Width Modulation
SPWM	Sinusoidal Pulse-Width Modulation
STC	Standard Test Conditions
THD	Total Harmonic Distortion
VSI	Voltage Source Inverter

Preface

Renewable energy source development has attracted research attention, especially as a consequence of the energy crisis and environmental issues such as global warming and pollution. There has been significant progress in the development of renewable energy sources such as combined heat and power (CHP) systems, solar photovoltaic (PV) modules, small wind turbines, and heat and electricity storage, where controllable loads are expected to play a significant role in future electricity supply. PV systems are considered to be an important renewable energy source, because they are considered to be an effective and efficient solution to environmental problems. Unfortunately PV systems suffer from three main problems: high fabrication cost, low conversion efficiency especially under variable weather conditions, and the nonlinearity between the PV array output power and current. In this thesis, possible solutions for photovoltaic systems are proposed.

Chapter one presents general facts on photovoltaic system such as history, potential, economy, environmental impact, applications, reliability, and standards.

Chapter two is a literature survey of photovoltaic system configurations, with a detailed description of the photovoltaic cell, power electronics components, and the control strategies of stand-alone and grid-connected photovoltaic systems.

Chapter three investigates structures and features of conventional hill climbing maximum power point tracking, and then proposes a new fuzzy logic controller for maximum power point tracking of photovoltaic systems under varying weather conditions. Simulation and experimental results are provided to demonstrate the validity of the proposed fuzzy logic based controller.

In chapter four, a modified fuzzy-logic controller for maximum power point tracking is proposed to increase PV system performance during partially shaded operation. A new mathematical model of a PV system under partial shading conditions is proposed. Simulation and practical results verify the proposed controller.

In chapter five, a single-phase single-stage current source inverter based photovoltaic system for grid connection is developed. In this system, current source modulation techniques and methods for mitigating oscillation in the dc link inductor are proposed.

Simulation and practical results are provided to validate and confirm the dynamic performance and power quality of the proposed system.

Finally, chapter six presents the thesis general conclusion, the author's contribution, and suggestions for future research.

Table of contents

Chapter 3 Modified Hill-Climbing Method for Maximum Power Point Tracking in Standalone Photovoltaic Systems

Chapter 4 A Maximum Power Point Tracking Technique for Partially Shaded Photovoltaic Systems

Chapter 5 Single-Phase Single-Stage Transformerless Grid Connected PV System

Chapter 6 Conclusion

Appendices

Chapter 1

Introduction

Electric energy consumption has been growing dramatically over the past few years to meet the energy needs related to global population and high economic growth. The global electrical demand is projected to increase by 2.2% per year on average between 2008 and 2035 [1.1]. Currently, 87% of the world's power generation is based on burning fossil fuels, which results in increased greenhouse gas emissions [1.2]. Therefore, the development of renewable energy sources has attracted the attention of researchers. There has been significant progress in the development of renewable energy sources, such as combined heat and power (CHP) applications, solar photovoltaic (PV) modules, small wind turbines, and heat and electricity storage, where controllable loads are expected to play a significant role in future electricity supplies. Photovoltaic systems are considered one of the most efficient and well-accepted renewable energy sources, due to their suitability in distributed generation, mobile applications, transportation, and satellite systems.

1.1 Background and development of the photovoltaic system

The history of the PV system goes back to the 17th century, when a French physicist, Alexander-Edmond, came across the PV effect. In 1883, American inventor Charles Fritts developed the first PV cell by coating the semiconductor material selenium with a thin layer of gold; solar energy conversion efficiency was only 1%. Then, in 1954, Chapin *et al.*, at Bell Laboratories invented the first crystalline silicon solar PV cell, with 6% efficiency. The first practical application of solar PV technology took place in the space satellite projects in the 1960s. Nowadays, solar PV panels are the key component of satellite systems, providing them with a maintenance-free power supply for life [1.3]. The improvement of solar PV technology over the last 50 years, as well as the pioneering success of space satellite projects have encouraged researchers and investors to use solar PV technology as an alternative to generating electricity from burning fossil fuel. Additionally, the solar PV system has no harmful emission, noise pollution, or polluting gases; therefore, it is considered to be a good environmental option in the micro-generation of domestic electricity. Most countries around the world are encouraging their inhabitants to take part in green initiatives, by offering financial incentives. Consumers who generate their own power are most likely to modify their energy consumption by making their homes environmentally friendly and fuel efficient.

1.1.1 Photovoltaic power potential

PV power use has grown significantly as a source of practical renewable energy during the past decade. Increasing the use of PV systems as an alternative to conventional energy resources results in a considerably decrease in green-house gas emissions. The cumulative growth rate of PV power in the countries that are registered with The International Energy Agency of Photovoltaic Power Systems (IEA PVPS) programme is illustrated in Figure 1.1 [1.4]. According to IEA PVPS, the cumulative rate of standalone PV systems was 78 MW in 1993, whereas the standalone cumulative rate was 980 MW in 2010. On the other hand, the cumulative rate of grid-connected PV systems was 27 MW in 1993, and increased to 33,973 MW in 2010. These indicate standalone and grid connected PV systems have grown by 902 MW and 33,946 MW respectively. In conclusion, the potential of PV system has increased significantly in both standalone and grid-connected applications during the last two decades

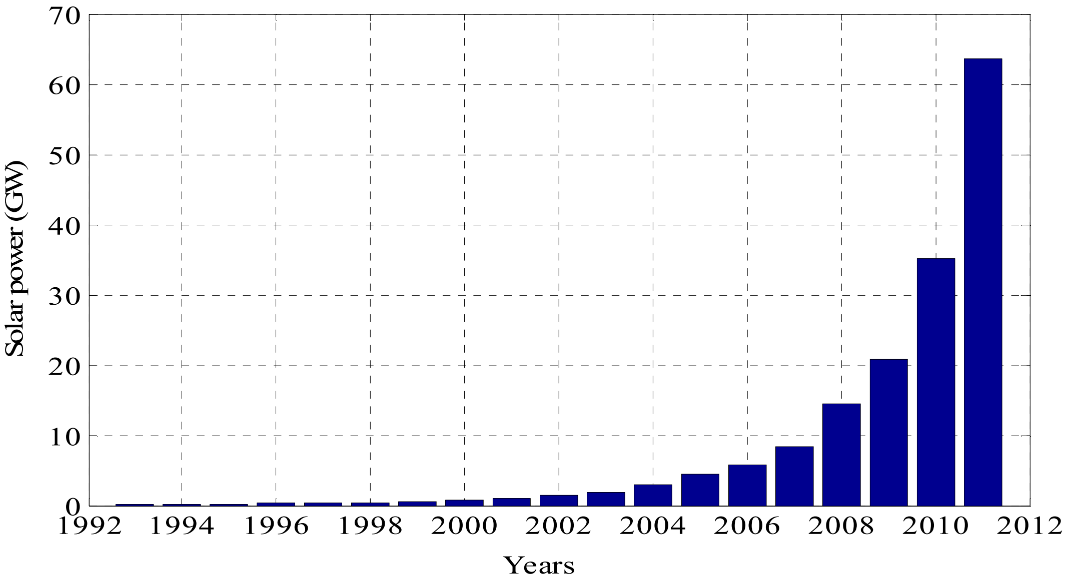

Figure 1.1. Growth rate of PV power installation in IEA PVPS countries.

1.1.2 Economics of photovoltaic energy

Due to government support and other financial incentives, the cost of PV modules has experienced a large reduction in the past few decades. According to [1.5], the average price per Watt of the PV module decreased from \$10/W in 1980 to \$2.36/W in 2010. The price of the PV module depends mainly on two factors; manufacture cost and the efficiency of converting sunlight into electricity. From the manufacturer point of view, the manufacture cost of the PV module is the main factor that determines the PV module selling price that meets the required profit margin. Increasing PV module conversion efficiency results in reducing the overall cost of the PV system, as electricity production requires less installation area per watt and reduces the cost of installation equipment such as wiring and racking. Currently, the installation cost of PV systems is considered to be high, compared with other sustainable energy sources, such as wind energy [1.6]. However, in the long term, the PV system is economically viable when compared with the wind energy system, as it requires almost no maintenance and has a long working life, as well as flexibility at the installation location.

1.1.3 Environmental impact

The solar panel derives its energy from the sun; therefore, it releases no carbon dioxide or any greenhouse gases, and therefore, does not contribute to global warming. Greenhouse gas emissions could be produced during the production stage of the PV module; however, the amount of greenhouse gas emissions during PV panel manufacture is much less than those resulting from conventional power. PV emits only 21.65 gCO_2/kWh, whereas conventional thermal power emits 900 gCO_2/kWh [1.7]. At the end of the PV module's lifetime, it is possible to recycle it and use the raw materials to produce a new PV module. In this case, the energy used to produce the PV cell is reduced. Unlike other energy sources, a PV system is a static device, operates in a silent mode, and produces no noise or air pollution; therefore, it can be safely used in residential areas.

1.1.4 Photovoltaic energy application

Photovoltaic systems operate in two different modes: standalone and grid-connected.

a. Standalone system

Standalone PV systems are operated independently of the utility grid. Therefore, the major applications of standalone PV systems are in remote or isolated areas where utility power is unavailable or costly. Examples of the most popular standalone PV system applications are satellites, space stations, communication sites, transportation, emergency telephones, traffic signs, cathodic protection, and water pumps [1.8]. In most cases, standalone PV systems require storage batteries to supply electricity continuously during the night or at times of low sunlight level. In the last few years, the development and installation of standalone PV systems has dramatically decreased, because most political investment goes to grid-connected technology. According to [1.9], of the total installed PV systems in IEA PVPS countries during 2010, less than 0.7% were installed in standalone PV systems.

b. Grid-connected system

Grid-connected PV systems are designed to operate in parallel with the utility grid. The grid-connected PV system can operate as a distributed generation or centralized power plant. In distributed generation, customers generate their own power to reduce their dependency on the grid or inject power into the grid. On the other hand, the centralized PV power station provides bulk power to reduce oil dependency and greenhouse gases [1.10].Currently, the largest PV power plant is located in China with a total capacity of 200 MW. However, different projects under construction in the USA aim to break this record by producing 550 MW [1.11]. Unlike other renewable energy sources, PV systems can be utilized safely as roof-mounted PV power plants. The largest roof-mounted PV power plant is located in Belgium, with a total capacity of 13 MW [1.11].

1.1.5 Development

PV technology has the potential to become a major worldwide source of power generation. In terms of installed capacity, PV technology is ranked the third most important renewable energy, after hydro and wind power [1.12]. In 2011, the worldwide PV capacity was around 70 GW, with an average growth rate of 58% per year [1.6]. Europe is the world's largest PV energy producer, with a total installed capacity of 51 GW. Japan comes next in the ranking, with total installed capacity of 5 GW, followed by USA (4.4 GW), China (3.1 GW), Australia (1.3GW), and India (0.46 GW).

Recently, many developing countries in the Middle East, Southeast Asia, Africa, and Latin America have installed PV systems to take advantage of the large sunbelt in their region [1.12]. According to European Photovoltaic Industry Association (EPIA), the countries in the large sunbelt region could have 1100 GW installed capacity by the year 2030.

1.1.6 Photovoltaic energy in the UK

Due to unpredictable weather conditions and the northerly latitude location, it is expected that PV systems are not suitable for the UK. However, the modern PV system can operate efficiently without having large amounts of sunlight [1.13]. In the past few years, installations of PV systems have increased significantly in the UK, because of extra support from policy investment [1.14]. The total installed PV energy capacity increased from 10.9 MW in 2005 to 1 GW in 2012 [1.15]. In April 2010, a system of Feed-In Tariff was introduced to provide support for PV and other renewable energy sources. The system supports householders and communities in generating their own power with regular payments through their energy supplier. The UK government established this system to increase the total renewable energy level from 2% in 2009 to 15% in 2020 [1.16]. According to the Feed-In Tariff, approximately 22,548 PV sites were reported in the UK, with 21,032 in England, 915 in Wales and 601 in Scotland.

1.2 Photovoltaic energy generation challenges

Due to the many advantages that can be gained from renewable energy sources, their development has increased significantly in recent years [1.17]. Solar energy, which is widely used as power plant in the MW range and distributed generation in the kW range, presents many challenges in terms of reliability, robustness, cost, and effect on the grid. Solar energy performance can be improved by power electronics devices. To achieve higher efficiency and better stability, solar energy is controlled by power electronics devices in grid-connected or islanded modes.

1.2.1 Reliability

In general, a PV system consists of a PV module, dc/dc converter, energy storage devices, dc/ac inverter, and a system controller. The reliability of the PV system depends on the quality of those components and the installation region. The PV modules are the most reliable part of the PV system; they required no maintenance and have a lifespan of up to 30 years [1.18]. In some PV system applications, such as standalone modes and grid-connected modes with critical loads, the use of energy storage devices and a charger controller are required to continually supply the load with high quality power [1.19-21]. Lead acid and nickel (Ni-Cd or Ni-HD) type batteries are commonly used in PV systems. The batteries can greatly increase the cost and decrease the overall system reliability; therefore, they have to be properly selected and managed to increase their lifetime [1.22]. According to [1.18], the power electronics devices and controllers are the most susceptible components in PV systems. For example, the Florida Solar Energy Center [1.23] has recorded 213 failure events on 130 grid-connected PV systems from 1999 to 2003, and the recorded data indicates that 65% of those failures are mainly caused by inverters. Logically, the reliability of power electronics components in PV systems is poor, because they are directly affected by any faulty condition in the grid or during maintenance. Therefore, protection devices must be carefully selected to prevent any failure of the power circuit. Moreover, the power electronics device controllers play a major role in their reliability, by using islanding detection and maximum power point tracking (MPPT).

1.2.2 Efficiency

The efficiency of PV systems depends on three major components: PV panel, inverter, and MPPT controller. Transformer efficiency could be added to the list for grid-connected applications. In the past, the PV panel could only convert 1-2% of the sun's radiation into electric energy, because most of the sunlight was absorbed or reflected by the solar cell materials. However, the solar cell industry has advanced significantly in the last few decades, and the conversion efficiency of the modern solar cell varies from one solar cell technology to another. Table 1.1 shows the conversion efficiencies of the solar cell technologies [1.5]. Researchers are aiming to increase the solar cell efficiency to exceed 50% [1.24].

Table 1.1. The efficiency of all solar cell types.

Solar cell type	Conversion efficiency %
multi-junction	42.3
crystalline silicon	15-25
thin film	10-20
organic cells	5
dye-sensitized	10

Single and two-stages are commonly used power electronic topologies in PV systems. In a single stage, the PV system utilizes a single conversion unit; a dc/ac inverter to track the maximum power point and interface the PV system to the grid. In such a topology, the maximum PV power is delivered into the grid with high efficiency, small size, and low cost. In a two-stage topology, the PV system utilizes two conversion stages; a dc/dc converter, for boosting the PV output voltage and tracking the maximum power point, and a dc/ac inverter, for interfacing the PV system to the grid or loads. In this topology, a high-voltage PV array is not necessarily required, due to the amplification stage. However, the two-stage grid-connected system suffers from lower efficiency, higher cost, and larger size.

The PV array power and current characteristics are highly nonlinear and are affected by variations in irradiance and temperature. Therefore, MPPT is required to handle such problems and to ensure that the PV system is operating at the maximum power point (MPP) [1.25]. Many different MPPT techniques have been proposed [1.26]. The existing techniques vary in simplicity, accuracy, time response, popularity, cost, and other technical aspects. Moreover, the PV system suffers from a major disadvantage, which is the nonlinearity between the output voltage and current, especially under partially shaded conditions [1.27]. During partially shaded conditions, the PV system's characteristic curve has multiple peaks. Therefore, conventional MPPT such as hill climbing, incremental conductance, and ripple correlation, could miss the global maximum point [1.26, 28-30]. A study of partial shadow conditions in [1.31] shows that using conventional MPPT during partial shadows could result in significant loss of PV output power. Therefore, many researchers have investigated improvements in tracking efficiency. Figure 1.2 shows the three major components that contribute to the overall PV system efficiency.

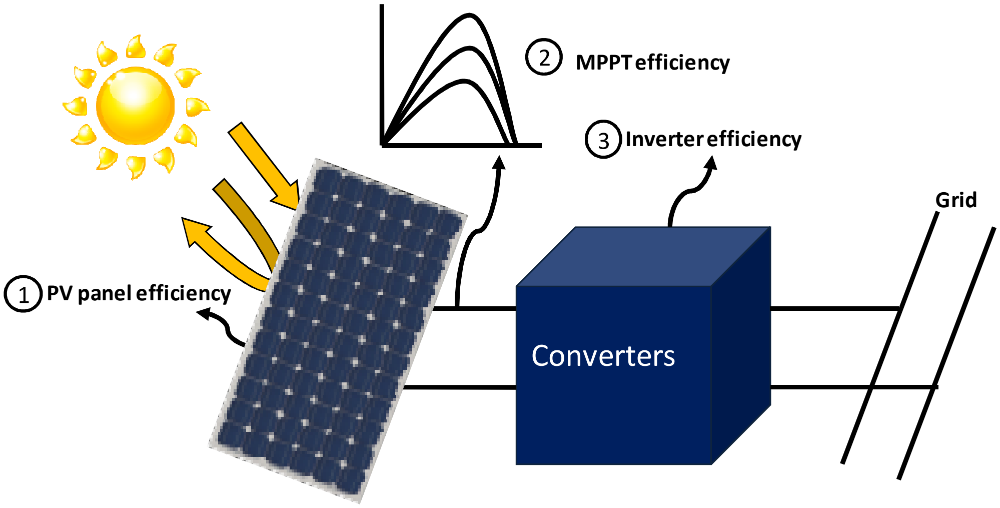

Figure1. 2. The three major components that contribute to the overall PV system efficiency.

1.2.3 Transmission and grid integration

Different methods have been proposed to interface a grid-connected PV system to the grid. The methods include a centralized inverter, a string inverter, and a multi-string inverter [1.7]. The centralized inverter [1.32], which utilises strings of PV modules connected in parallel, using a string diode and then interfacing the grid through a dc/ac inverter, is considered to be the most economically scaled method. However, it suffers from a number of drawbacks, such as difficulty of tracking the optimal MPP, the need for high dc voltage wire, lack of expandability options, and additional power losses in the string diode. The string inverter [1.33], which utilises each PV string with its own inverter, is proposed as a way to overcome the centralized inverter drawbacks. In such technology, the economic scale is increased by adding additional inverters to each string. However, this allows MPPTs for each string, flexibility in extending the PV system, and reduced wiring dc voltage. The string inverter can be constructed using a single stage or two stages. In the single-stage PV system, the PV maximum power is delivered to the grid with high efficiency, a small foot-print and low cost. However, to fulfil the grid requirement, this topology requires either a step-up transformer, which reduces system efficiency and increases cost, or a PV array with a high dc voltage, which suffers from hotspots during partial shadowing and increased chance of current leakage between the panel and the system ground through parasitic capacitances. Moreover, inverter control is complicated, because the control objectives such as MPPT, power factor correction, and harmonic reduction, are simultaneously considered. Large electrolytic capacitors are required to decouple the PV string from the single-phase output power. In two-stage inverters, also called a multi-string inverter [1.34], the PV system is constructed using two conversion stages: the dc/dc converter for boosting the PV output voltage and tracking the MPP, and the dc/ac inverter for interfacing the PV system to the grid. In this topology, the dc/dc input stage decouples the PV modules from the output power ripple and allows the system to operate over a wide voltage range. Also, a high-voltage PV array is not essential, due to the amplification stage. However, the two-stage grid-connected system suffers from lower efficiency, higher cost, and larger size.

1.2.4 Grid code requirement

The penetration of the PV grid-connected system has been impressive in the last few years. The total capacity of PV systems installed globally reached 70 GW in 2011, with an increase of 41% over 2010 [1.35]. Therefore, guidelines for equipment manufacturers, operation, and installation must be provided to ensure the safety and reliability of the network. In most countries, local regulations are imposed by the utility or the government. However, many organizations that deal with PV code and safety standards are working towards imposing grid requirement standards that can be adapted by different countries [1.36]. There are many organizations that deal with PV code and safety standards; however, the most relevant organizations are The Institute of Electrical and Electronics Engineers (IEEE) and International Electrotechnical Commission (IEC) [1.37]. Examples of an IEEE PV standard and an IEC PV standard are IEEE-1547 and IEC61727, respectively. The IEEE-1547 standard deals with interconnecting distributed generation to the electric power system, and the IEC-61727 standard is for Photovoltaic systems - Characteristics of the utility interface. A summary of IEEE1574 and IEC61727 Standards is given in Table 1.2.

Table 1.2. Summary of IEEE 1574 and IEC 61727 standards

Issue	IEEE1574	IEC61727
Nominal power	30 kW	10 kW
Harmonic current (order-h) limits	(2-10) 4.0% (11-16) 2.0% (17-22) 1.5% (23-34) 0.6% (>35) 0.3%	(3-9) 4.0% (11-15) 2.0% (17-21) 1.5% (23-33) 0.6%
	Even harmonics in these ranges shall be less than 25% of the odd harmonic limits listed.	
Maximum current THD	5.0%	
dc current injection	Less than 0.5% of rated output current	Less than 1.0% of rated output current
Frequency range for normal operation	59.3 Hz to 60.5 Hz	50±1 Hz

The design and performance of the PV interfacing unit are based on grid requirements. For example, a transformer-less PV inverter system is allowed by the utility in the United States, whereas this system configuration is restricted in some other countries [1.38]. Moreover, in some European countries, the new grid requirements adopted a three-phase mini-central PV inverter. Therefore, grid regulations play an important role in the PV system industry, and frequent regulation updating is highly recommended to accelerate the adoption of the technology.

References

[1.1] International_Nuclear_Energy_Agency, "World Energy Outlook, Executive Summary," (2010).

[1.2] B. Bose, "Global Warming: Energy, Environmental Pollution, and the Impact of Power Electronics," Industrial Electronics Magazine, IEEE, vol. 4, pp. 6-17, 2010.

[1.3] K. K. Ng, Complete Guide to Semiconductor Devices: Wiley, 2002.

[1.4] Survey report of selected IEA countries between 1992 and 2011. [Online]. Available: http://www.iea-pvps.org/.

[1.5] K. Ardani and R. Margolis, 2010 Solar Technologies Market Report, United State Dep. of Energy, November 2011.

[1.6] P. P. Dash and M. Kazerani, "Dynamic Modeling and Performance Analysis of a Grid-Connected Current-Source Inverter-Based Photovoltaic System," Sustainable Energy, IEEE Transactions on, vol. 2, pp. 443-450, 2011.

[1.7] S. B. Kjaer, J. K. Pedersen, and F. Blaabjerg, "A review of single-phase grid-connected inverters for photovoltaic modules," Industry Applications, IEEE Transactions on, vol. 41, pp. 1292-1306, 2005.

[1.8] M. A. Elgendy, B. Zahawi, and D. J. Atkinson, "Assessment of Perturb and Observe MPPT Algorithm Implementation Techniques for PV Pumping Applications," Sustainable Energy, IEEE Transactions on, vol. 3, pp. 21-33, 2012.

[1.9] TRENDS IN PHOTOVOLTAIC APPLICATIONS Survey report of selected IEA countries between1992 and 2010. [Online]. Available: http://www.iea-pvps.org/.

[1.10] Sun bridge Solar. [Online]. Available: http://sunbridgesolar.com/pacific-northwest-solar/solar-farms/.

[1.11] PV Resources. [online]. Available:http://www.pvresources.com/PVPowerPlants/LargestPVRoofs.aspx.

[1.12] Global Market Outlook for Photovoltaics until 2016, European Photovoltaic Industry Association (EPIA), Brussels, 2012, http://files.epia.org/files/Global-Market-Outlook-2016.pdf.

[1.13] A. Stafford and S. Irvine, UK Photovoltaic Solar Energy Road Map: Centre for Solar Energy Research. [Online]. Available: https://connect.innovateuk.org/c/document_library/get_file?uuid=b5d43db3-260c-43ff-b3a8-8ae0bbf00cb6&groupId=154351.

[1.14] Solar Trade Association. [Online]. Available: http://www.solar-trade.org.uk.

[1.15] The Department of Energy and Climate Change. [Online]. Available: http://www.decc.gov.uk/.

[1.16] FEED- IN TARIFF. [Online]. Available: http://www.fitariffs.co.uk/.

[1.17] D. Tagare, Electricity Power Generation:The Changing Dimensions Wiley-IEEE Press 2011.

[1.18] G. Petrone, G. Spagnuolo, R. Teodorescu, M. Veerachary, and M. Vitelli, "Reliability Issues in Photovoltaic Power Processing Systems," Industrial Electronics, IEEE Transactions on, vol. 55, pp. 2569-2580, 2008.

[1.19] B. N. Alajmi, K. H. Ahmed, S. J. Finney, and B. W. Williams, "Fuzzy-Logic-Control Approach of a Modified Hill-Climbing Method for Maximum Power Point in Microgrid Standalone Photovoltaic System," Power Electronics, IEEE Transactions on, vol. 26, pp. 1022-1030, 2011.

[1.20] E. Serban and H. Serban, "A Control Strategy for a Distributed Power Generation Microgrid Application With Voltage- and Current-Controlled Source Converter," Power Electronics, IEEE Transactions on, vol. 25, pp. 2981-2992, 2010.

[1.21] T. F. Wu, C. H. Yang, Y. K. Chen, and Z. R. Liu, "Photovoltaic inverter systems with self-tuning fuzzy control based on an experimental planning method," in Industry Applications Conference, 1999. Thirty-Fourth IAS Annual Meeting. Conference Record of the 1999 IEEE, 1999, pp. 1887-1894 vol.3.

[1.22] J. A. Halliday, T. Markvart, and J. N. Ross, "Battery management for PV systems," Power Engineer, vol. 17, pp. 46-46, 2003.

[1.23] Florida Solar Energy Center [Online]. Available:http://www.fsec.ucf.edu/en/.

[1.24] A. Luque, "Will we exceed 50% efficiency in photovoltaics?," Journal of Applied Physics, vol. 110, pp. 031301-031301-19, 2011.

[1.25] H. Chihchiang, L. Jongrong, and S. Chihming, "Implementation of a DSP-controlled photovoltaic system with peak power tracking," Industrial Electronics, IEEE Transactions on, vol. 45, pp. 99-107, 1998.

[1.26] T. Esram and P. L. Chapman, "Comparison of Photovoltaic Array Maximum Power Point Tracking Techniques," Energy Conversion, IEEE Transactions on, vol. 22, pp. 439-449, 2007.

[1.27] G. Lijun, R. A. Dougal, L. Shengyi, and A. P. Iotova, "Parallel-Connected Solar PV System to Address Partial and Rapidly Fluctuating Shadow Conditions," Industrial Electronics, IEEE Transactions on, vol. 56, pp. 1548-1556, 2009.

[1.28] A. Safari and S. Mekhilef, "Simulation and Hardware Implementation of Incremental Conductance MPPT With Direct Control Method Using Cuk Converter," Industrial Electronics, IEEE Transactions on, vol. 58, pp. 1154-1161, 2011.

[1.29] L. Fangrui, K. Yong, Z. Yu, and D. Shanxu, "Comparison of P&O and hill climbing MPPT methods for grid-connected PV converter," in Industrial Electronics and Applications, 2008. ICIEA 2008. 3rd IEEE Conference on, 2008, pp. 804-807.

[1.30] J. W. Kimball and P. T. Krein, "Discrete-Time Ripple Correlation Control for Maximum Power Point Tracking," Power Electronics, IEEE Transactions on, vol. 23, pp. 2353-2362, 2008.

[1.31] H. Patel and V. Agarwal, "MATLAB-Based Modeling to Study the Effects of Partial Shading on PV Array Characteristics," Energy Conversion, IEEE Transactions on, vol. 23, pp. 302-310, 2008.

[1.32] C. Meza, J. J. Negroni, D. Biel, and F. Guinjoan, "Energy-Balance Modeling and Discrete Control for Single-Phase Grid-Connected PV Central Inverters," Industrial Electronics, IEEE Transactions on, vol. 55, pp. 2734-2743, 2008.

[1.33] Ma, X, A. Ki, and S. Valkealahti, "Power Losses in Long String and Parallel-Connected Short Strings of Series-Connected Silicon-Based Photovoltaic Modules Due to Partial Shading Conditions," Energy Conversion, IEEE Transactions on, vol. 27, pp. 173-183, 2012.

[1.34] K. Jung-Min, K. Bong-Hwan, and N. Kwang-Hee, "Grid-Connected Photovoltaic Multistring PCS With PV Current Variation Reduction Control," Industrial Electronics, IEEE Transactions on, vol. 56, pp. 4381-4388, 2009.

[1.35] Renewables 2012, Global Status Report [Online]. Available: http://www.map.ren21.net/GSR/GSR2012.pdf.

[1.36] J. Wiles and W. Bower, "Codes, standards, and PV power systems. A 1996 status report," in Photovoltaic Specialists Conference, 1996., Conference Record of the Twenty Fifth IEEE, 1996, pp. 1409-1412.

[1.37] "IEEE Recommended Practice for Qualification of Concentrator Photovoltaic (PV) Receiver Sections and Modules," IEEE Std 1513-2001, p. i, 2001.

[1.38] R. Teodorescu, M. Liserre, and P. Rodríguez, Grid Requirements for PV, 1 ed.: Wiley-IEEE Press, 2011.

Chapter 2

Photovoltaic system configuration

This Chapter presents a literature survey of photovoltaic system configurations. The survey starts with a detailed description of the photovoltaic cell, module, array, and the characteristic curve. The power electronics components and the control strategies of standalone and grid-connected photovoltaic systems are presented. The integration options of grid-connected photovoltaic system are discussed to clarify their power electronics topologies. The types of dc/ac inverters that can be used on either single-stage or two-stage topologies are presented.

2.1 Photovoltaic cell, module and array

A photovoltaic system consists of a solar array which is a group of series-parallel connected modules, where the basic component within the module is solar cells [2.1]. To design a solar module, the solar cell's power is measured and then connected in series based on the desired output voltage. Figure 2.1 represents a photovoltaic system.

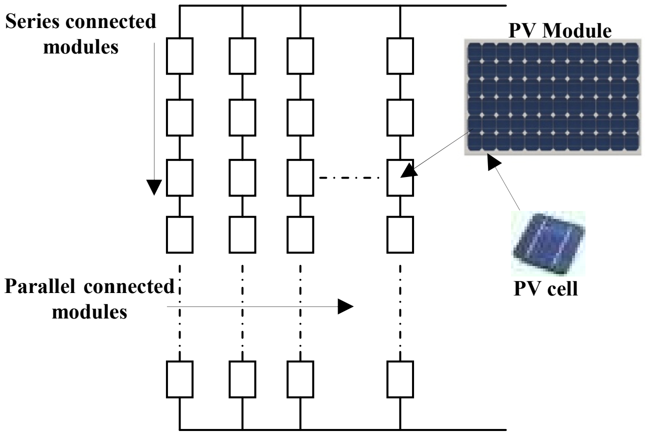

Figure 2.1. PV array system.

2.1.1 Solar cell

The solar cell, which is the basic building block of the PV system, consists of semiconductor materials. The semiconductors behave like conductors when exposed to light or heat, but at low temperature the semiconductors become insulators. Normally, the semiconductor material consists of at least two layers. Positive charge is located on one layer, and negative charge on the other layer. When the cell is exposed to light, the semiconductors atoms absorb some photons from the light and release electrons from the cell negative layer. The external circuit allows the flow of the released electrons back to the positive layer, which represent the electric current [2.2]. Figure 2.2 shows the electron-hole pair generation and minority carrier transport in a silicon solar cell, along with the external circuit.

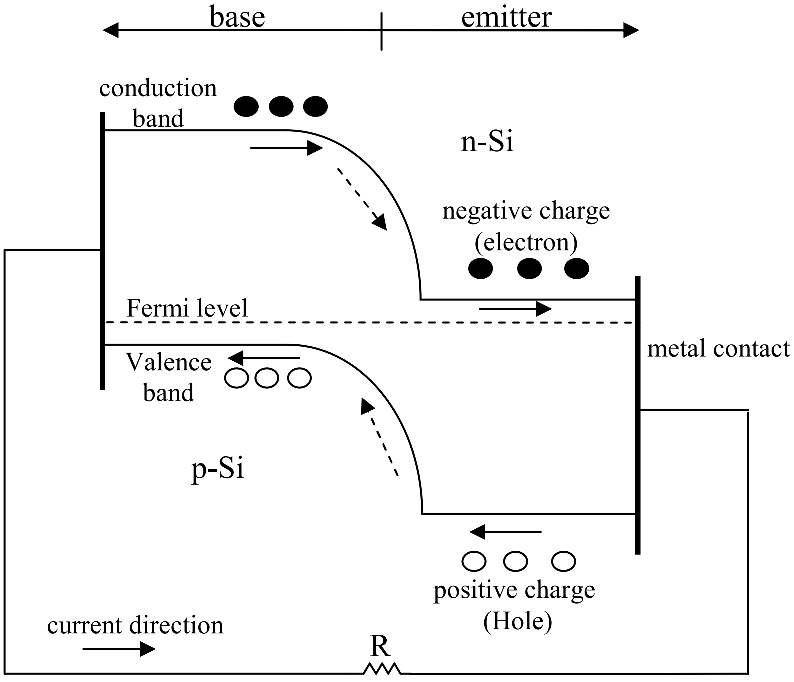

Figure 2.2. Solar cell band diagram for silicon solar cell.

Commonly, the semiconductor material used for the solar cell is silicon [2.3]. There are different types of solar cells. However the most commonly and commercially available types are monocrystalline, multicystalline, and amorphous [2.4]. The advantages and disadvantage vary from one type to another, depending on the targeted application [2.5]. Monocrystalline solar cells are manufactured from near pure silicon in which the entire solid is a continuous crystal lattice. This type of solar cell has an efficiency of approximately 25%. Alternatively, the multicystalline solar cell is the preferred type because it provides the best value in term of output power per unit cost. Unlike the monocrystalline solar cell, the multicystalline solar cell is constructed by slicing blocks of crystals into wafers to produce individual solar cells. Therefore, this type of solar cell is cheaper than the monocrystalline solar cell. Moreover, the efficiency of the multicystalline solar cell is approximately 20% which is slightly less than that of the monocrystalline solar cell. Amorphous solar cells are the least expensive type because they are manufactured by depositing a thin layer of silicon on a base material such as glass or metal. The efficiency of this type of solar cell is approximately 12.5%, which is considered to be low compared with the other types of solar cells. Amorphous solar cells are commonly used for low power applications such as calculators and garden lights. Recently, multi-junction or tandem cells have been developed. This type of solar cell contains several p-n junctions where each junction is tuned to a different wavelength of light. Therefore, the solar cell can absorb more energy from the light. The efficiency of this type of solar cells is approximately 43% which is relatively high compared to other solar cells types. Commercially, the use of this type of solar cells is limited to aerospace application due to the high cost [2.6].

The physical construction of a solar cell is shown in Figure 2.3. In general, a solar cell consists of top contacts, single or double layers of anti-reflective coating, an n-type emitter, a p-type base, and a back contact [2.7]. The purpose of the top contacts is to collect current from the emitter and to connect the solar cell to an external circuit. In Figure 2.3 only one bus bar and six fingers are shown as top contacts. However, the real solar cell consists of several bus bars and many fingers. To minimize light reflection from the solar cell, an anti-reflection coating is applied. The anti-reflection coating maximizes the light entering the cell, which increases the solar cell output power [2.8]. An n-type emitter and p-type base are the main components of the solar cell. The emitter layer, which contains the negative majority electrons, is made as thin as possible to attain reasonable sheet resistivity. Practically, the emitter layer thickness is approximately 2μm. On the other side, the base layer is thicker than the emitter layer, being almost the full thickness of the solar cell. Typically, the thickness of a silicon solar cell is about 200μm to 500μm. The rear contact is located at the bottom of the solar cell. It is mainly used to collect the charge carriers and to reflect the light back in to the optical path [2.9].

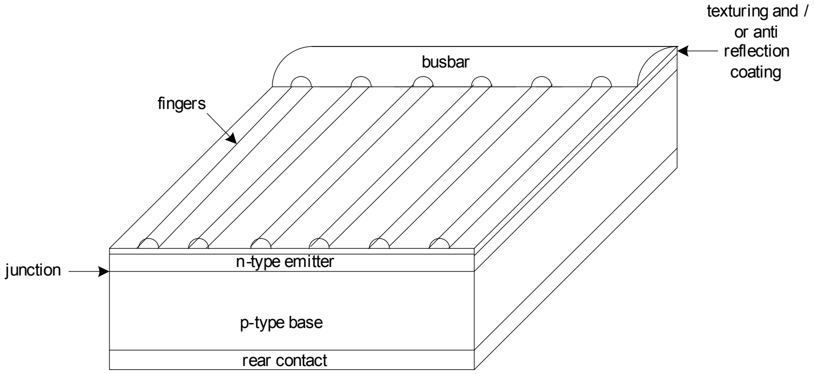

Figure 2.3. Schematic diagram of solar cell physical structure.

The equivalent circuit of the solar cell consists of a photocurrent source, a diode, a parallel resistor to model the leakage current, and a series resistor to describe the internal resistance. The equivalent circuit of a solar cell is shown in Figure 2.4. By using the equivalent circuit of the solar cell, the mathematical model of the generated current in a PV system is represented by [2.3]:

$$I_{pv} = I_{ph} - I_o \left[e^{\left(\frac{q\left(V_{pv} + R_s I_{pv}\right)}{AkT} \right)} - 1 \right] - \frac{(V_{pv} + R_s . I_{pv})}{R_{sh}} \tag{2.1}$$

where V_{pv} and I_{pv} represent the PV array output voltage and current, respectively. R_s and R_{sh} are the solar cell series and shunt resistances. q is the electron charge $1.6x10^{-19}C$; I_{ph} is the light generated current; I_o is the reverse saturation current; A is dimensionless junction material factor; k is Boltzmann constant ($1.38x10^{-23}J/K$); and T is the temperature (K).

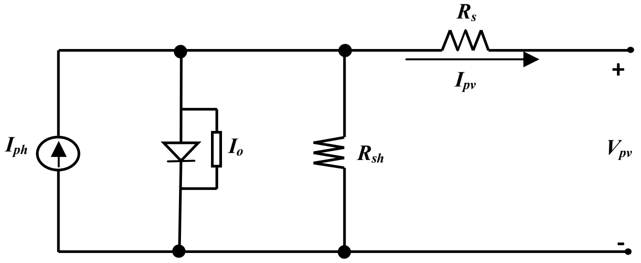

Figure 2.4. Equivalent circuit of a PV cell.

2.1.2 PV module

A PV module (PV panel) consists of a group of series connected solar cells to obtain sufficient working voltage [2.8]. Usually, the PV module is rated by its dc output power under standard test conditions (STC) and commercially STC is specified at an irradiance of $1000\ W/m^2$ with a spectral distribution of air mass (AM) 1.5 and a 25^oC PV cell temperature [2.10]. The PV module can be implemented from the mathematical model in eq. (2.1), which is derived from a cell's equivalent circuit where all cells are identical.

$$I_{pv} = I_{ph} - I_o \left[e^{\left(\frac{q\left(V_{pv}+R_s I_{pv}\right)}{AkTn_s} \right)} - 1 \right] - \frac{(V_{pv} + R_s.I_{pv})}{n_s.R_{sh}} \tag{2.2}$$

where V_{pv} and I_{pv} represent the PV array output voltage and current, respectively and n_p and n_s are the number of cells connected in parallel and series, respectively. For a given PV module, the Power-Voltage (P-V) characteristic and the Current-Voltage (I-V) characteristic under STC are shown in Figure 2.5.

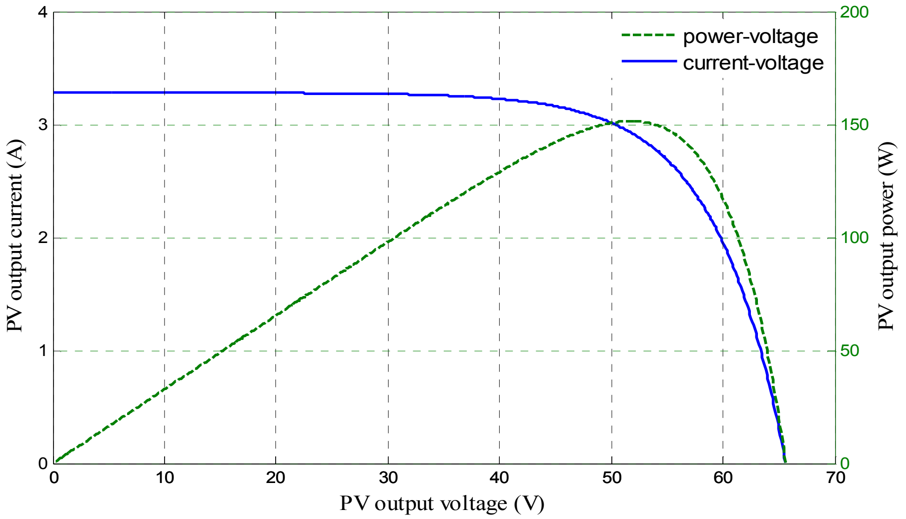

Figure 2.5. P-V and I-V characteristics of a given PV module under STC.

2.1.3 PV array

A PV array consists of a group of series-parallel connected PV modules to obtain the desired voltage and current. The size of the PV array varies from a single PV module to any number of modules. The PV array output voltage and current can be calculated from equations (2.3) and (2.4) respectively.

$$I_{PVt} = I_{PV} \times N_p \tag{2.3}$$

$$V_{PVt} = V_{PV} \times N_s \tag{2.4}$$

where I_{PVt} is the PV array output current, I_{PV} is the PV module output current, calculated using Eq. 2.1, V_{PVt} is the PV array output voltage, V_{PV} is the PV module output voltage, N_P is the number of the parallel strings in the PV array, and N_S is the number of series PV modules in one PV string. In the PV array, the number of PV modules in each string should be identical to get equal parallel voltages.

Generally, the electrical behaviour of the PV system is represented by the power versus voltage (or current, or duty cycle) and the current versus voltage characteristics. The characteristic curves of the solar cell are nonlinear because of operational physical phenomena [2.11]. The characteristic curves of the PV array system depend on the radiation and temperature of the PV system. For a given system, where the radiation λ is distributed across the PV modules, the power-voltage (*P-V*) characteristics under varying weather conditions are shown in Figure 2.6.

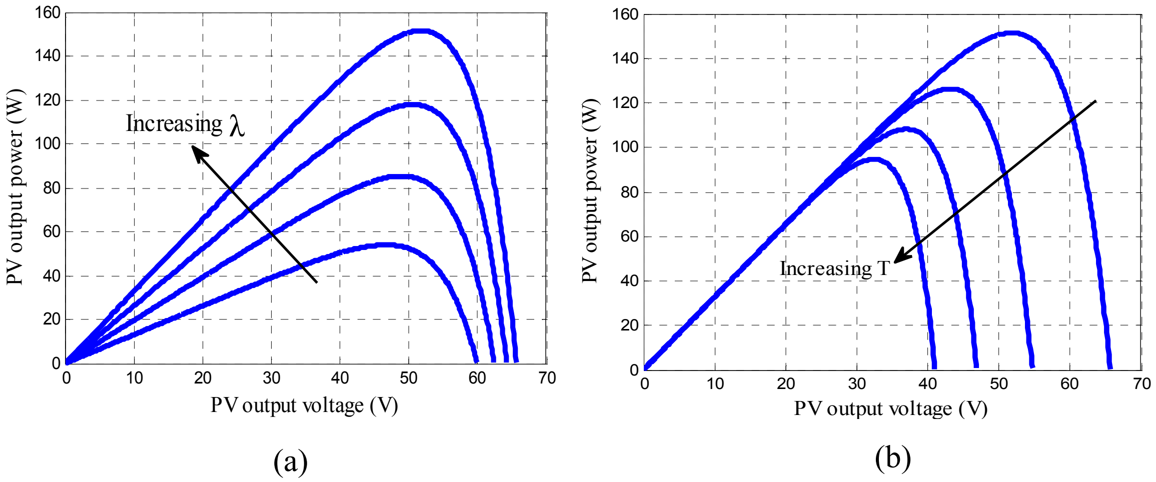

Figure 2.6. The influence on *P–V* characteristics of
(a) solar radiation *G* and (b) temperature *T*.

When the radiation is not equally distributed, local and global maxima are introduced into the characteristic curves [2.12]. In order to understand such phenomena, a PV array system with nine modules, connected 3×3 in series and parallel, is considered as shown in Figure 2.7a. There are different possibilities for the radiation distribution among the PV modules; five cases are randomly considered:

Case 1: One module in each column is completely shaded (viz. modules 1, 4 and 7).

Case 2: One module in each column is partially shaded with equal radiation levels (viz. modules 2, 5 and 8).

Case 3: One module of each column is partially shaded with unequal radiation levels (viz. modules 3, 6 and 9).

Case 4: Two modules of the first column and one module of each other column are partially shaded with equal radiation levels (viz. modules 1, 2, 4 and 7).

Case 5: All modules are partially shaded with different radiations levels.

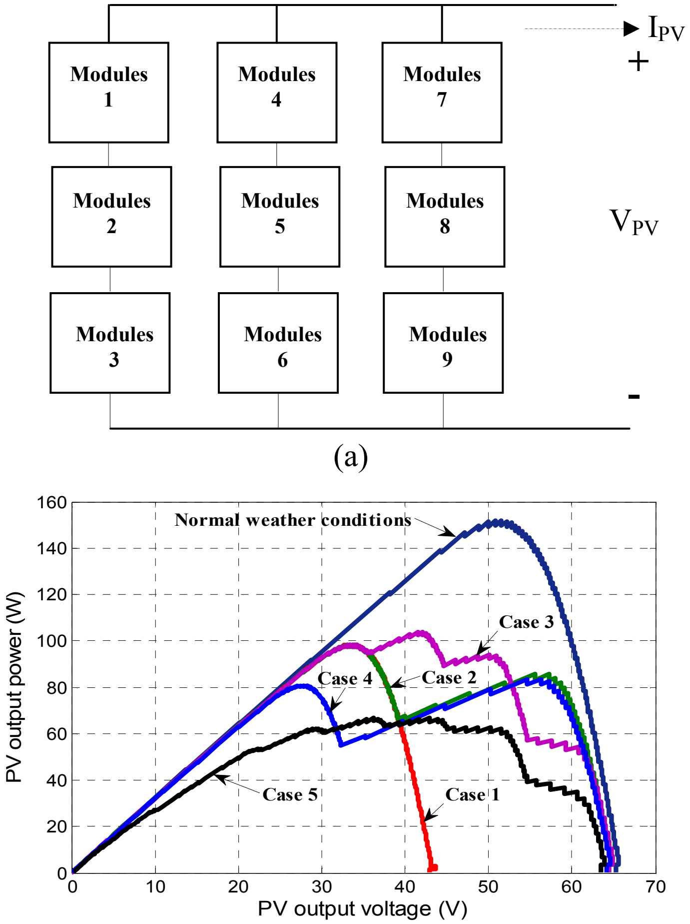

(a)

(b)

Figure 2.7. (a) PV array system with nine modules connected in series and parallel and (b) PV output power characteristics for the five cases.

Simulation results for the five cases, shown in figure 2.7b, indicate that a completely shaded module causes a reduction of the PV output power without creating local maxima. However, partially shaded modules result in reduced PV output power and the creation of local maxima, where the number of local maxima increases as the radiation variation of each module increases.

2.2 Photovoltaic system

In distributed generation applications, the PV system is divided into two modes; standalone and grid-connected. In both modes, MPPT is required to ensure that the PV system operates at the maximum power point for different weather conditions.

2.2.1 Maximum power point tracker (MPPT)

As shown in section 2.1, the efficiency of the solar cell is relatively low, and the characteristics curves of the PV array power and current are highly nonlinear and are affected by irradiance and temperature variations. Therefore, a maximum power-point tracker (MPPT) is required to cater for these issues and ensure that the PV system operates at the maximum power point (MPP) [2.13]. Many MPPT techniques have been proposed in the literature, such as perturbation and observation, incremental conductance, parasitic capacitance, constant voltage, ripple correlation control, constant current, fuzzy logic controller, and artificial intelligence techniques [2.14, 15]. These techniques vary in simplicity, accuracy, time response, popularity, cost, and other technical aspects. Another important aspect is the existence of local maxima in the PV characteristic curve during random distribution of the sun's radiation on the PV array. Therefore, different methods have been proposed to cater for the partial shading effect by either improving the existing MPPT techniques or applying advanced optimization techniques.

2.2.2 Standalone PV systems

A standalone PV system is operated independently of the utility grid. It can be designed to supply either ac or dc electric loads [2.16]. For dc load application, PV systems utilize single-stage dc/dc power converters such as the boost, buck or buck-boost converters. The dc/dc power converter plays a major role in changing the voltage level to track the MPP. Alternatively, for ac load application, a two-stage topology along with battery banks connected between the two stages is used. In the first stage, the boost converter is utilized to boost the PV voltage and track the MPP. In the second stage, the dc/ac inverter is use to convert the dc power to ac power and improve the ac power quality. In some PV application with a critical load, battery banks are used to fix the inverter dc voltage and enhance or supply the required load power. Figure 2.8 shows the block diagram of the standalone PV system for dc and ac load.

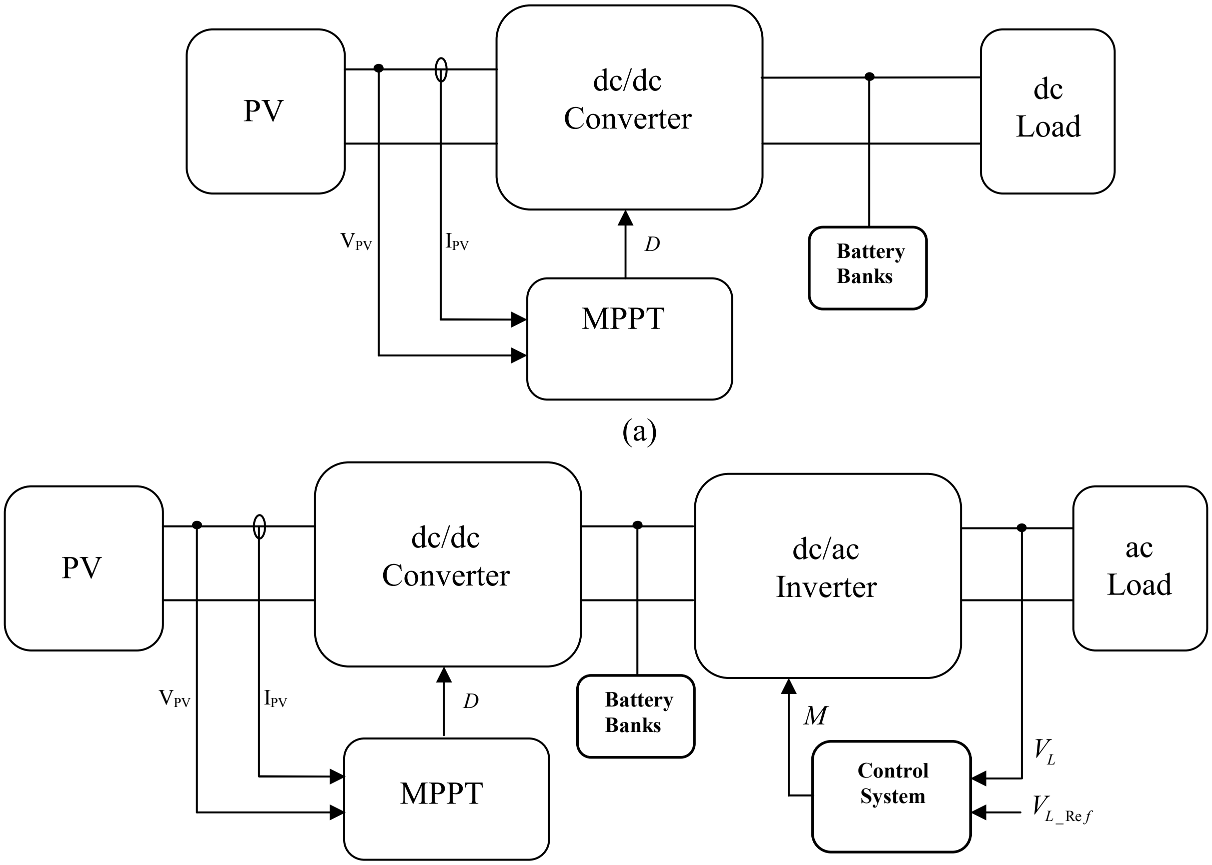

(a)

(b)

Figure 2.8. (a) Block diagram of a standalone PV system supplying a dc load, and (b) block diagram of a standalone PV system supplying an ac load.

2.2.3 Grid-connected PV systems

PV modules generate dc power. Therefore, to inject the PV power into the grid, the PV dc power must be converted to ac power. In order to convert the dc to ac, a power electronics inverter is employed. In addition to the converting capability, the inverter is used for the MPPT. Another power electronics device, a dc-dc converter, could be used to boost the PV output voltage and track the MPP. In the PV market, there are different inverter configurations:

- centralized technology
- string technology
- multi-string technology
- ac-module technology

Centralized inverter technology is considered to be the first PV grid-connected configuration [2.17]. To obtain a PV array with the desired output power and dc voltage level, PV strings (a number of PV modules connected in series), are connected in parallel. The PV array output is connected to a single dc to ac inverter. In such a configuration, PV maximum power is delivered into the grid with high efficiency, small size, and low cost. However, to fulfil grid requirements, such a topology requires either a step-up transformer, which reduces the system efficiency and increases cost, or a PV array with a high dc voltage. A high voltage PV system suffers from hotspots (where a PV module with lower radiation behaves as a load) during partial shading and increased leakage current between the PV panel and the system ground though parasitic capacitances. Moreover, the parallel connected PV strings could have different optimum voltages, resulting in multiple peaks on the PV array characteristic curve. In order to improve MPPT during partial shading or string optimum voltage mismatch, string technology is used, where each PV string is connected to an inverter with its own MPPT. Disadvantages of this configuration are that it requires a large number of components and has high installation costs. Multi-string technology is similar to string technology. The difference is that a dc-dc converter is installed on each PV string where the outputs of each dc-dc converter are connected to a single dc-ac inverter. The added dc-dc converter on each string is employed to track the MPP and avoids having a large dc voltage PV module. This technology is expensive because each string has its own converter. The last configuration is ac module technology, in which each PV module is connected to a different inverter, where the MPP from each module is extracted separately. This technology is recommended when PV modules with different power rating are used. When compared with other approaches, ac-module technology is considered to be the most expensive. Figure 2.9 illustrates the PV system technologies.

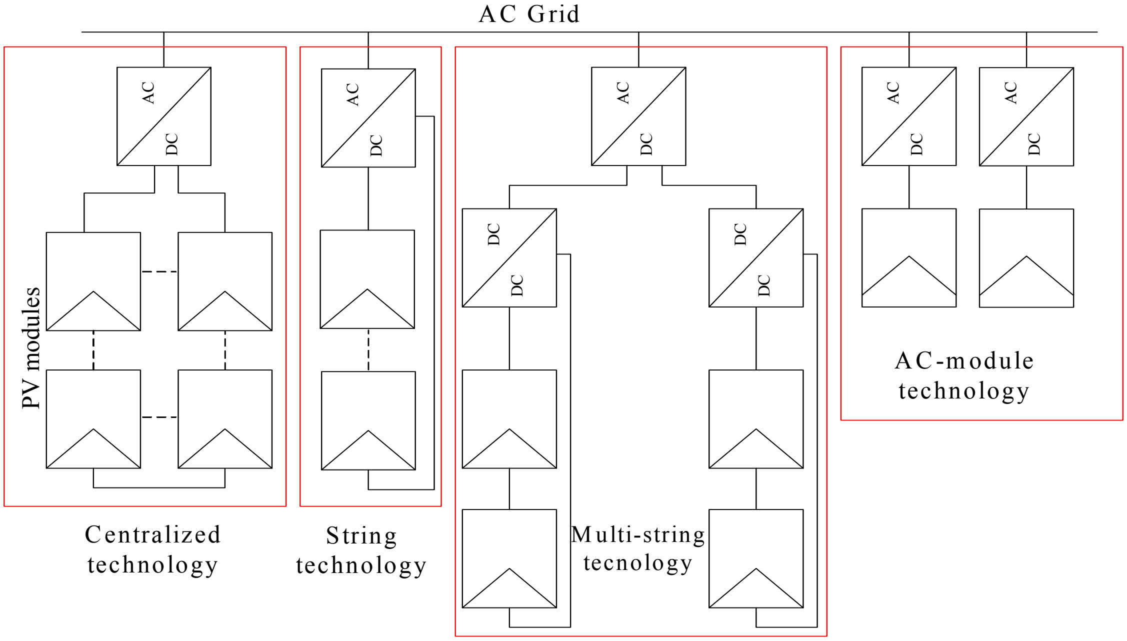

Figure 2.9. Photovoltaic grid interfacing system technologies.

2.3 Power electronics interfacing topologies for PV systems

In a grid-connected mode, the maximum power is extracted from the PV system to inject the maximum available power into the grid. Single and two stages grid-connected topologies are commonly used topologies in single and three-phase PV systems [2.18, 19].

2.3.1 Single-stage grid-connected

In a single-stage grid-connected system, the PV system utilizes a single conversion unit (dc-ac power inverter) to track the maximum power point (MPP) and interface the PV system to the grid. In such a topology, PV maximum power is delivered into the grid with high efficiency, small size, and low cost [2.20]. However, to fulfil grid requirements, such a topology requires either a step-up transformer, which reduces the system efficiency and increases cost, or a PV array with a high dc voltage. High voltage systems suffer from hotspots during partial shading and increased leakage current between the panel and the system ground though parasitic capacitances, as described in section 2.2.3. Moreover, inverter control is complicated because the control objectives, such as maximum power point tracking (MPPT), power factor correction, and harmonic reduction, are simultaneously considered. Different types of dc-ac inverters have been applied to enhance and regulate the performance, such as two-level and multilevel voltage source inverters and current source inverters. A block diagram of a single-stage grid-connected PV system is illustrated in Figure 2.10.

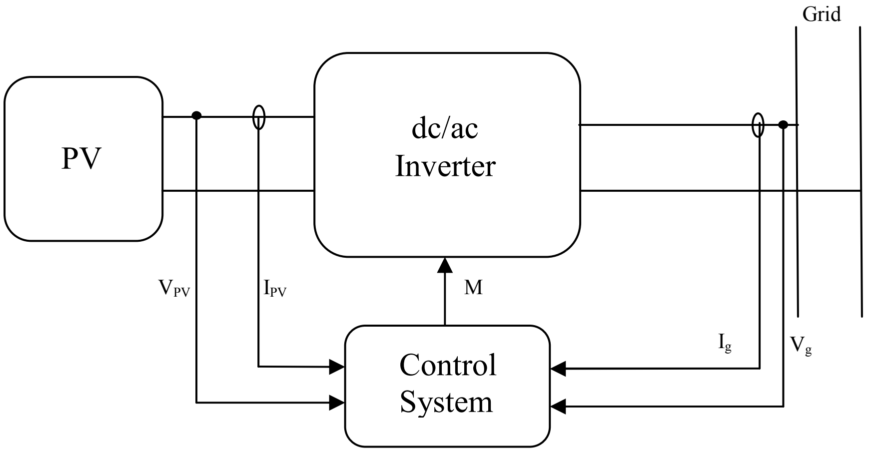

Figure 2.10. Block diagram of a single-stage grid-connected PV system.

2.3.2 Two-stage grid-connected

In this topology the PV system utilizes two conversion stages. The first stage uses dc/dc converter (boost, buck, or buck-boost) for changing the PV output voltage level and tracking the maximum power point. A dc/ac inverter is utilized in the second stage to regulate the dc link voltage and to synchronize the PV system output to the grid voltage and current in order to achieve the desired power factor. The advantages of the two-stage topology lies in the simplicity of designing the control scheme, since the control requirements are distributed between the two stages. Moreover, a PV array with a high voltage output is not required because of the first amplification stage. In single-phase applications, the dc/dc converter stage handles the power fluctuation that causes voltage ripple on the PV side at double (and multiples of) the line frequency [2.17]. However, such a topology suffers from higher power losses, larger footprint and higher cost than single-stage systems [2.21]. A block diagram of a two-stage grid-connected PV system is illustrated in Figure 2.11.

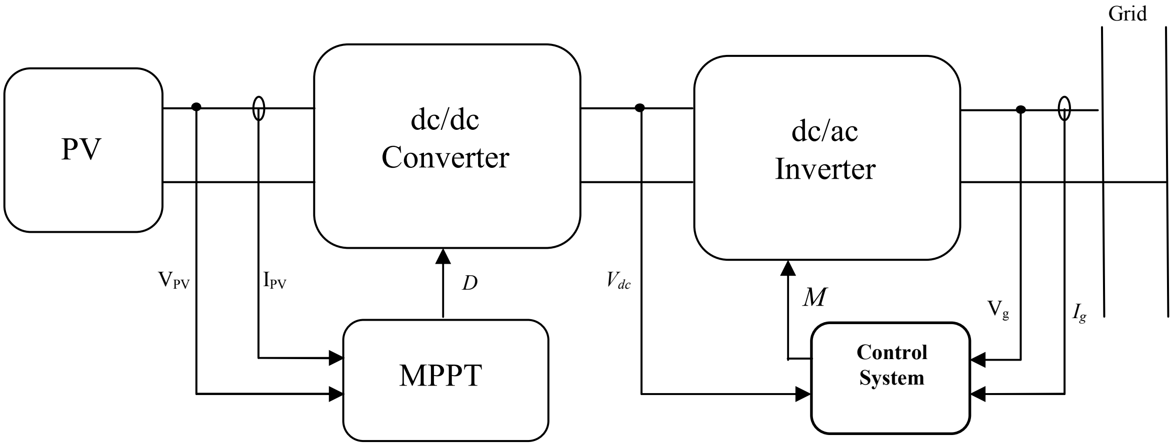

Figure 2.11. Block diagram of a two-stage grid-connected PV system.

2.3.3 DC-AC inverter

In a grid-connected system, the boost dc/dc converter is commonly used in the two-stage topology, where many types of dc/ac inverters can be used on either single-stage or two-stage topologies. Therefore, this section presents the common dc/ac inverters used in PV applications.

a. Two- level voltage source inverter

The conventional dc/ac inverter is widely used in the single-stage grid-connected applications because of its simplicity and availability [2.22]. However, to fulfil grid requirements, such a topology requires either a step-up transformer, or a PV array with a high dc voltage output. An electrolytic capacitor, which presents a critical point of failure, is required in this topology to store energy in the dc bus. Moreover, inverter control is complicated because the control objectives, such as MPPT, power factor correction, and harmonic reduction, are simultaneously considered.

b. Multilevel inverter

Recently, multilevel inverters have attracted attention because of their ability to overcome two-level dc-ac inverter limitations such as high harmonic distortion, high voltage stress on power switches, and high power losses due to a high switching frequency [2.23-25]. They offer lower THD (total harmonic distortion), switching frequency, *dv/dt* and device voltage stress. A five-level pulse-width modulation (PWM) inverter for a grid-connected PV system is proposed in [2.24], and the multilevel inverter operates by adopting a full bridge inverter with an auxiliary circuit to generate five voltage levels at the output. The current injected into the grid is improved by a smaller filter size and lower harmonic distortion, however, the inverter switching frequency is high, 20 kHz. Additionally, the problem of high voltage stress on power switches is not resolved and this may result in reduced switch lifetime. A diode clamped multilevel inverter with more than three voltage levels for grid integration of PV using a single-stage is proposed in [2.23]. However, the principle of minimum switching losses is violated by allowing switching of more than one voltage level at the same instant. This results in increased switching losses, harmonic distortion and device voltage stress, and high *dv/dt*. Therefore, this topology is not suitable for medium voltage applications, or even low-voltage applications. It requires a relatively large ac filter to meet harmonic requirements at the point of common coupling (PCC). Cascaded multilevel inverters are used in PV system applications since separate dc voltage sources are available [2.25]. In a PV system, the inverter input voltage changes over a wide range depending on the weather conditions, therefore, it cannot be guaranteed that the voltage is always maintained at the designed voltage level. Moreover in two-stage grid-connected PV systems, the boost converter must be installed on each unit to ensure separation of the dc inputs and this leads to increased system size and cost. In a two-stage grid-connected PV system, a modular multilevel inverter (M2I) regulates the boost converter output voltage to be fixed and the injected current into the grid to achieve unity power factor operation [2.26].

The M2I has been designed to alleviate the drawbacks of conventional multilevel inverters such as the difficulty of capacitor voltage balancing on higher order levels, the need for an output filter and an interfacing transformer. Also conventional multilevel inverters are not capable of fault management and fault ride-through [2.27].

c. Current source inverter

The current source inverter (CSI) has not been extensively investigated for grid-connected renewable energy systems [2.28]. However, it is a viable alternative technology for PV distributed generation, grid connection for the following reasons:

- The dc input current is continuous which is important for PV application.
- System reliability is increased by replacing the shunt input electrolytic capacitor with a series input inductor.
- The inherently CSI voltage boosting capability allows a low-voltage PV array to be grid interfaced without the need of a transformer or an additional boost stage.

For single-phase single-stage application, the power fluctuation causes even harmonics on the dc side, which affect MPPT, reduce PV lifetime, and are associated with odd order harmonics on the grid side [2.29-32]. Therefore, eliminating the even harmonics on the dc side is essential in PV applications. Various techniques have been proposed to reduce the even harmonic effects in CSI PV applications [2.30].

2.4 Summary

In this chapter, the photovoltaic cell, module, and array, and their characteristic curves have been described in detail to realize their physical components. Standalone and grid-connected PV applications were presented to illustrate their power circuit and control systems. The integration options for a grid-connected photovoltaic system were discussed to clarify their power electronics topology requirements. The types of the dc-ac inverters which are used on either single or two stage topologies were presented.

References

[2.1] D. M. Tagare, Electricity Power Generation: The Changing Dimensions: Wiley, 2011.

[2.2] Introduction to Photovoltaic Systems- the infinitepower of Texas. Available:http://www.infinitepower.org/pdf/FactSheet-11.pdf.

[2.3] F. A. Farret and G. Simões, Integration of Alternative Sources of Energy: John Wiley & Sons, 2006.

[2.4] Solar Photovoltaics for Development Applications: Sandia National Laboratories, SAND93-1642, August 1993.

[2.5] Solar power industries. Available: http://www.solarpowerindustries.com/solarcelltypes.cfm.

[2.6] K. H. Lee, K. W. J. Barnham, J. P. Connolly, B. C. Browne, R. J. Airey, J. S. Roberts, M. Fuhrer, T. N. D. Tibbits, and N. J. Ekins-Daukes, "Demonstration of Photon Coupling in Dual Multiple-Quantum-Well Solar Cells," Photovoltaics, IEEE Journal of, vol. 2, pp. 68-74, 2012.

[2.7] K. K. Ng, Complete Guide to Semiconductor Devices: Wiley, 2002.

[2.8] R. A. A. MESSENGER and J. A. VENTRE, Photovoltaic Systems Engineering, Second Edition: Taylor & Francis Group, 2004.

[2.9] P. Würfel, Physics of Solar Cells: From Basic Principles to Advanced Concepts: Wiley, 2009.

[2.10] "IEEE Recommended Practice for Testing the Performance of Stand-Alone Photovoltaic Systems," IEEE Std 1526-2003, pp. 0_1-18, 2004.

[2.11] M. Kolhe, J. C. Joshi, and D. P. Kothari, "Performance analysis of a directly coupled photovoltaic water-pumping system," Energy Conversion, IEEE Transactions on, vol. 19, pp. 613-618, 2004.

[2.12] A. Bidram, A. Davoudi, and R. S. Balog, "Control and Circuit Techniques to Mitigate Partial Shading Effects in Photovoltaic Arrays," Photovoltaics, IEEE Journal of, vol. 2, pp. 532-546, 2012.

[2.13] D. Tagare, Electricity Power Generation:The Changing Dimensions Wiley-IEEE Press 2011.

[2.14] B. Subudhi and R. Pradhan, "A Comparative Study on Maximum Power Point Tracking Techniques for Photovoltaic Power Systems," Sustainable Energy, IEEE Transactions on, vol. 4, pp. 89-98, 2013.

[2.15] M. A. G. de Brito, L. Galotto, L. P. Sampaio, G. de Azevedo e Melo, and C. A. Canesin, "Evaluation of the Main MPPT Techniques for Photovoltaic Applications," Industrial Electronics, IEEE Transactions on, vol. 60, pp. 1156-1167, 2013.

[2.16] G. M. Masters, Renewable and Efficient Electric Power Systems: John Wiley & Sons, 2004.

[2.17] S. B. Kjaer, J. K. Pedersen, and F. Blaabjerg, "A review of single-phase grid-connected inverters for photovoltaic modules," Industry Applications, IEEE Transactions on, vol. 41, pp. 1292-1306, 2005.

[2.18] Y. Bo, L. Wuhua, Z. Yi, and H. Xiangning, "Design and Analysis of a Grid-Connected Photovoltaic Power System," Power Electronics, IEEE Transactions on, vol. 25, pp. 992-1000, 2010.

[2.19] W. Tsai-Fu, C. Chih-Hao, L. Li-Chiun, and K. Chia-Ling, "Power Loss Comparison of Single- and Two-Stage Grid-Connected Photovoltaic Systems," Energy Conversion, IEEE Transactions on, vol. 26, pp. 707-715, 2011.

[2.20] T. J. Liang, Y. C. Kuo, and J. F. Chen, "Single-stage photovoltaic energy conversion system," Electric Power Applications, IEE Proceedings -, vol. 148, pp. 339-344, 2001.

[2.21] S. Jain and V. Agarwal, "A Single-Stage Grid Connected Inverter Topology for Solar PV Systems With Maximum Power Point Tracking," Power Electronics, IEEE Transactions on, vol. 22, pp. 1928-1940, 2007.

[2.22] R. Gonzalez, J. Lopez, P. Sanchis, and L. Marroyo, "Transformerless Inverter for Single-Phase Photovoltaic Systems," Power Electronics, IEEE Transactions on, vol. 22, pp. 693-697, 2007.

[2.23] S. Busquets-Monge, J. Rocabert, P. Rodriguez, S. Alepuz, and J. Bordonau, "Multilevel Diode-Clamped Converter for Photovoltaic Generators With

Independent Voltage Control of Each Solar Array," Industrial Electronics, IEEE Transactions on, vol. 55, pp. 2713-2723, 2008.

[2.24] J. Selvaraj and N. A. Rahim, "Multilevel Inverter For Grid-Connected PV System Employing Digital PI Controller," Industrial Electronics, IEEE Transactions on, vol. 56, pp. 149-158, 2009.

[2.25] E. Villanueva, P. Correa, J. Rodriguez, and M. Pacas, "Control of a Single-Phase Cascaded H-Bridge Multilevel Inverter for Grid-Connected Photovoltaic Systems," Industrial Electronics, IEEE Transactions on, vol. 56, pp. 4399-4406, 2009.

[2.26] B. N. Alajmi, K. H. Ahmed, G. P. Adam, S. J. Finney, and B. W. Williams, "Modular multilevel inverter with maximum power point tracking for grid connected photovoltaic application," in Industrial Electronics (ISIE), 2011 IEEE International Symposium on, 2011, pp. 2057-2062.

[2.27] G. P. Adam, O. A. Lara, G. Burt, S. J. Finney, and B. W. Williams, "Comparison between Two VSC-HVDC Transmission Systems Technologies: Modular and Neutral Point Clamped Multilevel Converter," presented at the 13 th Annual conference of the Industrial Electronic Society IECON2009, Porto-Portugal, November 2009.

[2.28] B. Sahan, Arau, x, S. V. jo, No, C. ding, and P. Zacharias, "Comparative Evaluation of Three-Phase Current Source Inverters for Grid Interfacing of Distributed and Renewable Energy Systems," Power Electronics, IEEE Transactions on, vol. 26, pp. 2304-2318, 2011.

[2.29] S. Nonaka, "A suitable single-phase PWM current source inverter for utility connected residential PV system," Solar Energy Materials and Solar Cells, vol. 35, pp. 437-444, 1994.

[2.30] A. Darwish, A. K. Abdelsalam, A. M. Massoud, and S. Ahmed, "Single phase grid connected curent source inverter: Mitigation of oscillating power effect on the grid current," in Renewable Power Generation (RPG 2011), IET Conference on, 2011, pp. 1-7.

[2.31] R. T. H. Li, C. Henry Shu-hung, and T. K. M. Chan, "An Active Modulation Technique for Single-Phase Grid-Connected CSI," Power Electronics, IEEE Transactions on, vol. 22, pp. 1373-1382, 2007.

[2.32] K. Hirachi and Y. Tomokuni, "A novel control strategy on single-phase PWM current source inverter incorporating pulse area modulation," in Power Conversion Conference - Nagaoka 1997., Proceedings of the, 1997, pp. 289-294 vol.1.

Chapter 3

A Modified Hill-Climbing Method for Maximum Power Point Tracking in Standalone Photovoltaic Systems

In this chapter, a new fuzzy logic controller for maximum power point tracking of a photovoltaic system is proposed. Conventional hill climbing maximum power point tracking (MPPT) structures and features are investigated. The new controller improves the hill climbing search method by fuzzifying the rules of such techniques and reduces their disadvantages. Simulation and experimental results are provided in this chapter to validate the proposed fuzzy logic based controller.

3.1 Background

The PV array power and current characteristics are highly nonlinear and are affected by irradiance and temperature variation. Therefore, MPPT is required to handle such problems [3.1]. Many different MPPT techniques have been proposed [3.2]. The existing techniques vary in simplicity, accuracy, time response, popularity, cost, and other technical aspects.

The voltage based maximum power point tracking method exploits the fact that the ratio of the maximum power voltage to the open circuit voltage under different weather conditions, is linearly proportional [3.3] (and varies much less than the corresponding current). Since this method is based on an approximation of a constant ratio, the extracted power is most likely to be less than the actual MPP, which results in significant loss of the available power. Moreover, this method fails to track the MPP if some of the PV array cells are partially shaded or damaged. A similar MPPT method, called current based MPPT, has been proposed. This method approximates the ratio of the maximum power current to the short circuit current under different weather conditions [3.4]. The same limitations as voltage based MPPT exist with this method.

The incremental conductive method is widely used because of implementation simplicity and high tracking efficiency. The method is based on the derivative of power with respect to voltage (dP/dV) being zero at the MPP, positive on the left of the MPP, and negative on the right. Complex computation is required to give good performance under rapidly varying weather conditions. Moreover, the tracking time is relatively long since the step size is tuned to be small enough to reach the desired MPP [3.5].

Ripple correlation control (RCC) is an optimization technique that takes advantage of the converter signal ripple to track the MPP [3.6]. The optimal point is approached by changing the operating current according to its location. The tracking speed is comparatively fast in this method. However, since the differentiators are sensitive to noise and disturbance, the MPP accuracy is poorer than other MPPT methods.

Among the MPPT methods, hill climbing/perturbation and observation (P&O) are the most commonly used algorithms because of simplicity, ease of implementation, and low cost [3.7]. Hill climbing works by perturbing the PV array system by changing the power converter duty cycle and observing its impact on the PV array output power, and then deciding the new direction of the duty cycle to extract maximum power. Similarly, P&O functions by perturbing the PV array output current and observing its impact on output power. It is frequently assumed that both techniques are the same. The authors in [3.7-9] use duty cycle perturbation but term it P&O. On the other hand, in [3.10] a comparison between hill climbing and P&O proves that P&O is more efficient, especially under varying weather conditions. In general both techniques use the same concept to search for the optimum operating point searching, but with different control structures.

The fuzzy logic controller (FLC) has been introduced to alleviate the disadvantage of the P&O and hill climbing algorithms. In most fuzzy-based MPPT algorithms [3.11-15], the optimum point is tracked after computing the slope of the power-current characteristic and the slope change. The drawback of this fuzzy controller, as shown in [3.11], is that the operating point moves away from the maximum point when the irradiance changes, since duty cycle variation is neglected. Therefore, the authors in [3.12] introduced a fuzzy controller with array power variation and duty cycle as inputs. This technique improves the dynamic characteristics in variable weather conditions; however steady-state error occurs in the PV output power. To improve the dynamic characteristics and power level accuracy, both techniques have been combined [3.13]. Three inputs are used for the fuzzy controller: the array derivative *dP/dI*, the change of this derivative, and duty cycle variation. However, practically computing the slope is challenging, especially in a noisy environment. The author in [3.14] improved the fuzzy based MPPT method in [3.11] by adding fuzzy cognitive networks. The tracking speed is significantly improved, however it requires an additional switch in parallel with the PV system and an additional current sensor to compute the short circuit current. Self-tuning fuzzy control for a photovoltaic inverter system is proposed in [3.16]. The scaling factor of both inputs and the output are automatically tuned to improve system performance.

In this thesis, a fuzzy logic based hill climbing technique is proposed for MPPT in a microgrid stand-alone PV system. The disadvantages of conventional hill climbing are investigated. The proposed FLC is capable of exploiting the advantages of the hill climbing searching method whilst reducing its disadvantages. The FLC is designed by translating the conventional hill climbing algorithm into 16 fuzzy rules, after the controller inputs and output have been divided in to four fuzzy subsets. Simulation and experimental results allow evaluation of the effectiveness and robustness of the proposed control technique.

3.2 Conventional hill climbing technique

Hill climbing operates by perturbing the system by changing the power converter duty cycle and observing its impact on the array output power. This MPPT method is the most commonly used algorithm in practice because of simplicity, easy implementation, and low-cost. However, it has three major disadvantages:

1- Slow convergence to the optimum operating point.
2- At steady state, the amplitude of the PV power oscillates around the maximum point which causes system power losses.
3- During cloudy days when the irradiance varies quickly, the maximum optimum point moves away from the operating point.

Figure 3.1 is introduced to illustrate the behaviour of a PV system controlled by conventional hill climbing MPPT. In figure 3.1a, the PV output power is forced to move toward the optimum point by a hill climbing algorithm. After reaching the optimum point, the PV output power oscillates around the MPP. At 0.5 second the solar radiation is increased from 0.5 *KW/m*^{2} to 1 *KW/m*^{2}, therefore the power moves to the new optimum point. The controller output in Figure 3.1b is used to verify the aforementioned disadvantages of the hill climbing algorithm. Ellipse 1 shows the required time for the controller to compute the optimum duty cycle of the boost converter, ellipse 2 shows the duty cycle oscillation around the optimum value, and ellipse 3 shows the duty cycle divergence from the optimum value.

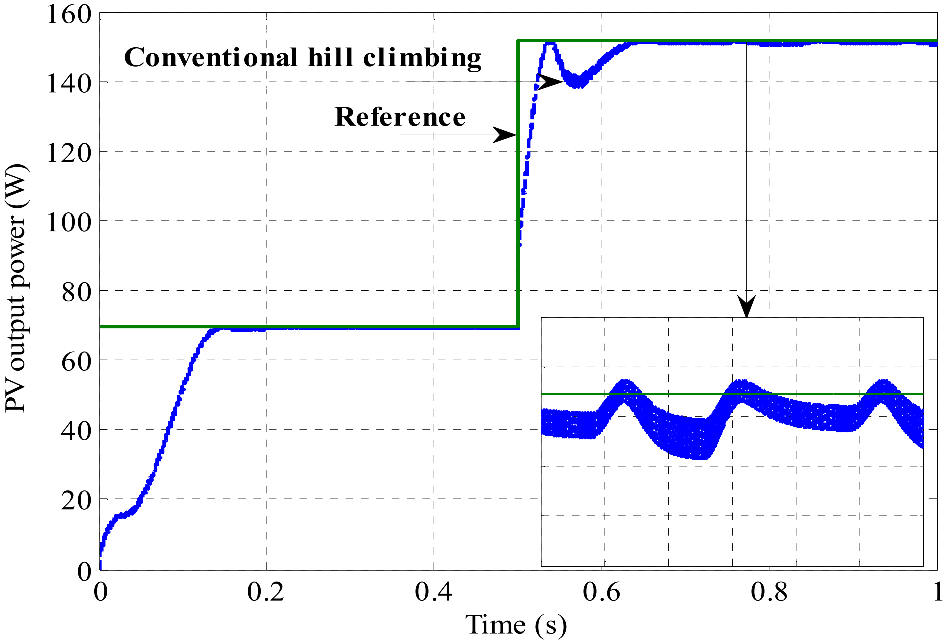

(a)

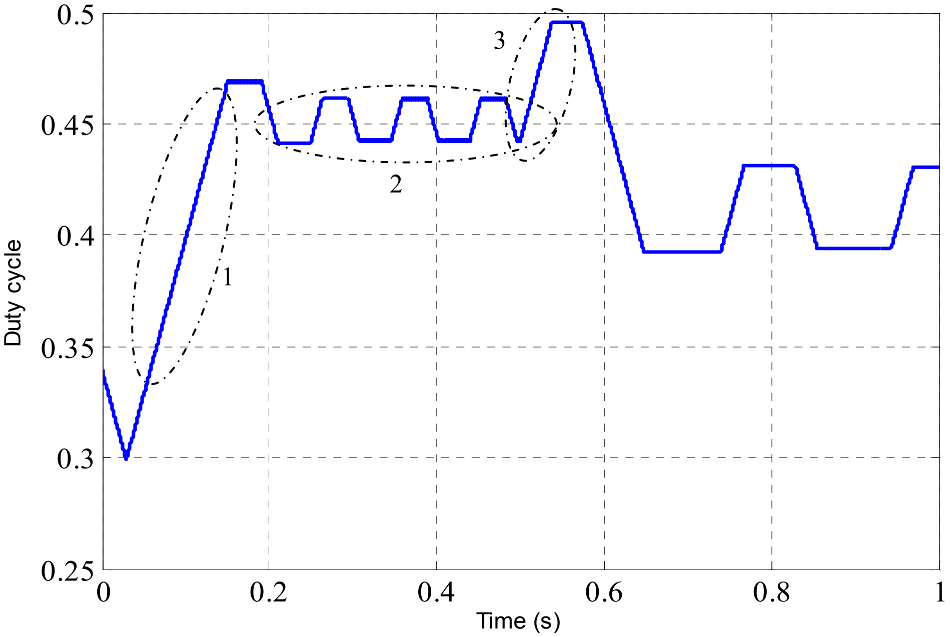

(b)

Figure 3.1. Disadvantages of the hill climbing method:
(a) PV output power and (b) duty cycle.

Several techniques in the literature have addressed improving hill climbing. In [3.17], a technique has been developed to overcome oscillation around the MPP by optimizing the sampling time rate according to the converter's dynamics. A similar technique was implemented in [3.7] by customizing the duty-cycle perturbation magnitudes to the dynamic behaviour of a specific dc-dc converter to realize the adaptive algorithm. The second disadvantage with the hill climbing algorithm is greatly reduced in [3.7, 17], however the first and the third drawbacks remain in both proposals. Moreover, to improve hill climbing performance, the author in [3.18] proposed an adaptive based controller to enhance steady-state and converging speed performance. At steady state, the incremental step is small and during a transient stage the incremental step size is large. The following equation is used to tune the incremental step:

$$\Delta D(k) = \alpha \frac{|\Delta P|}{\Delta D(k-1)} \tag{3.1}$$

The disadvantage of equation 3.1 is that the constant factor (α) requires manual tuning for different radiation levels and PV systems, which makes it commercially impractical. In [3.19], the authors enhanced the variable step size techniques by designing a feedback compensator to minimize the oscillation problem. A new MPPT technique, called the β method, is proposed in [3.20]. This method uses conventional hill climbing and the approximated β MPP method simultaneously to extract the exact MPP. According to [3.21] the β method offers faster convergence to the MPP than the conventional hill climbing method. However, such a method depends on PV array configuration parameters which make it impractical. Adaptive hill climbing has been proposed in [3.22] where a power window is added to the hill climbing method. The operating point is kept within the window, just below the maximum power point. Once each iteration loop, the window size is adjusted until the optimum power is reached. In the conventional method, two points (the recent power and the previous power) are compared to choose the direction of the next incremental step. However, in [3.23] the authors proposed a three-point comparison method: point A is the current condition, point B is perturbed from point A, and point C is doubly perturbed in the opposite direction from point B. This method successfully eliminates the oscillation problem, however slow convergence and divergence problems still exist. An improved perturbation and observation method is proposed in [3.24]. It is based on an adaptive algorithm which automatically adjusts the reference step size and hysteresis bandwidth for power comparison. The algorithm shows better steady-state performance and total PV output power increases 0.5% over the classic case, under varying weather conditions.

3.3 Modified Hill Climbing Fuzzy Based Technique

A modification of the hill climbing searching method uses a FLC based algorithm. The proposed controller is designed to take advantage of hill climbing simplicity and eliminates the aforementioned disadvantages. The PV system block diagram, including the proposed controller, is shown in Figure 3.2.

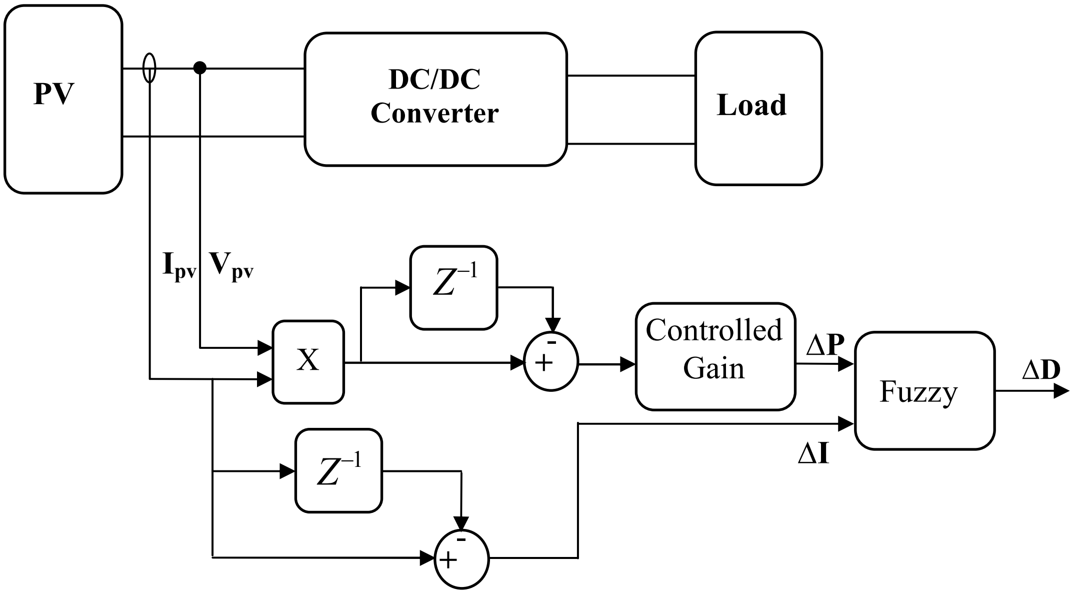

Figure 3.2. Block diagram of the PV array system along with the proposed MPPT controller.

The inputs of the FLC are:

$$\Delta P = P(k) - P(k-1) \tag{3.2}$$

$$\Delta I = I(k) - I(k-1) \tag{3.3}$$

and the output equation is:

$$\Delta D = D(k) - D(k-1) \tag{3.4}$$

where ΔP is the PV array output power change, ΔI is the array output current change, and ΔD is the boost converter duty cycle change. To ensure that the PV output power does not diverge from the optimum point during varying weather conditions, ΔP passes through a gain controller to reverse its direction as described in section 3.4. The variable inputs and output are divided into four fuzzy subsets: PB (Positive Big), PS (Positive Small), NB (Negative Big), and NS (Negative Small). Therefore, the fuzzy rules algorithm requires 16 fuzzy control rules. These rules are based on regulation of the hill climbing algorithm. To operate the fuzzy combination, Mamdani's method with Max-Min is used [3.25]. The fuzzifications of the hill climbing rules are shown in Figure 3.3.

```
If ΔP > 0
If ΔI > 0
D(t)= D(t-1) + ΔD
Else
D(t)=D(t-1)-ΔD
End
```

If ΔP is PB and ΔI is PB then ΔD is PB
If ΔP is PB and ΔI is PS then ΔD is PB
If ΔP is PB and ΔI is NB then ΔD is NB
If ΔP is PB and ΔI is NS then ΔD is NB
If ΔP is PS and ΔI is PB then ΔD is PS
If ΔP is PS and ΔI is PS then ΔD is PS
If ΔP is PS and ΔI is NB then ΔD is NS
If ΔP is PS and ΔI is NS then ΔD is NS

```
elseIf ΔP < 0
If ΔI > 0
D(t) = D(t-1) - ΔD
Else
D(t)=D(t-1)+ ΔD
End
End
```

If ΔP is NB and ΔI is PB then ΔD is NB
If ΔP is NB and ΔI is PS then ΔD is NB
If ΔP is NB and ΔI is NB then ΔD is PB
If ΔP is NB and ΔI is NS then ΔD is PB
If ΔP is NS and ΔI is PB then ΔD is NS
If ΔP is NS and ΔI is PS then ΔD is NS
If ΔP is NS and ΔI is NB then ΔD is PS
If ΔP is NS and ΔI is NS then ΔD is PS

Figure 3.3. Fuzzification of the modified hill climbing rules.

After simulating the PV system and studying the behaviour of the controller inputs and output, the shapes and fuzzy subset partitions of the membership function in both of inputs and output are shown in Figure 3.4.

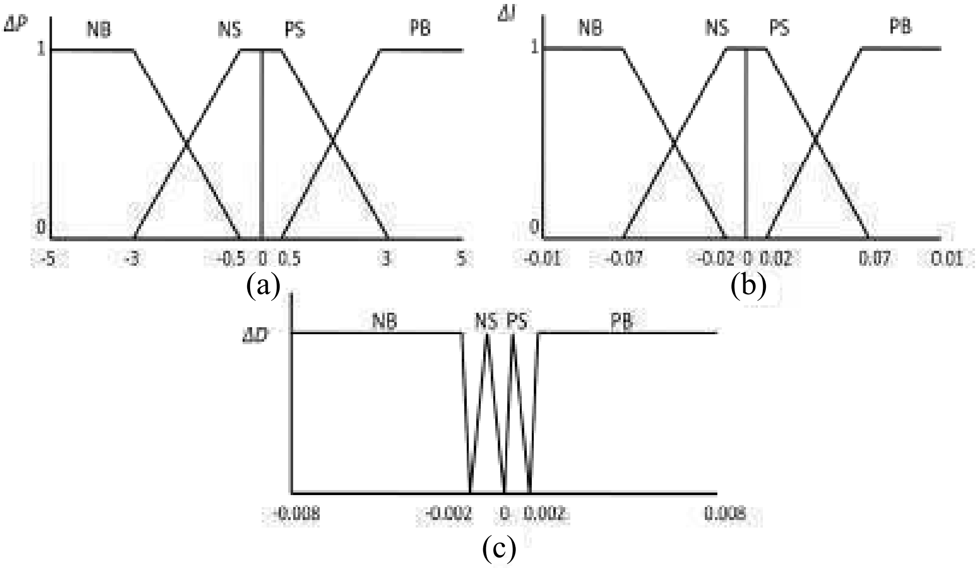

Figure 3.4. Membership functions: (a) input ΔP, (b) input ΔI and (c) output ΔD.

The last stage of the fuzzy controller is the defuzzification where the centre of area algorithm (COA) is used to convert the fuzzy subset duty cycle changes to real numbers.

$$\Delta D = \frac{\sum_{i}^{n} \mu(D_i) D_i}{\sum_{i}^{n} \mu(D_i)} \tag{3.5}$$

where ΔD is the fuzzy controller output and D_i is the centre of Max-Min composition at the output membership function.

The FLC computes the variable step sizes to increment or decrement the duty cycle, therefore the tracking time is short and the system performance during steady-state conditions is much better than with the conventional hill climbing algorithm. Moreover, the divergence problem no longer exists since the controller input, change of power (*dP*), reverses its direction in response to variation in atmospheric conditions.

3.4 Results and discussion

The tested PV array is composed of three series models with rated power of 150 W, where the design specification and circuit parameters are shown in table 3.1. Figure 3.5 shows a comparison of the PV output power characteristics which demonstrates the effectiveness of the proposed FLC compared to conventional hill climbing.

Table 3.1. Design specification and circuit parameters.

Item			Value
PV array rated Power,	P	*(W)*	150
Boost inductor,	L	*(H)*	0.3
Smoothing capacitor,	C	*(mF)*	2
Output voltage,	V	*(V)*	85
Switching frequency,	f_s	*(kHz)*	4

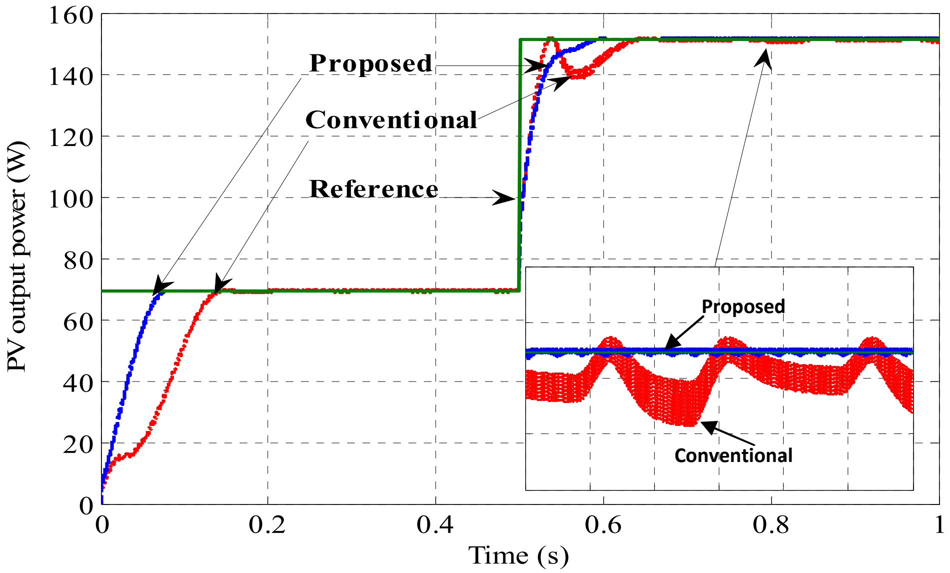

Figure 3.5. PV output power characteristics for conventional and the proposed modified hill climbing methods.

From Figure 3.5, the proposed MPPT performs better than conventional hill climbing, with the proposed MPPT convergence time being faster, has no oscillation at steady state, and the MPP is directly extracted under varying weather conditions.

To verify the advantages of the proposed controller, Figure 3.6 represents the controller output, which is a plot of the duty cycle versus time. The optimum duty cycle is reached faster and with less oscillation around the optimum value than with conventional hill climbing. Moreover, during solar radiation changes, the duty cycle moves toward the optimum value.

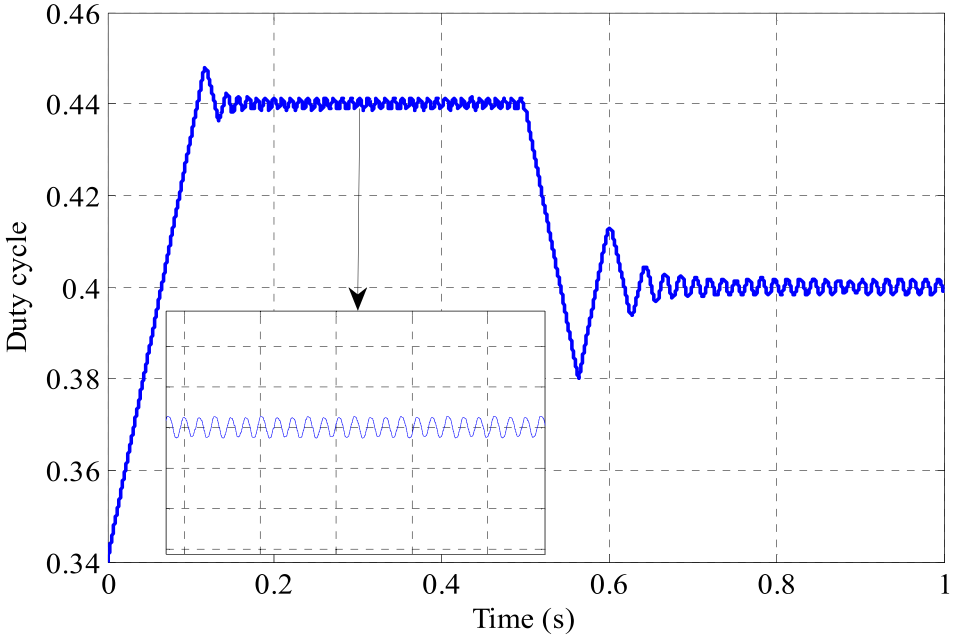

Figure 3.6. The advantages of modified hill climbing based on FLC.

The first two disadvantages of the hill climbing searching method, defined in section 3.2, are inherently eliminated via the FLC, since the increment and decrement step size is varied according to the location of ΔP and ΔI. The fuzzy rules force the step size to increase as long as the system is operating away from the optimum point and vice versa. However, the third disadvantage remains, where the explanation of the phenomena can be understood from Figure 3.7. This figure represents the behaviour of the FLC inputs and output during different operation periods; namely initial, steady state and under new weather conditions, initially and in steady state.

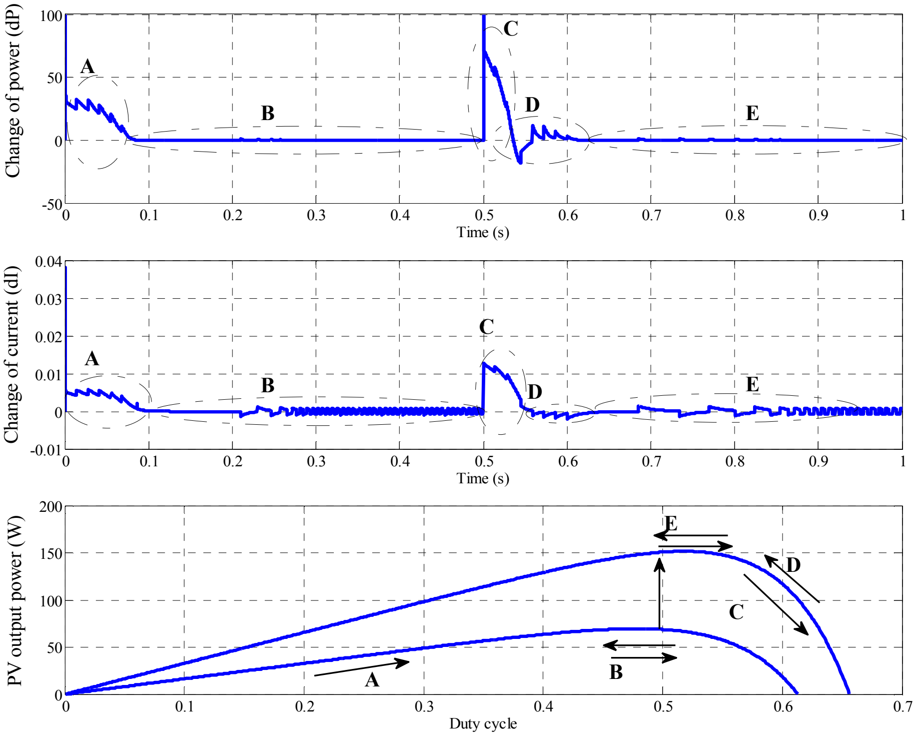

Figure 3.7. The power direction of PV array system under varying irradiance: (a) power change, (b) current change and (c) P-D characteristic under two different irradiance conditions.

In Figure 3.7, during period A, the changes of power and current are *positive big* therefore the duty cycle change is also *positive big*. As the PV power reaches maximum power, during period B, both the changes of power and current are almost zero, therefore the change of duty cycle is small, approaching zero. During varying weather conditions, the PV operating power moves from period B to C and continues to move until the change of power becomes negative, period D, at which point the control system detects that operation is diverging from the MPP. Therefore, the duty cycle change is reversed to the correct direction, to reach period E, which is the maximum operating point.

By inspection, ΔP only becomes *positive big* under two conditions; initial system operator and varying weather conditions. Therefore, to prevent diverging from the MPP, the sign of ΔP should only be reversed under varying weather conditions. Thus the proposed FLC has controlled gain on the fuzzy ΔP input. The controlled gain neglects the first 'positive big' value of ΔP since this represents the initial operating condition, subsequently the controlled gain will change the ΔP sign to negative. In this case, the power direction shown in Figure 3.7c will move from B directly to D under irradiance changes.

Load increase effects on the PV output power for the proposed technique and the conventional hill climbing technique are seen in Figure 3.8. Unlike conventional hill climbing, the proposed technique is not significantly affected by the load variation (either increase or decrease) since the FLC quickly locates the new optimum duty cycle. Conversely, conventional hill climbing tracks initially in the wrong direction for the new optimum duty cycle; before correcting its direction.

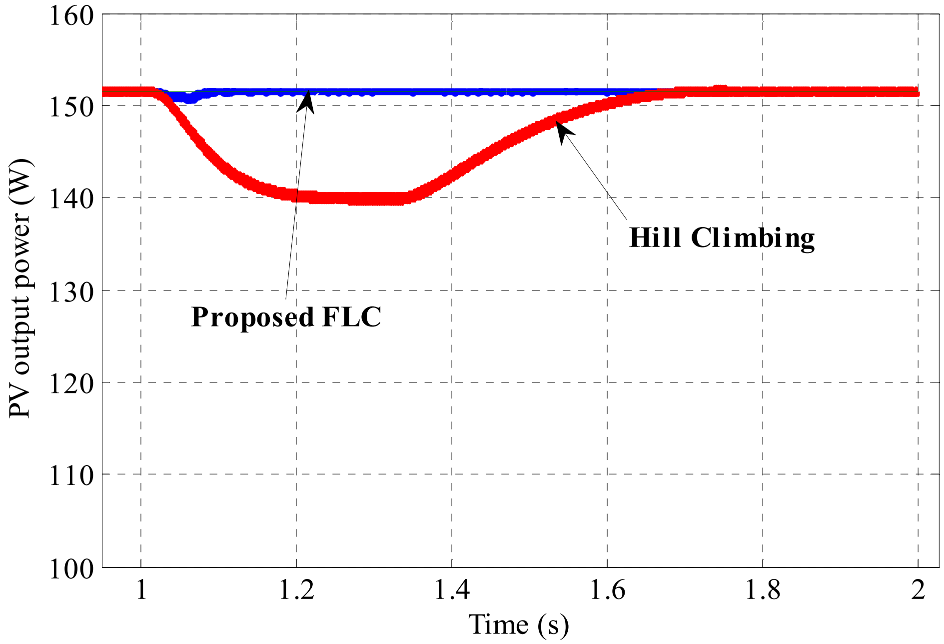

Figure 3.8. The proposed and conventional technique responses during load change.

To validate the robustness of the proposed technique, the comparison in Figure 3.9 between the proposed method and two other FLCs is presented. All the techniques offer good tracking speed and low variation around the MPP. However, during varying weather conditions, the FLC in [3.11] miss-tracks the new optimum point, which could result in failing to track the MPP under quickly varying weather conditions. Moreover, the FLC functions by computing the PV derivative *dP/dI* and the change of the derivative as inputs, which could result in practical controller implementation difficulties, especially in a noisy environment. The FLC in [3.12] is proposed to improve the MPPT dynamic performance under varying weather conditions in [3.11], by considering the duty cycle in the FLC input. Nevertheless, the tracking accuracy is limited as showing in Figure 3.9. Further validation of the considered techniques is shown in Table 3.2, by comparing the proposed technique with existing FLCs for MPPT. As shown in Table 3.2, the proposed technique gives good tracking speed, small oscillation, good accuracy, has fewer fuzzy rules, and no PI controller is needed.

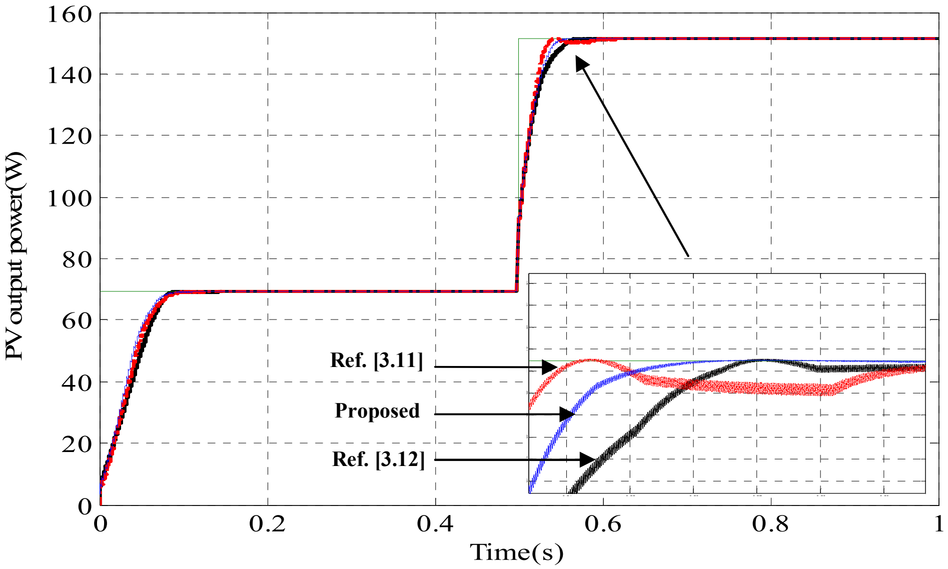

Figure 3.9. Simulation results of the propose technique and two other fuzzy trackers.

Table 3.2. Comparison between the proposed algorithm and the literature.

	Dynamic performance	Tracking accuracy	Number of Fuzzy rules	Execution speed time	Practical validation
Proposed	Good	Good	16	Low	Yes
[3.11], Won	Bad	Good	25	Medium	Yes
[3.12], Simoes	Good	Bad	15	Low	Yes
[3.13], Masoum	Good	Good	74	Large	Yes
[3.14], Kottas	Good	Good	25	High	No
[3.15], Cheikh	Good	Good	25	Medium	No

3.5 Experimental results

The performance of the proposed fuzzy logic control approach is verified experimentally with the configuration shown in Figure 3.10. The system consists of a variable dc supply in series with a variable resistor and a dc-dc boost converter with a 4 kHz switching frequency. The PV source is simulated by the dc voltage supply plus the series resistor, where the dc supply voltage level changes represent radiation variation, while temperature variation is simulated by changing the resistor value. An Infineon TriCore™ TC1796 is used to realise the proposed controller.

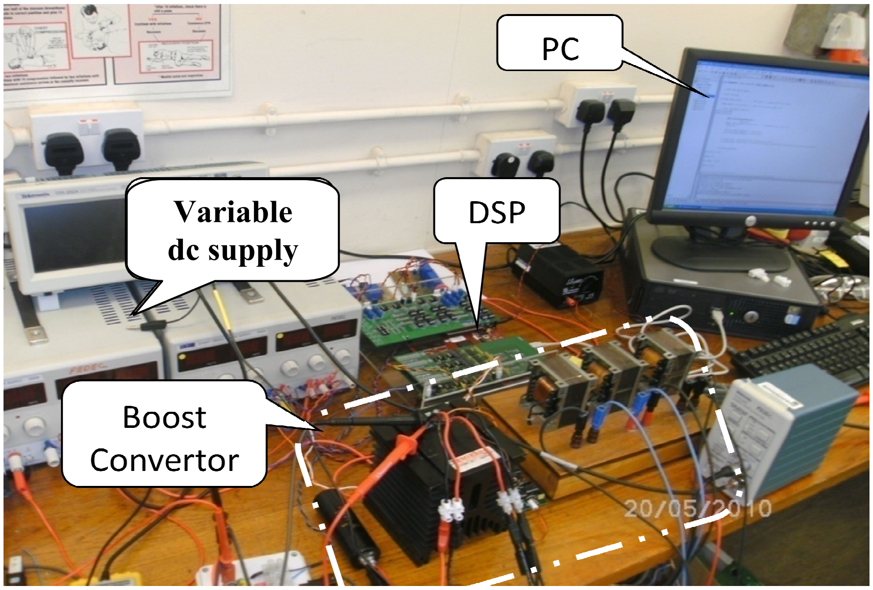

(a)

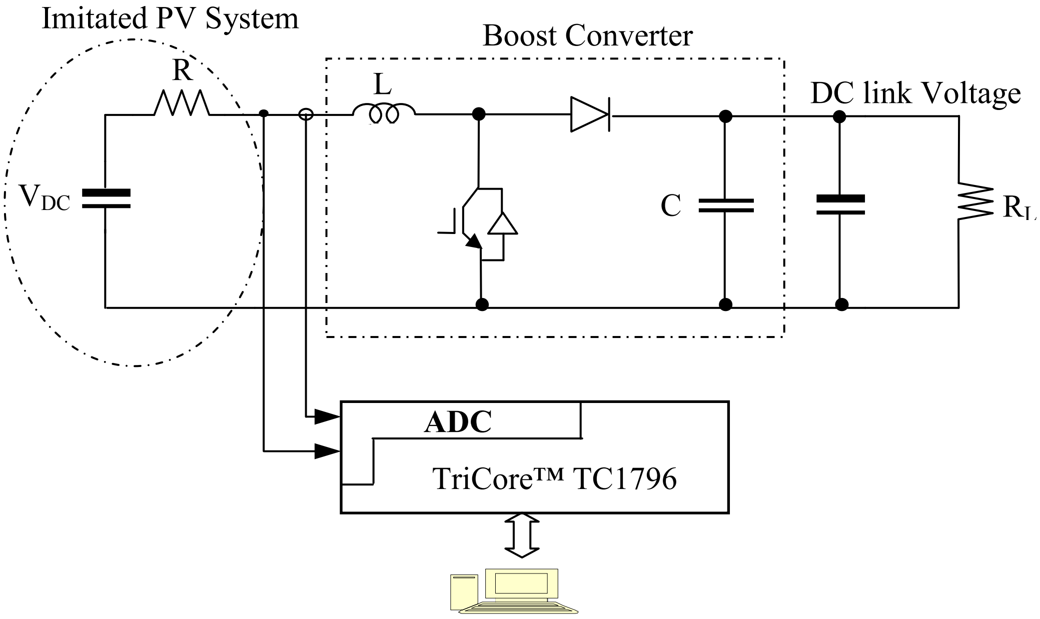

(b)

Figure 3.10. (a) Test rig photograph and (b) hardware diagram arrangement.

The experimental system is tested under different, stepped operating conditions. Figure 3.11 shows the results of the proposed MPPT. In each operating condition, the MPP is attained in a relatively short time and has a small oscillation in steady state. Moreover, when the weather conditions are changed, the proposed FLC forces the power to move directly to the new optimum point.

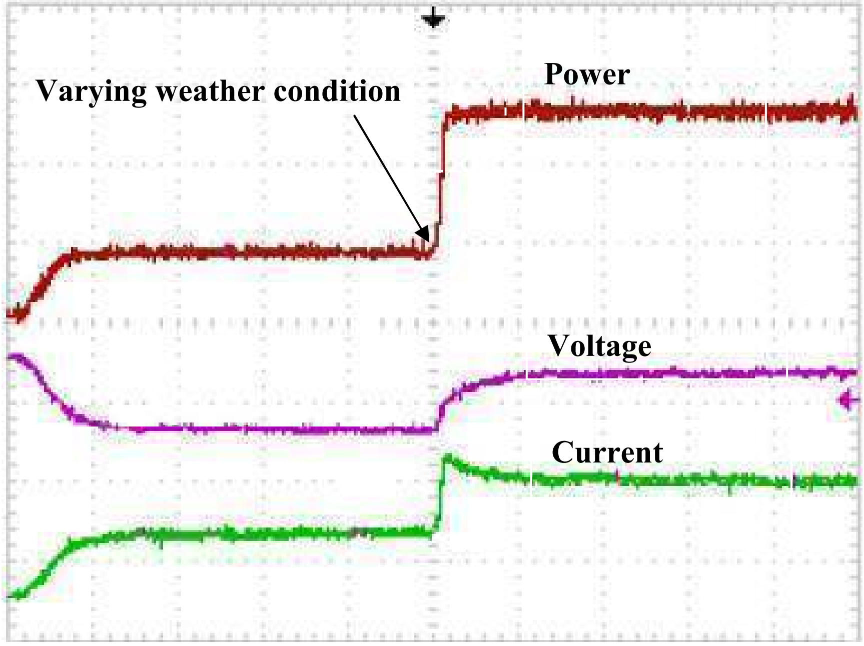

Time: 5s/div, P_o: 10 *W*/div, V_o: 10 *V*/div, i_o: 1 *A*/div

Figure 3.11. Experimental results for the proposed MPPT approach.

The practical results of the proposed MPPT and conventional hill climbing are shown in Figure 3.12 parts a and b, respectively. The responses in Figure 3.12a confirm the effectiveness of the proposed MPPT method over hill climbing. It is observed that the maximum power is attained faster with the proposed tracker and has smaller oscillation than with conventional hill climbing.

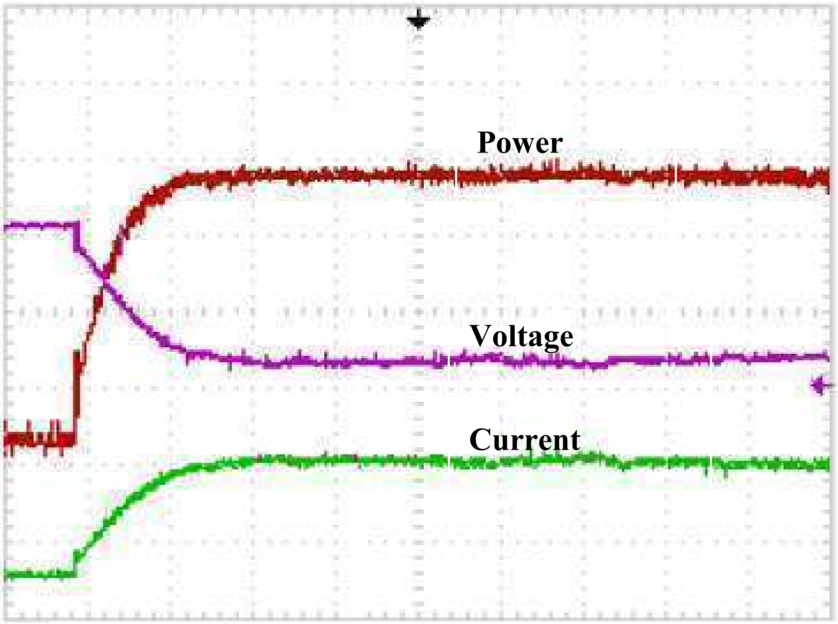

Time: 5s/div, P_o: 5 W/div, V_o: 10 V/div, i_o: 0.5 A/div

(a)

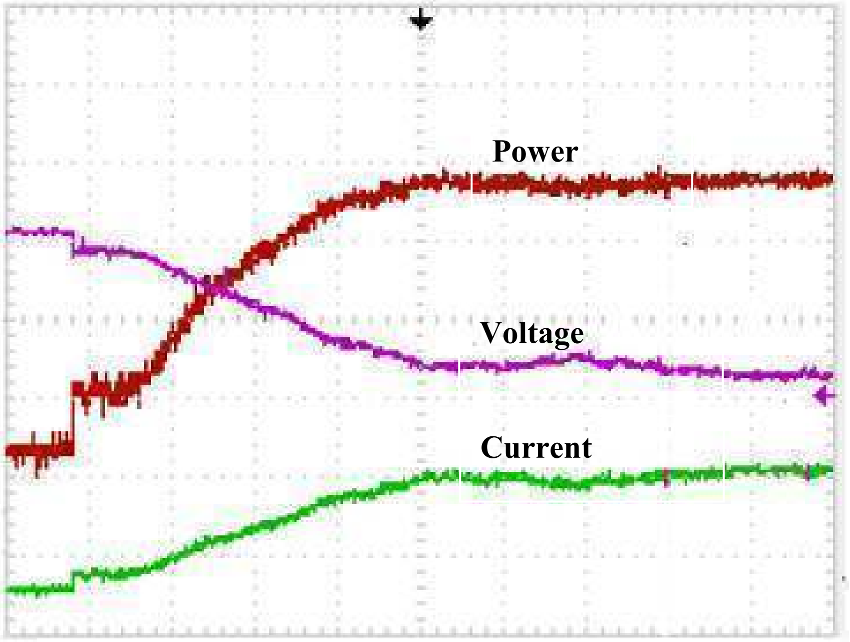

Time: 5s/div, P_o: 5 W/div, V_o: 10 V/div, i_o: 0.5 A/div

(b)

Figure 3.12. Experimental results: (a) proposed MPPT and (b) conventional hill climbing MPPT method.

3.6 Summary

In this chapter, the hill climbing search method has been modified based on fuzzy logic control, to cater for MPPT under rapidly changing weather conditions. The proposed MPPT approach was implemented by fuzzifying the rules of the hill climbing search methods to reduce its disadvantages, with a relatively simple approach. A Simulink model and practical experiments were used to verify the outcome of both conventional hill climbing and the proposed approach. The results of the proposed MPPT exhibit faster convergence, less oscillation around the MPP under steady-state conditions, and no divergence from the MPP during varying weather conditions. The feasibility and effectiveness of the proposed method were evaluated with different simulation studies and compared with existing fuzzy logic controller MPPT techniques. Partial shadowing is expected in PV arrays, where the radiation intensities are unequally distributed around the PV module or when some parts of the PV module go out of service.

References

[3.1] H. Chihchiang, L. Jongrong, and S. Chihming, "Implementation of a DSP-controlled photovoltaic system with peak power tracking," Industrial Electronics, IEEE Transactions on, vol. 45, pp. 99-107, 1998.

[3.2] M. G. Villalva, J. R. Gazoli, and E. R. Filho, "Comprehensive Approach to Modeling and Simulation of Photovoltaic Arrays," Power Electronics, IEEE Transactions on, vol. 24, pp. 1198-1208, 2009.

[3.3] M. A. Masoum, H. Dehbonei, and E. F. Fuchs, "Theoretical and Experimental Analyses of Photovoltaic Systems with Voltage and Current-Based Maximum Power Point Tracking," Power Engineering Review, IEEE, vol. 22, pp. 62-62, 2002.

[3.4] T. Noguchi, S. Togashi, and R. Nakamoto, "Short-current pulse-based maximum-power-point tracking method for multiple photovoltaic-and-converter module system," Industrial Electronics, IEEE Transactions on, vol. 49, pp. 217-223, 2002.

[3.5] L. Fangrui, D. Shanxu, L. Fei, L. Bangyin, and K. Yong, "A Variable Step Size INC MPPT Method for PV Systems," Industrial Electronics, IEEE Transactions on, vol. 55, pp. 2622-2628, 2008.

[3.6] T. Esram, J. W. Kimball, P. T. Krein, P. L. Chapman, and P. Midya, "Dynamic Maximum Power Point Tracking of Photovoltaic Arrays Using Ripple Correlation Control," Power Electronics, IEEE Transactions on, vol. 21, pp. 1282-1291, 2006.

[3.7] N. Femia, G. Petrone, G. Spagnuolo, and M. Vitelli, "Optimizing duty-cycle perturbation of P&O MPPT technique," in Power Electronics Specialists Conference, 2004. PESC 04. 2004 IEEE 35th Annual, 2004, pp. 1939-1944 Vol.3.

[3.8] N. Dasgupta, A. Pandey, and A. K. Mukerjee, "Voltage-sensing-based photovoltaic MPPT with improved tracking and drift avoidance capabilities," Solar Energy Materials and Solar Cells, vol. 92, pp. 1552-1558, 2008.

[3.9] A. Pandey, N. Dasgupta, and A. K. Mukerjee, "High-Performance Algorithms for Drift Avoidance and Fast Tracking in Solar MPPT System," Energy Conversion, IEEE Transactions on, vol. 23, pp. 681-689, 2008.

[3.10] L. Fangrui, K. Yong, Z. Yu, and D. Shanxu, "Comparison of P&O and hill climbing MPPT methods for grid-connected PV converter," in Industrial Electronics and Applications, 2008. ICIEA 2008. 3rd IEEE Conference on, 2008, pp. 804-807.

[3.11] W. Chung-Yuen, K. Duk-Heon, K. Sei-Chan, K. Won-Sam, and K. Hack-Sung, "A new maximum power point tracker of photovoltaic arrays using fuzzy controller," in Power Electronics Specialists Conference, PESC '94 Record., 25th Annual IEEE, 1994, pp. 396-403 vol.1.

[3.12] M. G. Simoes and N. N. Franceschetti, "Fuzzy optimisation based control of a solar array system," Electric Power Applications, IEE Proceedings -, vol. 146, pp. 552-558, 1999.

[3.13] M. A. S. M. a. M.Sarvi, "Design, simulation and construction of a new fuzzy-based maximum power point tracker for photovoltaic applications," Iranian Journal of Science and Technology, vol. 29, pp. 1-10, 2005.

[3.14] T. L. Kottas, Y. S. Boutalis, and A. D. Karlis, "New maximum power point tracker for PV arrays using fuzzy controller in close cooperation with fuzzy cognitive networks," Energy Conversion, IEEE Transactions on, vol. 21, pp. 793-803, 2006.

[3.15] C. Larbes, S. M. Aït Cheikh, T. Obeidi, and A. Zerguerras, "Genetic algorithms optimized fuzzy logic control for the maximum power point tracking in photovoltaic system," Renewable Energy, vol. 34, pp. 2093-2100, 2009.

[3.16] T. F. Wu, C. H. Yang, Y. K. Chen, and Z. R. Liu, "Photovoltaic inverter systems with self-tuning fuzzy control based on an experimental planning method," in Industry Applications Conference, 1999. Thirty-Fourth IAS Annual Meeting. Conference Record of the 1999 IEEE, 1999, pp. 1887-1894 vol.3.

[3.17] N. Femia, G. Petrone, G. Spagnuolo, and M. Vitelli, "Optimization of perturb and observe maximum power point tracking method," Power Electronics, IEEE Transactions on, vol. 20, pp. 963-973, 2005.

[3.18] X. Weidong and W. G. Dunford, "A modified adaptive hill climbing MPPT method for photovoltaic power systems," in Power Electronics Specialists Conference, 2004. PESC 04. 2004 IEEE 35th Annual, 2004, pp. 1957-1963 Vol.3.

[3.19] N. Femia, G. Petrone, G. Spagnuolo, and M. Vitelli, "A Technique for Improving P&O MPPT Performances of Double-Stage Grid-Connected Photovoltaic Systems," Industrial Electronics, IEEE Transactions on, vol. 56, pp. 4473-4482, 2009.

[3.20] S. Jain and V. Agarwal, "A new algorithm for rapid tracking of approximate maximum power point in photovoltaic systems," Power Electronics Letters, IEEE, vol. 2, pp. 16-19, 2004.

[3.21] S. Jain and V. Agarwal, "Comparison of the performance of maximum power point tracking schemes applied to single-stage grid-connected photovoltaic systems," Electric Power Applications, IET, vol. 1, pp. 753-762, 2007.

[3.22] B. Szabados and W. Fangnan, "A Maximum Power Point Tracker Control of a Photovoltaic System," in Instrumentation and Measurement Technology Conference Proceedings, 2008. IMTC 2008. IEEE, 2008, pp. 1074-1079.

[3.23] H. Ying-Tung and C. China-Hong, "Maximum power tracking for photovoltaic power system," in Industry Applications Conference, 2002. 37th IAS Annual Meeting. Conference Record of the, 2002, pp. 1035-1040 vol.2.

[3.24] J. Youngseok, S. Junghun, Y. Gwonjong, and C. Jaeho, "Improved perturbation and observation method (IP&O) of MPPT control for photovoltaic power systems," in Photovoltaic Specialists Conference, 2005. Conference Record of the Thirty-first IEEE, 2005, pp. 1788-1791.

[3.25] S. V. Kartalopoulos and I. N. N. Council, Understanding neural networks and fuzzy logic: basic concepts and applications: Institute of Electrical and Electronics Engineers, 1996.

Chapter 4

A Maximum Power Point Tracking Technique for Partially Shaded Photovoltaic Systems

This chapter reviews the state of art and recent research developments on MPPT under partial shading conditions. Also, a new mathematical model of a PV system under partial shading conditions is derived. Then a modified fuzzy-logic controller for maximum power point tracking is proposed to increase PV system performance during partially shaded conditions. Instead of perturbing and observing the PV system maximum power point, the controller scans and stores the maximum power during the perturbing and observing procedure. The controller offers accurate convergence to the global maximum operating point under different partial shading conditions. To validate the proposed modified fuzzy-logic based controller, simulation and experimental results are provided.

4.1 Background

During partial shaded conditions, the system power-voltage characteristic curve has multiple peaks [4.1]. Therefore, a conventional maximum power point tracker (MPPT) such as hill climbing, incremental conductance, or ripple correlation trackers, could miss the global maximum point [4.2-6].

A study of partial shading conditions in [4.7] shows that using conventional MPPT could result in significant losses of PV output power. Moreover, the PV energy system reliability could experience a significant reduction during partial shading conditions [4.8]. Therefore, different researchers have investigated improving tracking efficiency. Reference [4.9] proposes short circuit pulse based MPPT with fast scan on the power-voltage curve to identify the proportional parameter which is commonly used in current-based MPPT [4.10]. The global maximum point is found, however an additional switch in parallel with the PV source is required to compute the short circuit current every few minutes. Such methods cause momentarily power losses and incur additional cost. To avoid using an extra switch, the authors in [4.11] propose a controller that swings the converter's duty cycle from 0 to 1 to measure the open circuit voltage and the short circuit current and then computes the optimum voltage and current. From the computed values, the operating point is moved in one step to the optimal operating point. The conventional hill climbing algorithm is used to maintain operation around the maximum point. Local maxima are avoided, however significant loss in power is experienced during the computation of the open circuit voltage and the short circuit current.

Based on observation and investigation of the PV characteristic, the authors in [4.12] claim that on either side of the global maximum point, the local maxima consistently decrease. Therefore, an MPPT scheme for a PV system under partially shaded conditions is proposed based on this observation. In [4.13], simulation of a partially shaded PV system rejects the observation of [4.12] and MPPT based on conventional hill climbing and a partial shading identifier is proposed. Also, it has been observed [4.13] that the global maximum point under non-uniform conditions is always located to the left of maximum power at normal weather conditions. Therefore a trajectory line of the PV system under different isolation levels is stored in a data based memory to identify the partial shaded conditions. Such a technique could save the controller from unnecessary global scanning, however the trajectory line is different between PV systems and also the PV parameters vary with time.

A line search algorithm with a Fibonacci sequence has been employed to track the global power point under partially shaded conditions. However this method can miss the global MPP in some shaded conditions [4.14]. In [4.15] a direct search algorithm is employed to search the Lipschitz function which describes the PV power and voltage relationship in an interval. In order for this method to ensure finding the global maximum power, the initial point must be carefully selected otherwise the controller may be trapped at a local maxima power point. Particle swarm optimization has been implied to track the maximum global operating point under abnormal weather conditions. A large time delay is required to allow agents to compute the global maximum point, resulting in a long computation time to reach the maximum operating point [4.16, 17].

Two stage MPPT using monitoring cells has been proposed in [4.18], where the operating point in the first stage moves to the MPP by assuming that the power-voltage curve is uniform. In the second stage the incremental conductance method is used to locate the real MPP. It could overlook the global MPP in some partial shading conditions; and also open circuit voltage and short circuit current measurements are required.

To reduce the partial shading effect, an adaptive solar photovoltaic array is proposed [4.19]. A model-based control algorithm is used to control a switching matrix that connects a solar adaptive bank to a fixed part of the PV array. Similarly, dynamic electrical array re-configuration is proposed [4.20] to improve the PV energy production during partial shading conditions. A controllable switching matrix is inserted between the PV generator and the central inverter to allow electrical reconnection of the available PV modules. In [4.21] reconnection of the PV arrays at regular time intervals is proposed to reduce the partial shading effect. In these approaches conventional MPPT can be applied to extract the MPP, however power stage complexity and cost are increased.

In this chapter, a fuzzy-logic-based hill climbing technique is proposed to track the global maximum point in a non-uniform power-current curve characteristic. The technique identifies the global maximum among any number of local maxima. Unlike conventional MPPT where the PV system operating power is perturbed and observed to track the maximum power point, the proposed controller scans and stores the maximum power during the perturbation and observation stage. Moreover, PV modelling during partial shading conditions is proposed. Computer-aided simulation and experimentation are used to demonstrate the effectiveness and robustness of the proposed control method.

4.2 PV modelling under partial shading

During shading conditions, the PV system mathematical model is no longer valid because different radiation levels are distributed around the PV system [4.22]. Therefore, a new mathematical model is required to represent the PV system under partial shading conditions. An extensive study has been undertaken of different PV module connections to derive a general PV mathematical model under shading conditions.

For simplicity, three series connected PV modules are considered. Based on the data for the Shell SP 150-PC, the short circuit current I_{sc} and the open circuit voltage V_{oc} for each PV module under the rated radiation level are 4.4A and 43.4V respectively. One PV module is partially shaded and it receives a radiation of 500W/m^2 while the other two modules receive the rated radiation of 1000W/m^2. The *I-V* characteristic and PV system block diagram are shown in Figure 4.1. Three points in Figure 4.1b are considered; first point one - where the current equals I_{sc} and the voltage is zero, point two - where the current equals I_{step} and voltage equals V_{step}, and point three - where the current is zero and the voltage equals V_{oc}. By inspection, the previous variables can be defined as:

- I_{sc} is the short circuit current of the unshaded PV modules.
- I_{step} is the short circuit current of the shaded PV module.
- V_{step} is the summation of the open circuit voltage of the unshaded modules.
- V_{oc} is the summation of the open circuit voltage of the shaded and unshaded modules.

From these observations the mathematical model of the given PV system is:

$$V_{pv} = \begin{cases} \dfrac{AkTn_s^{us}}{q} ln(\dfrac{I_{sc}.\lambda^{us} - I_{pv}}{I_o}) \quad \ldots\ldots\ldots\ldots\ldots\ldots\ldots\ldots\ldots\ldots\ldots \quad I_{pv} > I_{step} \\ \dfrac{AkTn_s^{us}}{q} ln(\dfrac{I_{sc}.\lambda^{us} - I_{pv}}{I_o}) + \dfrac{AkTn_s^{s}}{q} ln(\dfrac{I_{sc}.\lambda^{s} - I_{pv}}{I_o}) \quad \ldots \quad I_{pv} < I_{step} \end{cases} \tag{4.1}$$

where n_s^{us} and n_s^{s} are the numbers of series unshaded and series shaded modules respectively, and λ^{us} and λ^{s} are the radiation levels on the unshaded and shaded modules respectively.

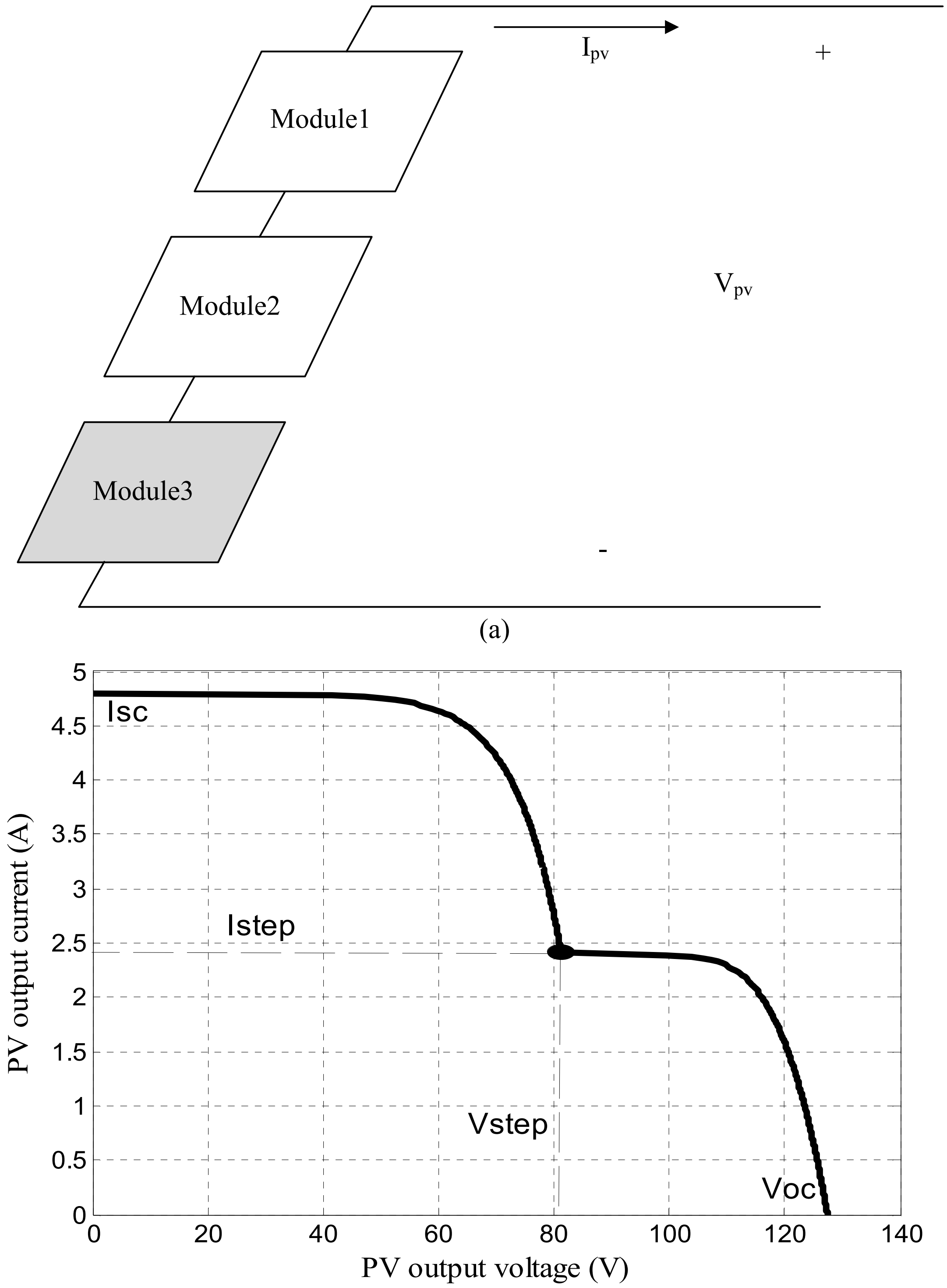

(a)

(b)

Figure 4.1. (a) Block diagram of a three series connected PV modules system and (b) characteristic curve of the PV output current and voltage.

Equation (4.1) is valid for two radiation levels distributed along the series connected PV modules. Therefore, equation (4.1) is extended to cater for three radiation levels, as in equation (4.2). When the radiation distribution levels increase, the number of voltage/current steps increase. Figure 4.2 shows the *I-V* characteristic of three series connected PV modules with different shading levels. The PV system shown in Figure 4.1a is tested under different partial shading conditions. Two PV modules are partially shaded and receive two different radiation levels, 500W/m^2 and 300W/m^2, and the third module receives rated radiation, 1000W/m^2. Two more observations are added to the previous observations:

- I_{step2} is the short circuit current of the shaded PV modules with the highest radiation level.
- V_{step1} is the open circuit voltage of the unshaded modules plus the summation of the shaded modules open circuit voltage without the open circuit voltage of the lowest radiation module.

Therefore the mathematical model for three different radiation levels on three series connected PV modules is:

$$V_{pv}=\begin{cases} \sum\frac{AkTn_s^{us}}{q}ln(\frac{I_{sc}.\lambda^{un}-I_{pv}}{I_o}) & I_{pv}>I_{2step} \\ \sum\frac{AkTn_s^{us}}{q}ln(\frac{I_{sc}.\lambda^{un}-I_{pv}}{I_o})+\frac{AkTn_s^{s1}}{q}ln(\frac{I_{sc}.\lambda^{s1}-I_{pv}}{I_o}) & I_{1step}<I_{pv}<I_{2step} \\ \sum\frac{AkTn_s^{us}}{q}ln(\frac{I_{sc}.\lambda-I_{pv}}{I_o})+\frac{AkTn_s^{s1}}{q}ln(\frac{I_{sc}.\lambda^{s1}-I_{pv}}{I_o})+\frac{AkTn_s^{s2}}{q}ln(\frac{I_{sc}.\lambda^{s2}-I_{pv}}{I_o}) & I_{pv}<I_{1step} \end{cases} \quad (4.2)$$

where n_s^{s1} is the number of the partially shaded PV modules with the lowest radiation level and n_s^{s2} is the number of the partially shaded PV modules with the highest radiation level. λ^{s1} is the lowest radiation level and λ^{s2} is the highest radiation level.
From equations 4.1 and 4.2, the general mathematical model of *n*-series connected PV modules in a PV system is:

$$V_{pv}=\begin{cases}\sum \frac{AkTn_s^{us}}{q} ln(\frac{I_{sc}.\lambda^{un}-I_{pv}}{I_o}) & I_{pv}>I_{Nstep} \\ \vdots & \vdots \\ \sum \frac{AkTn_s^{us}}{q} ln(\frac{I_{sc}.\lambda^{un}-I_{pv}}{I_o})+\frac{AkTn_s^{s1}}{q} ln(\frac{I_{sc}.\lambda^{s1}-I_{pv}}{I_o}) & I_{1step}<I_{pv}<I_{2step} \\ \sum \frac{AkTn_s^{us}}{q} ln(\frac{I_{sc}.\lambda-I_{pv}}{I_o})+\frac{AkTn_s^{s1}}{q} ln(\frac{I_{sc}.\lambda^{s1}-I_{pv}}{I_o})+....+\frac{AkTn_s^{sN}}{q} ln(\frac{I_{sc}.\lambda^{sN}-I_{pv}}{I_o}) & I_{pv}<I_{1step}\end{cases} \tag{4.3}$$

where n_s^{sN} is the number of the partially shaded PV modules with the highest radiation level and λ^{sN} is the highest radiation level. N is the number of the distributed radiation levels.

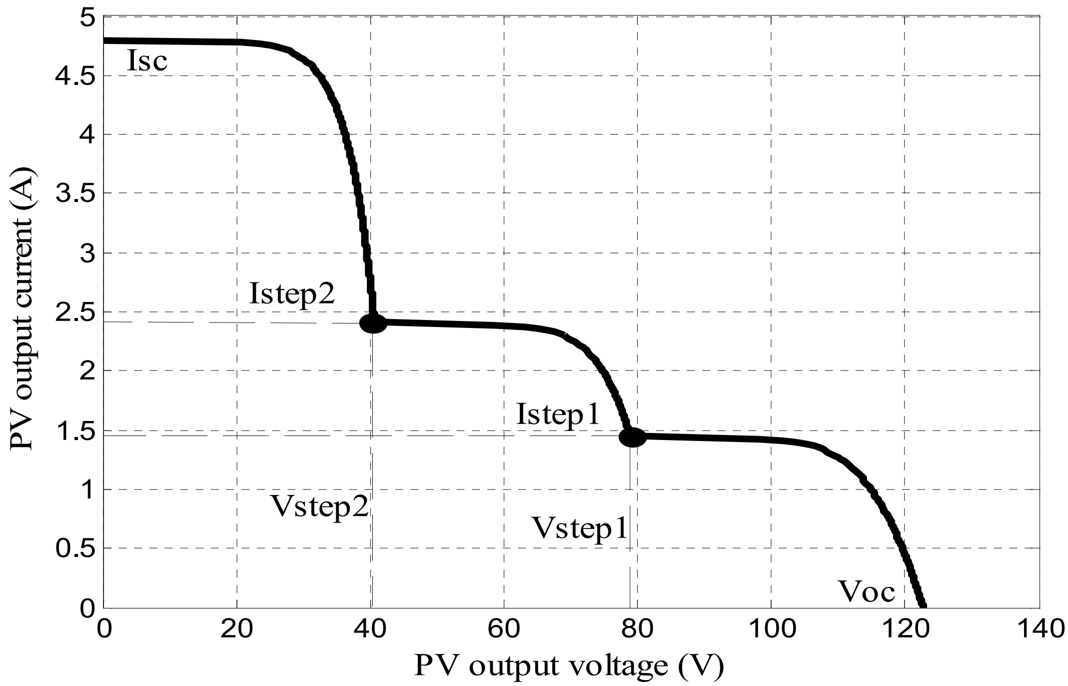

Figure 4.2. The characteristic curve of the PV output current and voltage.

Usually the PV system consists of parallel/series connected PV modules. Therefore to derive a mathematical model for the overall PV system, the previous three series connected PV modules are connected in parallel with another three series connected PV modules as shown in Figure 4.3a. For simplicity, the radiation levels are distributed as follow:

In the first branch, modules one and two receive radiation of 1000W/m^2 and the shaded module receives 500W/m^2. The three PV modules in the second branch are partially shaded to receive radiation of 300W/m^2. The *I-V* characteristic of the PV system is shown in Figure 4.3b. Curve A represents the *I-V* characteristic of the PV system, curve B represents the *I-V* characteristic of branch 1, and curve C represents the *I-V* characteristic of branch 2. The PV output current is the summation of the instant current from each branch.

$$I_{pvTotal} = I_{branch1} + I_{branch2} \tag{4.4}$$

From equation 4.4, the general mathematical model of *N*-parallel connected PV modules in the PV system is:

$$I_{pvTotal} = I_{branch1} + I_{branch2} + ... + I_{branchN} \tag{4.5}$$

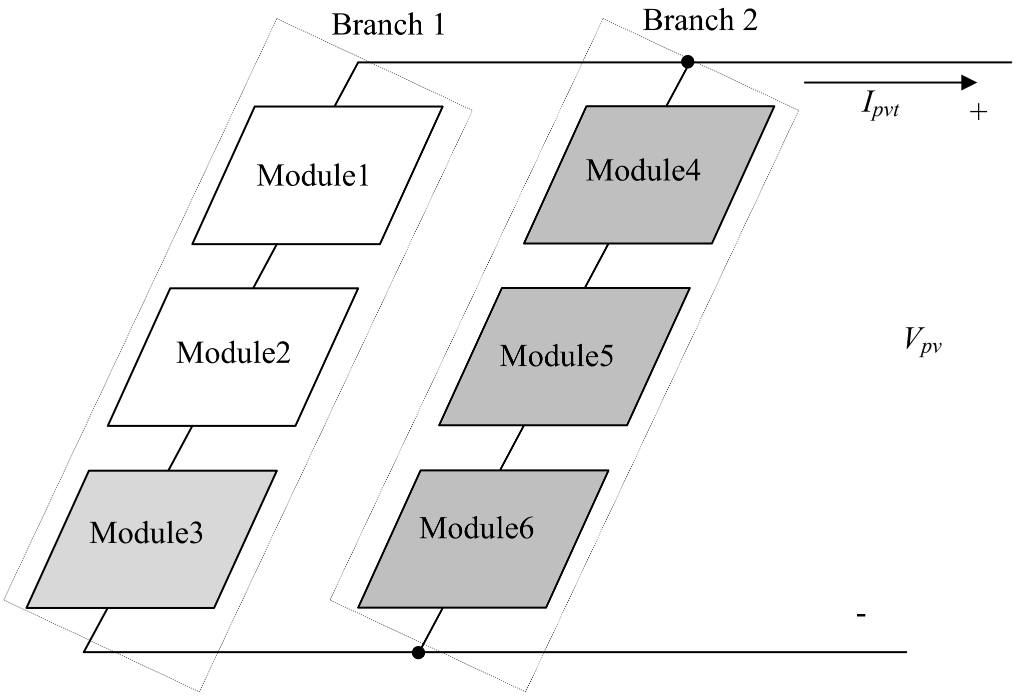

(a)

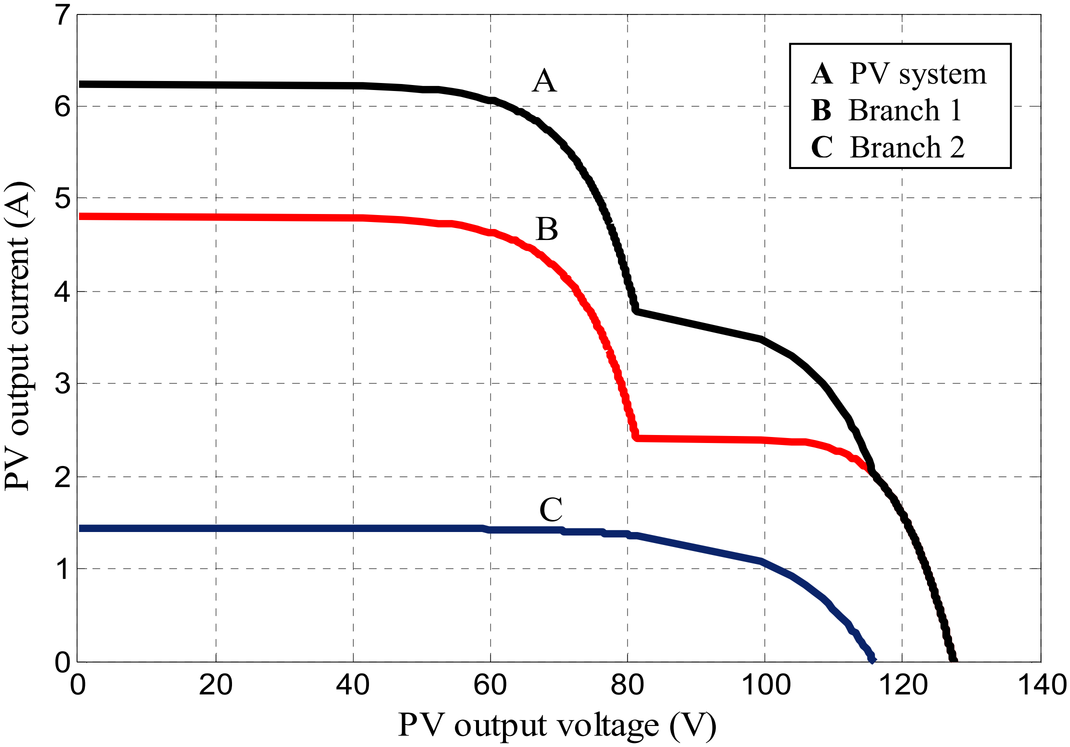

(b)

Figure 4.3. (a) Block diagram of the series/parallel connected PV module system and (b) characteristic curve of the PV output current and voltage.

4.3 Proposed method

Unlike conventional MPPTs where the PV system operating power is perturbed and observed to track the maximum power point, scanning, storing, perturbing, and observing the operating power of the PV system are used for the proposed MPPT. The method is able to track the maximum power point under any weather conditions; especially partial shading where local and global maximum points exist. During initial condition or varying weather conditions, the proposed MPPT makes a wide range search to scan and store the maximum power value of the PV system. A preset value which represents the accepted difference between the identified maximum power and the operating power is stored to decide the controller rules. If the difference between the identified maximum power and the operating power is greater than the preset value, the duty cycle is increased, otherwise fuzzy-logic-based MPPT is applied. In this case, the algorithm ensures that the MPPT is not trapped by local maxima and quickly recovers the new global maximum point during varying weather conditions. Unlike conventional scanning MPPT, the necessity of using a long time delay is not required because the controller scans the *P-V* curve while perturbation and observation is carried out. Figure 4.4 shows the flow chart of the proposed method, where V_{pv} are I_{pv} are the PV output voltage and current, D is the duty cycle, P_m is the global maximum power point, and ΔP_m is a constant that identifies the allowable difference between the global maximum and the operating power point.

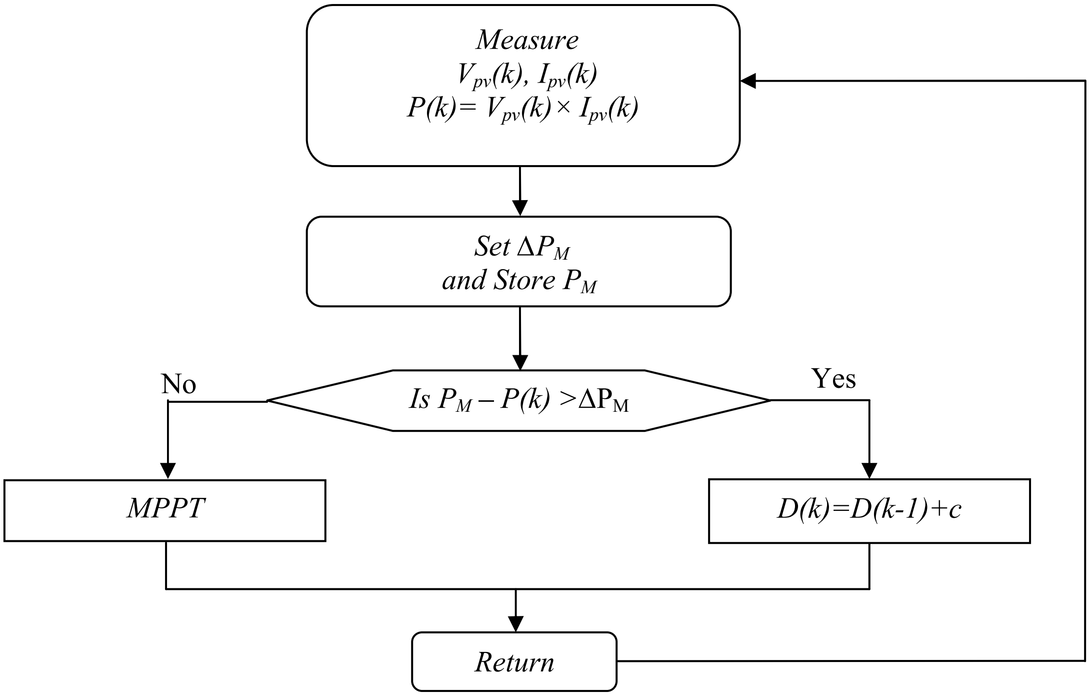

Figure 4.4. The proposed method flow chart.

Three scanning and storing techniques are proposed to identify the global maximum power during initial conditions or varying weather occasions.

The first is to initialize the system with maximum duty cycle, since the PV output power usually takes a few samples before reaching the operating point at maximum duty cycle. The PV characteristic curve is scanned and the global MPP is stored.

The second technique is to increase the duty cycle from the minimum to the maximum value with a fixed step. The PV curve is scanned and the global MPP is stored.

The last technique is to apply a large initial perturbation step to make a wide search range along the PV power locus. Unlike the previous two proposed techniques, scanning and storing the PV power is accomplished during perturbation and observation. The three techniques guarantee finding and storage of the global MPP, however the global identification time is different for each. Moreover, the duty cycle must return to a minimum value whenever it exceeds the maximum value to track the global MPP.

Any conventional MPPT method can be used with the proposed method; however, the proposed fuzzy-logic-based MPPT in chapter 3 is preferred, especially when using the third technique because the tracking speed is not constant. Therefore, during initial conditions or varying weather conditions, the initial tracking speed should be fast enough to make a wide range power scan and store the maximum available power. But when the operating point reaches the global maximum, tracking speed decreases to minimize any oscillation around the global maximum point. The PV system block diagram, along with the proposed controller, is shown in Figure 4.5.

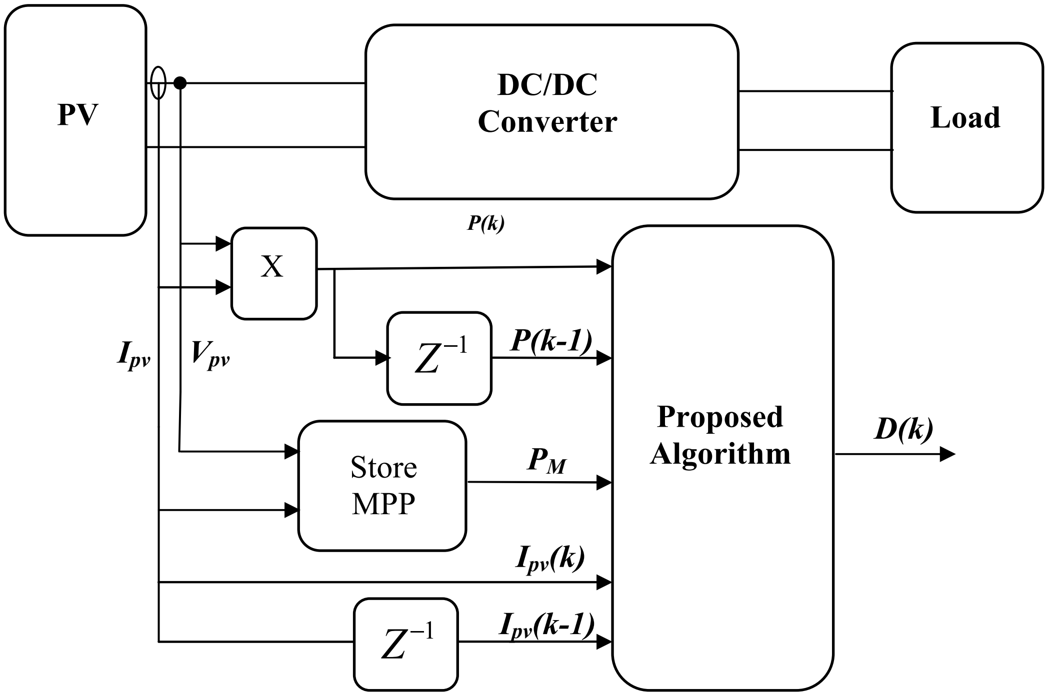

Figure 4.5. PV array system block diagram and the proposed MPPT controller.

4.4 Fuzzy logic control design

Modification to the fuzzy logic based MPPT algorithm, using a scanning and storing procedure, is proposed to quickly locate the global maximum power point. Fuzzification of the flow chart in Figure 4.4 is considered in the proposed MPPT design. The inputs to the FLC are:

$$\Delta P = P(k) - P(k-1) \tag{4.6}$$

$$\Delta I = I(k) - I(k-1) \tag{4.7}$$

$$\Delta P_M = P_m(k) - P(k) \tag{4.8}$$

and the output equation is:

$$\Delta D = D(k) - D(k-1) \tag{4.9}$$

where ΔP and ΔI are the PV array output power and current change, ΔP_M is the difference between the stored global maximum power P_M and the current power, and ΔD is the boost converter duty cycle change. To ensure that the PV global maximum power is stored during the scanning procedure, a fast initial tracking speed is used. The variable inputs ΔP and ΔI are divided into four fuzzy subsets: PB (*Positive Big*), PS (*Positive Small*), NB (*Negative Big*), and NS (*Negative Small*). The variable input ΔP_M is divided into two fuzzy subsets: PB and PS. The output variable ΔD is divided into six fuzzy subsets: PB, PM (*Positive Medium*), PS, NB, NM (*Negative Medium*), and NS. Therefore the fuzzy algorithm requires 32 fuzzy control rules; these rules are based on the regulation of a hill climbing algorithm along with the reference power. To operate the fuzzy combination, Mamdani's method with Max-Min is used [4.23]. The fuzzy rules are shown in Table 4.1.

Table 4.1. Fuzzy logic rules.

ΔI / ΔP	***NB***	***NS***	***PS***	***PB***	ΔP_M
NB	*PM*	*PM*	*NM*	*NM*	***PS***
NS	*PS*	*PS*	*NS*	*NS*	
PS	*NS*	*NS*	*PS*	*PS*	
PB	*NM*	*NM*	*PM*	*PM*	
NB	*PB*	*PB*	*PB*	*PB*	***PB***
NS	*PB*	*PB*	*PB*	*PB*	
PS	*PB*	*PB*	*PB*	*PB*	
PB	*PB*	*PB*	*PB*	*PB*	

After simulating the PV system and studying the behaviour of the controller inputs and output, the shapes and fuzzy subset partitions of the membership function in both the inputs and output are shown in Figure 4.6.

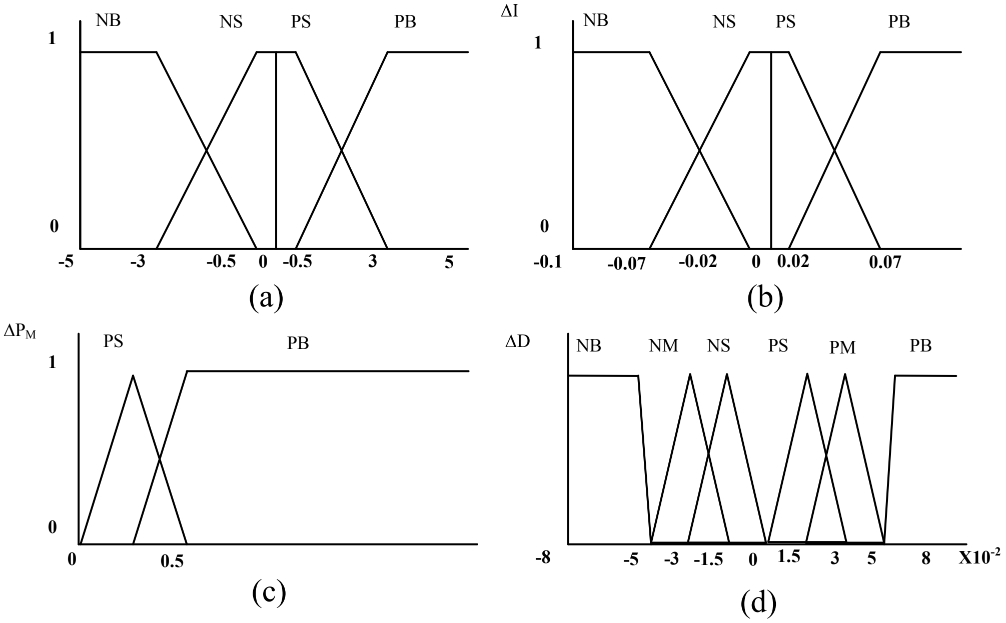

(a) (b) (c) (d)

Figure 4.6. Membership functions: (a) input ΔP, (b) input ΔI, (c) input $\Delta P_{M,}$ and (d) output ΔD.

The last fuzzy controller stage is defuzzification where the centre of the area algorithm (COA) is used to convert the fuzzy subset duty cycle changes to real numbers.

$$\Delta D = \frac{\sum_{i}^{n} \mu(D_i) D_i}{\sum_{i}^{n} \mu(D_i)} \tag{4.10}$$

where ΔD is the fuzzy controller output and D_i is the centre of the Max-Min composition at the output membership function.

4.5 Simulation results and discussion

The tested PV array is composed of ten series modules with rated power of 850W, where the design specification and circuit parameters are shown in table 4.2. The simulation results are carried out using Matlab/Simulink to validate the performance of the proposed MPPT. A large initial perturbation step is used to scan and store the global MPPT.

Table 4.2. Design specification and circuit.

Item	Value
PV array rated Power, P (W)	850
Boost inductor, L (H)	0.3
Smoothing capacitor, C (μF)	2200
Output voltage V (V)	300
Switching frequency, f_s (kHz)	4

4.5.1 Normal weather conditions

The proposed system is tested under two equally distributed radiation levels, 500W/m^2 and 1000W/m^2. As shown in figure 4.7, the global maximum scan causes some power loss during initial and varying weather conditions. Nevertheless, the proposed MPPT still attains the MPP in a relatively short time, with small oscillation in the steady state.

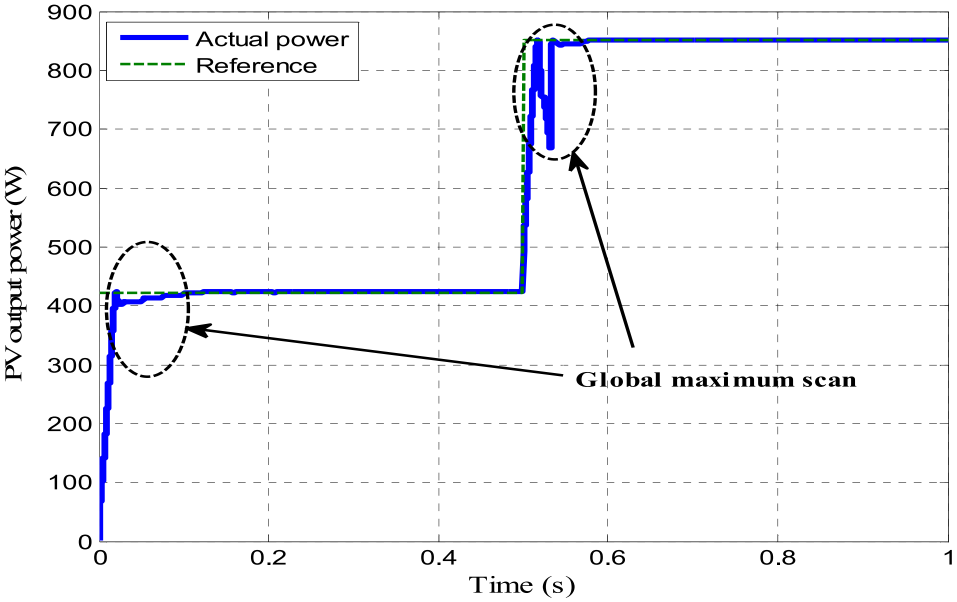

Figure 4.7. PV output power characteristic for the proposed MPPT under two radiation levels.

4.5.2 Partial Shading condition

To validate the performance of the proposed MPPT during partial shading, the PV system is tested under different distributed radiation levels; seven unshaded modules receive 1000 W/m^2 while the remaining three modules are partially shaded with radiation level of 800, 500 and 100 W/m^2 (Figures 4.8 and 4.9 Case1). The PV output power, along with the system power locus, is shown in Figure 4.8. The local maxima do not prevent the proposed controller from reaching the global maximum power point. In addition, the tracking of the global maximum is fast with small oscillation in the steady state. For further verification, the same partial shading conditions are repeated with different radiation levels of 500 W/m^2 on the unshaded modules (Figure 4.9 Case 2). The radiation level on the unshaded modules is then varied from 500 W/m^2 to 1000 W/m^2 at 0.5 second and then from 1000 W/m^2 to 500 W/m^2 at 1 second. From Figure 4.9, the proposed MPPT scans and then tracks the global maximum point within a relatively short time, even under varying weather conditions.

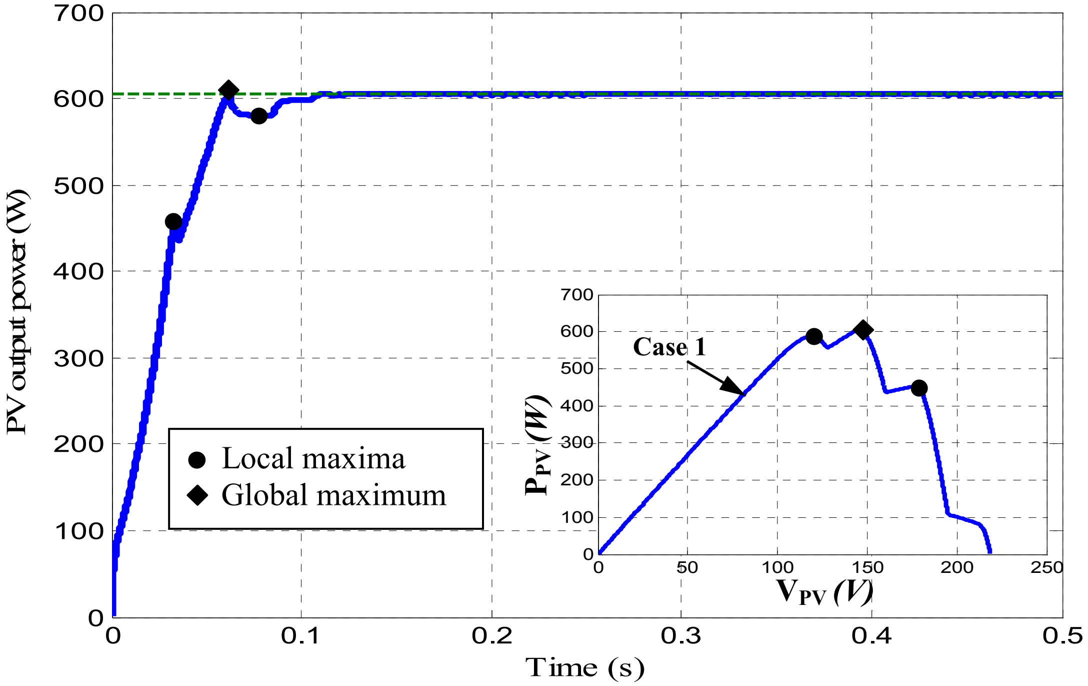

Figure 4.8. PV output power for the proposed MPPT under partially shaded conditions along with the PV power locus.

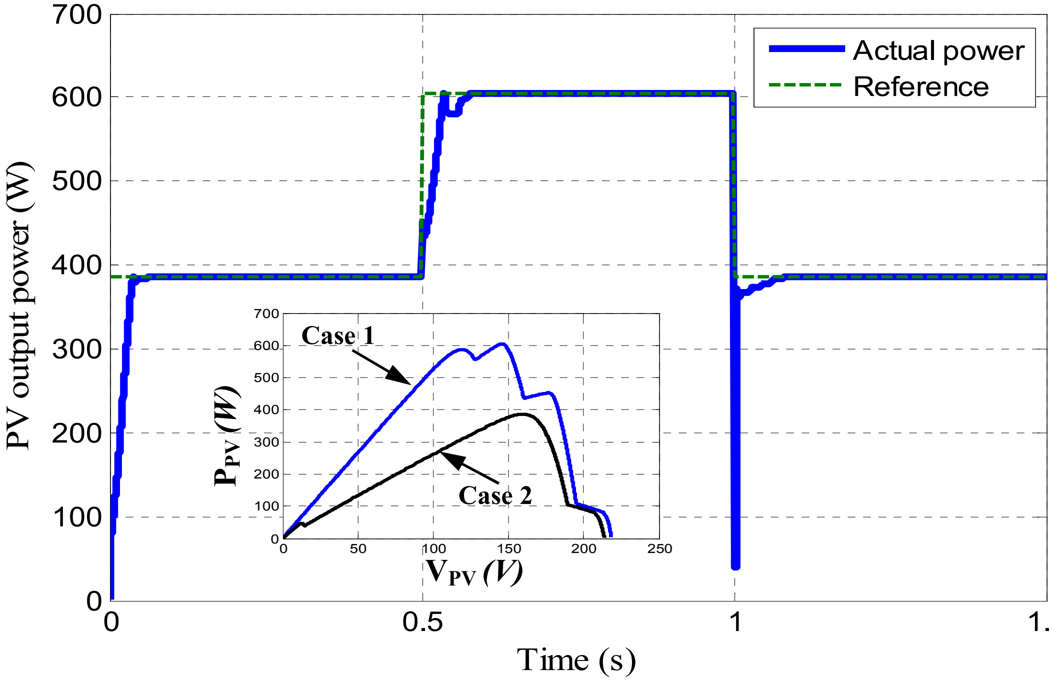

Figure 4.9. Output power for a partially shaded PV system under two radiation levels along with the PV power locus.

To clarify and analyse the behaviour of the proposed MPPT, Figure 4.10 shows the duty cycle of the PV system converter under varying weather conditions of three partially shaded modules. In the initial stage a wide duty cycle range search is applied to scan for the global maximum point. Once the global maximum power is found, the controller stores the value and compares it with the current operation power. If the difference between the stored global maximum power and the current operating power is greater than a preset value, the duty cycle is increased. Also, the fuzzy logic control perturbs and observes the PV system to maintain operation at the optimum duty cycle. During varying weather conditions, the controller resets the stored global maximum value and repeats the same process to find the new global maximum power point.

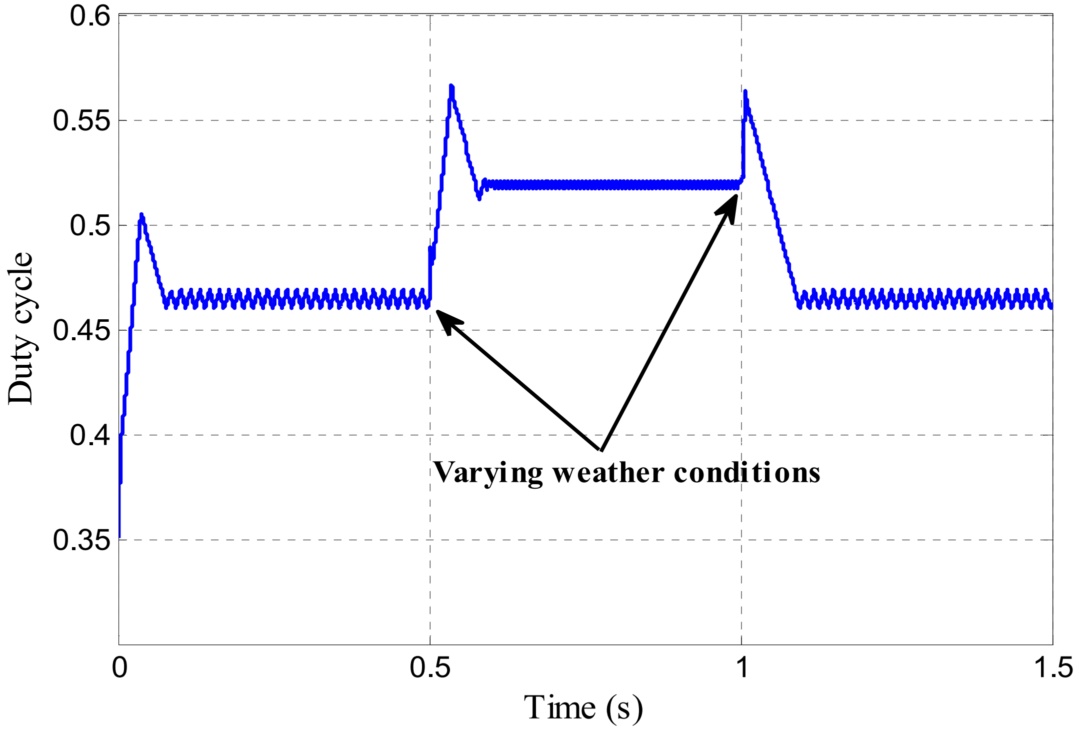

Figure 4.10. Duty cycle behaviour of the proposed MPPT.

4.6 Comparison between the three proposed scanning techniques

As mentioned, three scanning techniques can be used to identify the global maximum power during the initial condition or varying weather conditions:

Technique 1: Initialize the system with a duty cycle close to the maximum allowable duty cycle.

Technique 2: Increase the duty cycle from a minimum to maximum with a fixed step.

Technique 3: Apply a large perturbation step during initial or varying weather conditions.

A comparison between these scanning techniques is assessed for a PV system under different distributed radiation levels; seven unshaded modules receive 1000W/m^2 while the other three modules are partially shaded with radiation levels of 800, 500 and 100W/m^2. As showing in figure 4.11, the global maximum is attained for the three proposed scanning techniques. However, the techniques offer different scanning ranges and speeds. With the first two techniques, the PV power locus is fully scanned to identify the global maximum whilst the third technique scans only a wide range of the PV power locus. Therefore, the third technique is faster with less power loss during initial and varying weather conditions. With each of the three techniques, the duty cycle must return to a minimum value whenever it exceeds the maximum value, to track the global MPP.

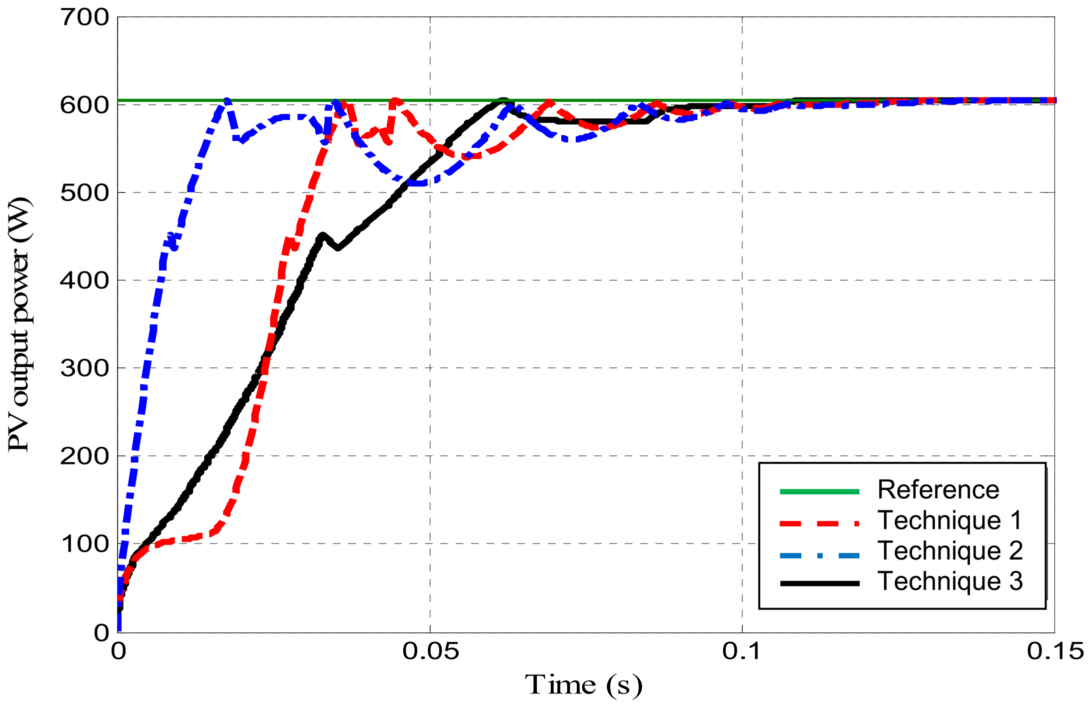

Figure 4.11. PV output power for a partially shaded PV system using the three scanning techniques.

4.7 Experimental results

Experimental verification of the proposed MPPT is achieved with the configuration shown in Figure 4.12. The experimental setup consists of an Agilent modular solar array simulator to generate the PV system *I-V* curves, a boost converter with a 4 kHz switching frequency to boost the output voltage and track the maximum power point, and a battery load to fix the boost converter output voltage and store the PV system energy. An Infineon TriCore TC1796 is used to control the proposed MPPT.

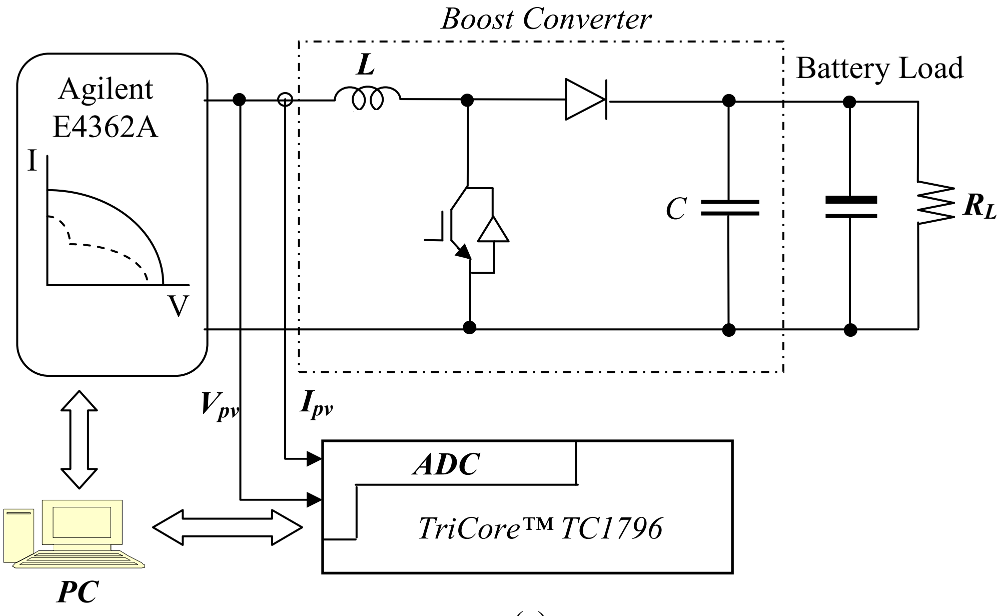

(a)

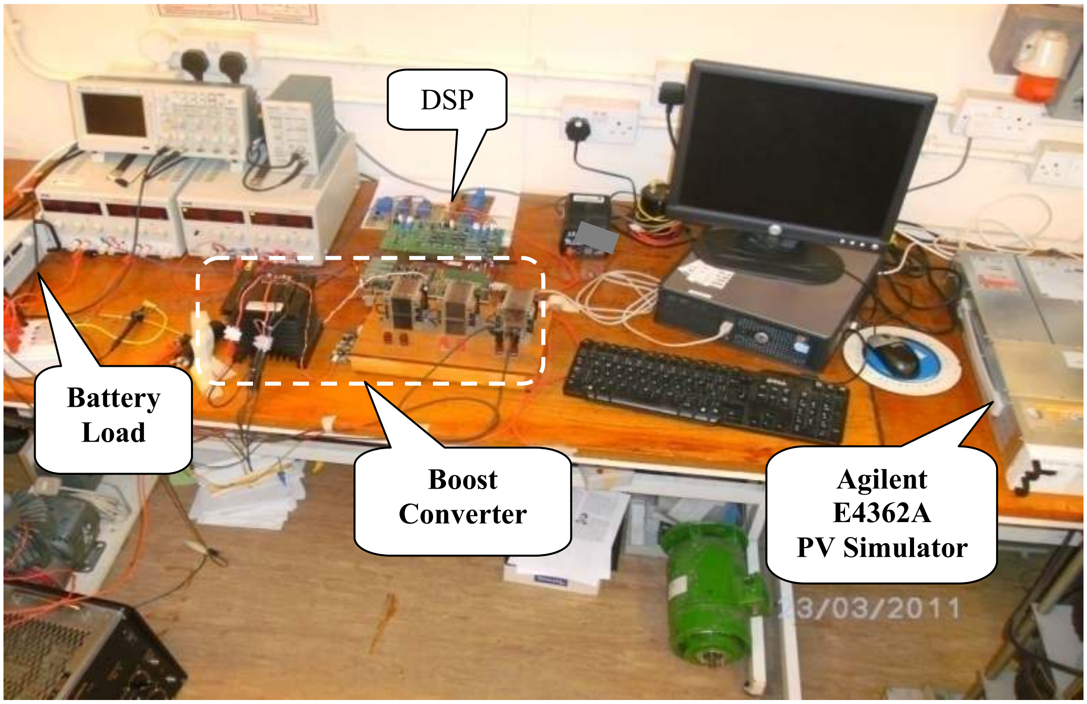

(b)

Figure 4.12. (a) Hardware diagram and (b) test rig photograph.

Different *I-V* curves are programmed into the PV source simulator to test the experimental system under different weather conditions. The results of the proposed MPPT under two uniform insolation conditions are shown in Figure 4.13. The MPP is attained after scanning and tracking the *I-V* curve in a relatively short time compared to hill climbing, with small oscillation in the steady state. When the radiation level varies, the proposed MPPT is reset and repeats the scanning and tracking procedure.

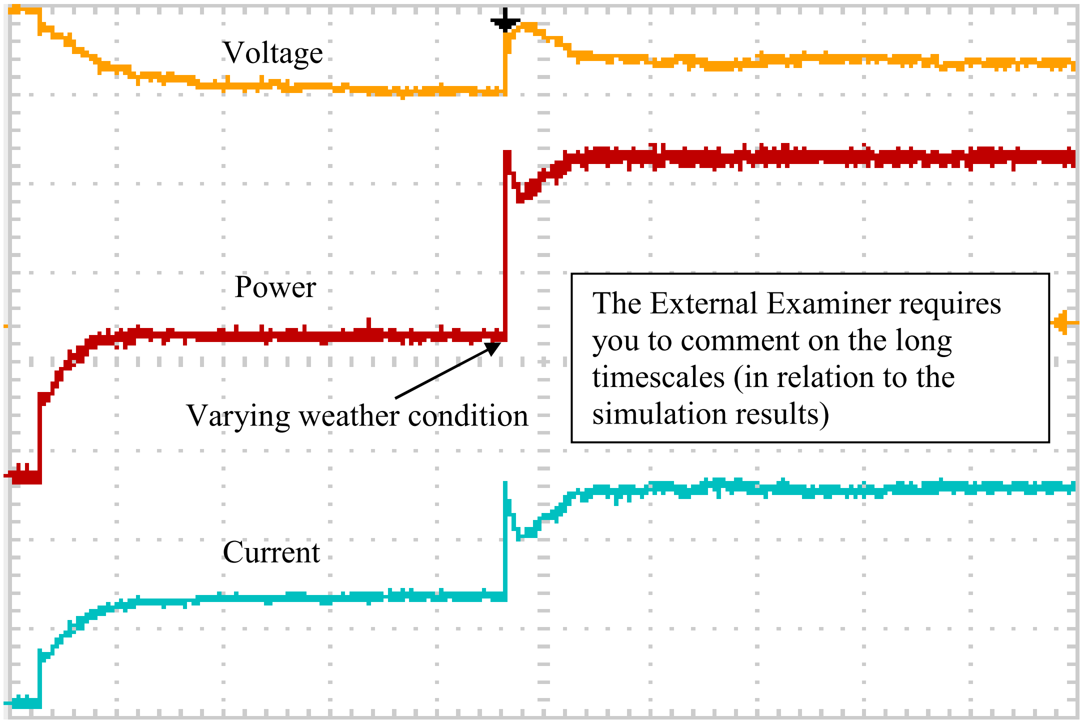

The External Examiner requires you to comment on the long timescales (in relation to the simulation results)

Time: 5s/div, P_o*: 5W/div,* V_o*: 5V/div,* i_o*: 0.5A/div*

Figure 4.13. Experimental results of the proposed MPPT under two radiation levels.

To confirm the effectiveness of the proposed MPPT, equation 4.4 is programmed into the PV source simulator to emulate the PV system characteristic curve under partial shading conditions. As shown in Figure 4.14, the proposed fuzzy based MPPT with a large initial perturbation step (Technique 3) scans and stores the power locus during perturbation and observation. The local maxima in the PV characteristic do not prevent the proposed MPPT from successfully capturing the global MPP in a relatively short time, with small oscillation around the MPP.

Figures 4.11 and 4.12 show differences in convergence times between the simulated and practical results obtained for the proposed technique. This difference may be explained by considering that the simulation models cannot represent accurately all of the switching device nonlinearities and the different delays in the system loops. Simulations do, however, take into account one sample time delay of $250\mu s$ in all measurements to reflect the practical system, and a multi-rate sampling time approach is used to control the computation accuracy of the power circuit using a relatively small time step of the order of $5\mu s$.

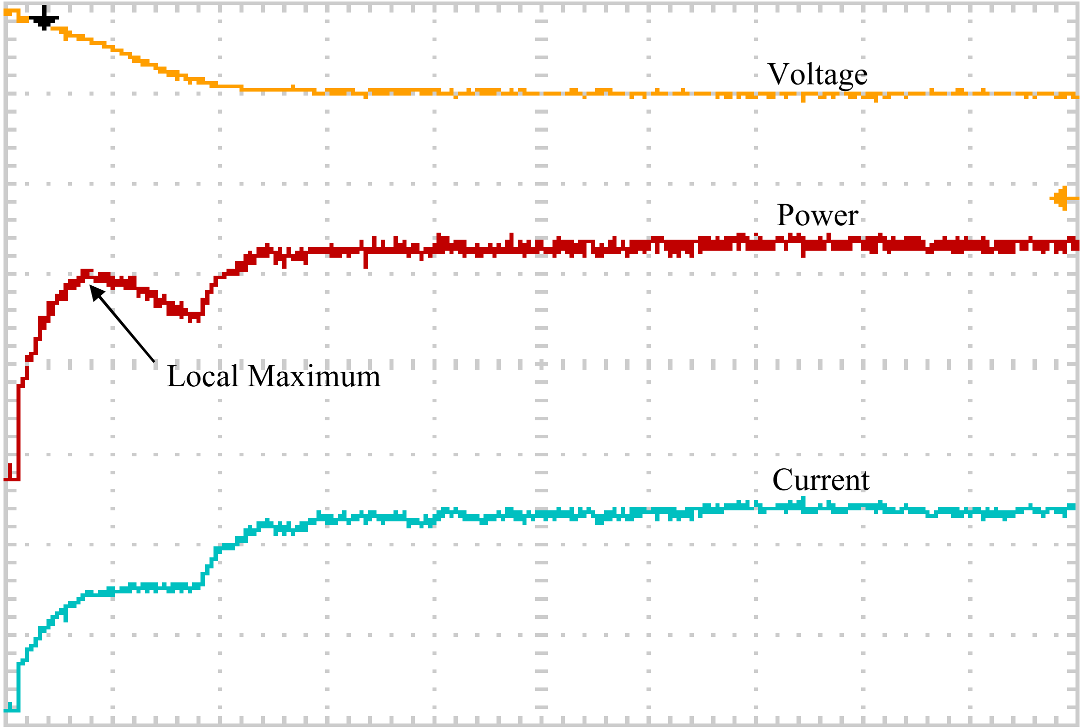

Time: 2.5s/div, P_o*: 5W/div,* V_o*: 10V/div,* i_o*: 0.5A/div*

Figure 4.14. Experimental results of the proposed MPPT under partial shading.

For further verification of the proposed MPPT, a roof-installed PV array on our university building is used to collect data. The PV array system consists of eight PV modules connected in series with the specification, at Standard Test Conditions (STC), as shown in Table 4.3:

Table 4.3. PV module data.

Short circuit current	(*A*)	4.79
Current at MPP	*(A)*	4.36
Open circuit voltage	*(V)*	11
Voltage at MPP	*(V)*	9.2

The PV array system is artificially shaded to generate an *I-V* characteristic with three local MPPs as shown in Figure 4.15a. After programming the *I-V* characteristic into the PV simulator, the proposed MPPT tracks the global MPP by applying a large perturbation step to the system duty cycle to scan and store the global MPP. Once the global maximum is found, fuzzy perturbation and observation takes over to move the operating point to the global MPP, with a small oscillate around it. The power, voltage and current curves of the PV system with the proposed MPPT are shown in Figure 4.15b.

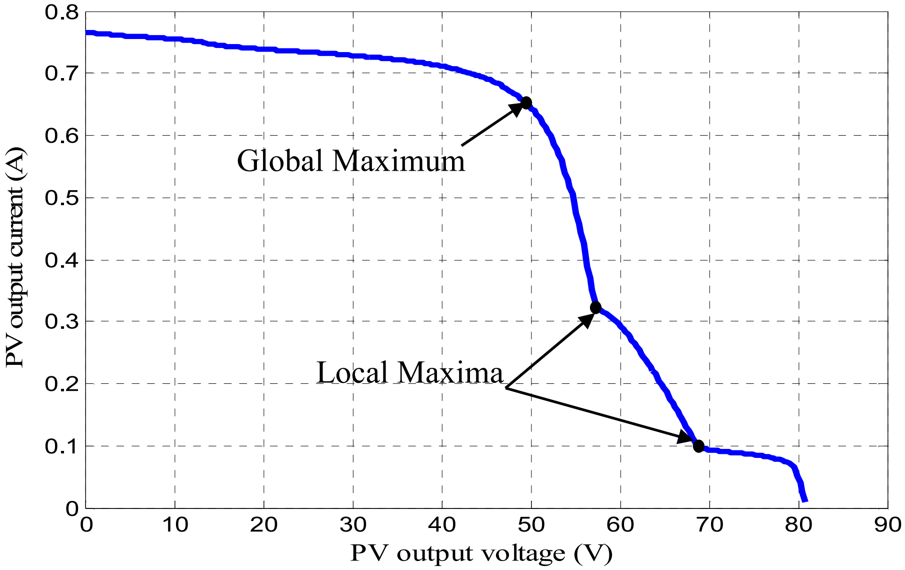

(a)

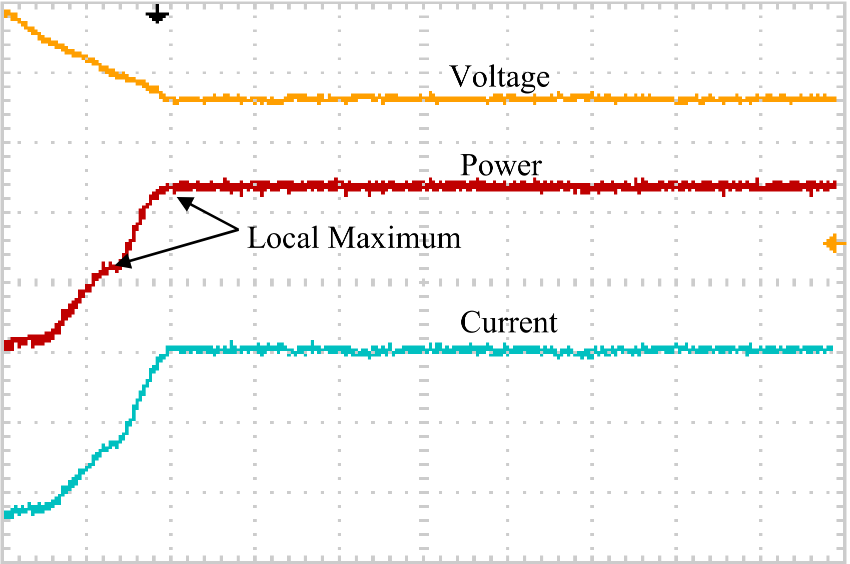

Time: 2.5s/div, P_o: 10W/div, V_o: 5V/div, i_o: 0.5A/div

(b)

Figure 4.15. Experimental results: (a) I-V characteristic curve of a real PV system and (b) the proposed MPPT under real PV conditions.

4.8 Summary

In this Chapter, fuzzy-logic based MPPT has been proposed to extract the global maximum power point under partially shaded PV system conditions. The MPPT was implemented by combining fuzzy-logic based MPPT with a scanning and storing system. Three scanning techniques were proposed to scan the PV power characteristic curve and store the maximum power value, during initial and varying weather conditions. A new mathematical model has been proposed to represent the behaviour of the PV characteristics under partial shading conditions. Matlab/Simulink simulations and practical experiments of a partially shaded PV system validate the proposed MPPT. The results show that the proposed MPPT is able to reach the global maximum power point under any partial shading condition. Moreover, the controller exhibits a fast convergence speed, with small oscillation around the maximum power point during the steady state.

References

[4.1] R. R. a. B. L. Mathur, "A Comprehensive Review and Analysis of Solar Photovoltaic Array Configurations under Partial Shaded Conditions," International Journal of Photoenergy, vol. 2012, 2012.

[4.2] T. Esram and P. L. Chapman, "Comparison of Photovoltaic Array Maximum Power Point Tracking Techniques," Energy Conversion, IEEE Transactions on, vol. 22, pp. 439-449, 2007.

[4.3] A. Safari and S. Mekhilef, "Simulation and Hardware Implementation of Incremental Conductance MPPT With Direct Control Method Using Cuk Converter," Industrial Electronics, IEEE Transactions on, vol. 58, pp. 1154-1161, 2011.

[4.4] L. Fangrui, K. Yong, Z. Yu, and D. Shanxu, "Comparison of P&O and hill climbing MPPT methods for grid-connected PV converter," in Industrial Electronics and Applications, 2008. ICIEA 2008. 3rd IEEE Conference on, 2008, pp. 804-807.

[4.5] J. W. Kimball and P. T. Krein, "Discrete-Time Ripple Correlation Control for Maximum Power Point Tracking," Power Electronics, IEEE Transactions on, vol. 23, pp. 2353-2362, 2008.

[4.6] M. A. G. de Brito, L. Galotto, L. P. Sampaio, G. de Azevedo e Melo, and C. A. Canesin, "Evaluation of the Main MPPT Techniques for Photovoltaic Applications," Industrial Electronics, IEEE Transactions on, vol. 60, pp. 1156-1167, 2013.

[4.7] H. Patel and V. Agarwal, "MATLAB-Based Modeling to Study the Effects of Partial Shading on PV Array Characteristics," Energy Conversion, IEEE Transactions on, vol. 23, pp. 302-310, 2008.

[4.8] G. Petrone, G. Spagnuolo, R. Teodorescu, M. Veerachary, and M. Vitelli, "Reliability Issues in Photovoltaic Power Processing Systems," Industrial Electronics, IEEE Transactions on, vol. 55, pp. 2569-2580, 2008.

[4.9] T. Noguchi, S. Togashi, and R. Nakamoto, "Short-current pulse-based maximum-power-point tracking method for multiple photovoltaic-and-converter module system," Industrial Electronics, IEEE Transactions on, vol. 49, pp. 217-223, 2002.

[4.10] M. A. S. Masoum, H. Dehbonei, and E. F. Fuchs, "Theoretical and experimental analyses of photovoltaic systems with voltageand current-based maximum power-point tracking," Energy Conversion, IEEE Transactions on, vol. 17, pp. 514-522, 2002.

[4.11] S. Kazmi, H. Goto, O. Ichinokura, and G. Hai-Jiao, "An improved and very efficient MPPT controller for PV systems subjected to rapidly varying atmospheric conditions and partial shading," in Power Engineering Conference, 2009. AUPEC 2009. Australasian Universities, 2009, pp. 1-6.

[4.12] H. Patel and V. Agarwal, "Maximum Power Point Tracking Scheme for PV Systems Operating Under Partially Shaded Conditions," Industrial Electronics, IEEE Transactions on, vol. 55, pp. 1689-1698, 2008.

[4.13] Y. LIU, "Advance Control of Photovoltaic Converters," Ph.D. dissertation, Department of Engineering, University of Leicester, Leicester, UK, April 2009.

[4.14] M. Miyatake, T. Inada, I. Hiratsuka, Z. Hongyan, H. Otsuka, and M. Nakano, "Control characteristics of a fibonacci-search-based maximum power point tracker when a photovoltaic array is partially shaded," in Power Electronics and Motion Control Conference, 2004. IPEMC 2004. The 4th International, 2004, pp. 816-821 Vol.2.

[4.15] N. Tat Luat and L. Kay-Soon, "A Global Maximum Power Point Tracking Scheme Employing DIRECT Search Algorithm for Photovoltaic Systems," Industrial Electronics, IEEE Transactions on, vol. 57, pp. 3456-3467, 2010.

[4.16] M. Miyatake, M. Veerachary, F. Toriumi, N. Fujii, and H. Ko, "Maximum Power Point Tracking of Multiple Photovoltaic Arrays: A PSO Approach," Aerospace and Electronic Systems, IEEE Transactions on, vol. 47, pp. 367-380, 2011.

[4.17] K. Ishaque, Z. Salam, M. Amjad, and S. Mekhilef, "An Improved Particle Swarm Optimization (PSO)-Based MPPT for PV With Reduced Steady-State Oscillation," Power Electronics, IEEE Transactions on, vol. 27, pp. 3627-3638, 2012.

[4.18] K. Kobayashi, I. Takano, and Y. Sawada, "A study on a two stage maximum power point tracking control of a photovoltaic system under partially shaded insolation conditions," in Power Engineering Society General Meeting, 2003, IEEE, 2003, p. 2617 Vol. 4.

[4.19] N. Dzung and B. Lehman, "An Adaptive Solar Photovoltaic Array Using Model-Based Reconfiguration Algorithm," Industrial Electronics, IEEE Transactions on, vol. 55, pp. 2644-2654, 2008.

[4.20] G. Velasco-Quesada, F. Guinjoan-Gispert, R. Pique-Lopez, M. Roman-Lumbreras, and A. Conesa-Roca, "Electrical PV Array Reconfiguration Strategy for Energy Extraction Improvement in Grid-Connected PV Systems," Industrial Electronics, IEEE Transactions on, vol. 56, pp. 4319-4331, 2009.

[4.21] H. Obane, K. Okajima, T. Oozeki, and T. Ishii, "PV System With Reconnection to Improve Output Under Nonuniform Illumination," Photovoltaics, IEEE Journal of, vol. 2, pp. 341-347, 2012.

[4.22] Ma, X, A. Ki, and S. Valkealahti, "Power Losses in Long String and Parallel-Connected Short Strings of Series-Connected Silicon-Based Photovoltaic Modules Due to Partial Shading Conditions," Energy Conversion, IEEE Transactions on, vol. 27, pp. 173-183, 2012.

[4.23] S. V. Kartalopoulos and I. N. N. Council, Understanding neural networks and fuzzy logic: basic concepts and applications: Institute of Electrical and Electronics Engineers, 1996.

Chapter 5

Single-Phase Single-Stage Transformerless Grid Connected PV System

A single-phase single-stage current source inverter based photovoltaic system for grid connection is proposed in this chapter. The system utilizes transformerless single-stage conversion for tracking the maximum power point and interfacing a photovoltaic array to the grid. Maximum power point tracking is achieved with the fuzzy logic controller proposed in Chapter 3. A proportional-resonant controller is used to control the current injected into the grid. To improve the power quality and system efficiency, a double tuned parallel resonant circuit is proposed to attenuate the second and fourth order harmonics at the inverter dc side. Additionally, a modified carrier based modulation technique for the current source inverter is proposed to magnetize the dc link inductor by short circuiting one of the bridge converter legs after every active switching cycle. Simulation and practical results of the proposed system validate the dynamic performance and power quality of the proposed system.

5.1 Background

In the grid-connected mode, maximum power is extracted from the PV system to supply maximum available power into the grid. Single and two-stage grid-connected systems are commonly used topologies in single and three-phase PV applications [5.1-3]. In a single-stage grid connected system, the PV system utilizes a single conversion unit (dc/ac power inverter) to track the maximum power point (MPP) and interface the PV system to the grid. In such a topology, PV maximum power is delivered into the grid with high efficiency, small size, and low cost. However, to fulfil grid requirements, such a topology requires either a 50/60Hz voltage step-up transformer, which reduces the system efficiency and increases cost, or a PV array with a high dc voltage. High voltage systems suffer from hotspots during partial shading and increased leakage current between the panel and the system ground though parasitic capacitances [5.4]. Moreover, inverter control is complicated because the control objectives, such as maximum power point tracking (MPPT), power factor correction, and harmonic reduction, are simultaneously considered [5.5]. On the other hand, a two-stage grid-connected PV system utilizes two conversion stages: a dc/dc converter for boosting and conditioning the PV output voltage and tracking the MPP, and a dc/ac inverter for interfacing the PV system to the grid. In such a topology, a high voltage PV array is not essential because of the dc voltage boosting stage. However, this two stage technique suffers from reduced efficiency, higher cost, and larger size [5.6].

From the aforementioned disadvantages of existing grid-connected PV systems, it is apparent that the efficiency and footprint of the two-stage grid-connected system are not attractive [5.7]. Therefore, single-stage inverters have gained attention, especially in low voltage applications. Different single-stage topologies have been proposed, and a comparison of the available interface units is presented in [5.2, 8]. The conventional voltage source inverter (VSI) is the most commonly used interface unit in grid-connected PV system technology due to its simplicity and availability [5.9]. However, the voltage buck properties (voltage step down) of the VSI increases the necessity of using a bulky transformer or higher dc voltage. Moreover, an electrolytic capacitor, which presents a critical point of failure, is also needed [5.4]. Several multilevel inverters have been proposed to improve the ac-side waveform quality, reduce the electrical stress on the power switches, and reduce the power losses due to a high switching frequency [5.10-15]. However, the advantages are achieved at the expense of a more complex PV system. Moreover, a bulky transformer and an electrolytic capacitor are still required.

The current source inverter (CSI) has not been extensively investigated for grid connected renewable energy systems [5.16]. However, it could be a viable alternative technology for PV distributed generation grid connection for the following reasons:

- The dc input current is continuous which is important for PV application.
- System reliability is increased by replacing the shunt input electrolytic capacitor with a series input inductor.
- The CSI voltage boosting capability allows a low-voltage PV array to be grid interfaced without the need of a transformer or an additional boost stage.

Grid-connected PV systems using a current source inverter have been proposed. The three-phase CSI for PV grid connection proposed in [5.17], successfully delivered PV power to the grid, without sensing the ac output current, with a total harmonic distortion (THD) of 4.5%. However, an ac current loop is essential for grid-connected application in order to limit the current and quickly recover the grid current variation during varying weather conditions. A dynamic model and control structure for a single-stage three-phase grid connected PV system using a CSI is proposed in [5.18]. The current injected into the grid has a low THD and unity power factor under various weather conditions. However, the controller consists of only current loops, which affect system reliability.

Unlike the three-phase grid-connected CSI, the single-phase system has even harmonics on the dc side, which affect MPPT, reduce PV lifetime, and are associated with odd order harmonics on the grid side [5.8, 19]. Therefore, eliminating the even harmonics on the dc side is essential in PV applications. Various techniques have been proposed to reduce the even harmonic effects in single phase CSI PV applications. The conventional solution to the dc current oscillation is to use a large inductor, which is capable of eliminating the even-order harmonics. Practically, the CSI inverter produces high dc current [5.18]; therefore, large inductance result in slow response, and is usually bulky and large in size. Thus, this technique is practically unacceptable. To eliminate the harmonics without using large inductance, two solutions have been proposed in the literature, namely feedback current control and hardware techniques. Specially designed feedback current controllers, intended to eliminate the odd harmonics on the ac side without using large inductance, are proposed in literature. In [5.20], the oscillating power effect from the grid is minimized by employing a tuned proportional resonant controller at the third harmonic. Nonlinear pulse width modulation (NPWM) has been proposed in [5.21] to improve harmonic mitigation. NPWM is based on applying computational operations, such as a band-pass filter, a low-pass filter, a phase-shifter block, and various division operations to extract the second-order harmonic component from the dc link current. In [5.22], the power oscillating effect is mitigated by using a modification of the carrier signal on pulse amplitude modulation (PAM). The carrier signal is varied with the second-order harmonic component in the dc link current to eliminate its effect on the grid current. These techniques [5.20-22] are not suitable for a single-stage grid-connected PV system, because the dc current oscillation is large, which causes high system losses and reduces lifetime. In the hardware solution proposed in [5.23], second-order harmonics are eliminated by using an additional parallel resonant circuit on the dc side inductor. Even though the hardware solution adds costs, losses, and size, it is considered to be a practical solution for CSI based PV systems. Usually, the impact of second-order harmonics in the dc side current can significantly affect the ac side current [5.24]. Additionally the fourth-order harmonic in the dc side current could affect the ac side current at high modulation indices.

In this chapter, a single-stage single-phase grid-connected PV system based on a CSI is proposed. A doubled tuned parallel resonant circuit is proposed to eliminate the second and fourth order harmonics on the dc side. Additionally, a modified carrier based modulation technique is proposed to provide a continuous path for the dc side current after each active switching cycle. The control structure consists of fuzzy based MPPT, an ac current loop, and a voltage loop. To demonstrate the effectiveness and robustness of the proposed system, computer-aided simulation and practical results are used to validate the system.

5.2 System description

A grid-connected PV system using a single-phase CSI is shown in Figure 5.1 The inverter has four IGBT's (S1-S4) and four diodes (D1-D4), each diode is connected in series with an IGBT switch for reverse blocking capability. A doubled tuned parallel resonant circuit is in series with dc link inductor L_{dc}, which is employed for smoothing the dc link current. To eliminate the switching harmonics, a C-L filter is connected at the inverter ac side. No grid side transformer is used, meaning that there is no blocking of dc current injection into the grid.

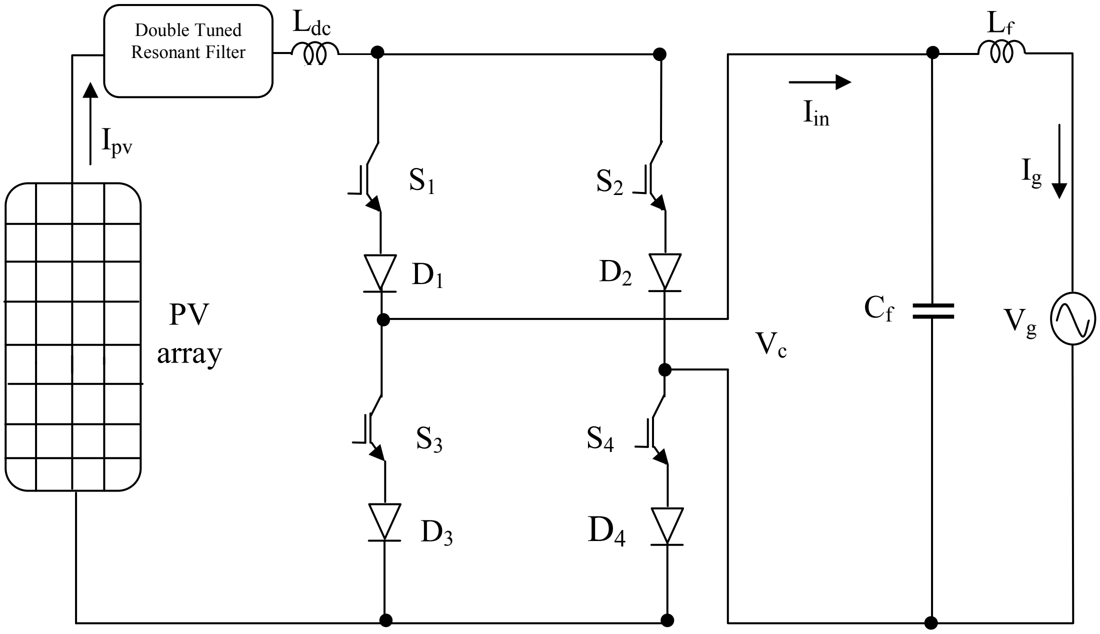

Figure 5.1. Single phase grid connected current source inverter.

5.3 Double tuned Resonant Filter

In a single-phase CSI, the pulsating instantaneous power at twice the system frequency generates even harmonics in the dc link current. These harmonics reflect onto the ac side as low order odd harmonics in the current and voltage. Undesirably, these even harmonics affect MPPT in PV system applications and reduce PV array lifetime [5.8]. In order to mitigate the impact of these dc side harmonics on the ac side and on the PV array, the dc link inductance must be large enough to suppress the dc link current ripple produced by these harmonics. Practically, large dc link inductance is not acceptable, because of its cost, size, weight, and the fact that it slows MPPT transient response. To reduce the necessary dc link inductance, a parallel resonant circuit tuned to the second-order harmonic is employed in series with the dc link inductor. The filter is capable of smoothing the dc link current by using relatively small inductors. Even though the impact of the second-order harmonic is significant in the dc link current, the fourth-order harmonic can also affect the dc link current, especially when the CSI operates at large modulation indices. Therefore, in an attempt to improve the parallel resonant circuit performance, this chapter proposes a double tuned parallel resonant circuit tuned at the second and fourth order harmonics, as shown in Figure 5.2.

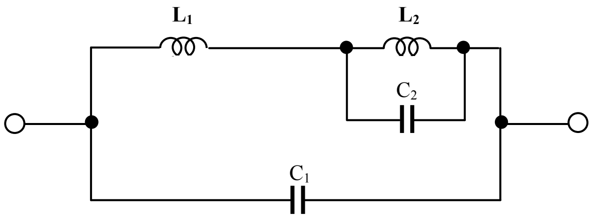

Figure 5.2. The proposed double tuned

In order to tune the resonant filter to the desired harmonic frequencies, the impedance of C_1 and the total impedance of L_1, L_2, and C_2 should have equal values of opposite sign. For simplicity, assume component resistances are small, and thus can be neglected in the calculation.

$$Z_{C1} + Z_t = 0 \tag{5.1}$$

From (5.1), the capacitances are represented by the following equations:

$$C_1 = \frac{L_2 C_2 - \frac{1}{\omega^2}}{\omega^2 L_1 L_2 C_2 - L_1 - L_2} \tag{5.2}$$

$$C_2 = \frac{-L_2}{\frac{L_2}{C_1} - \omega^2 L_1 L_2} + \frac{1}{\omega^2 L_2} \tag{5.3}$$

where C_1 and C_2 are resonant filter capacitances, L_1 and L_2 are the resonant filter inductances, Z_{C1} is C_1 impedance, Z_t is the total impedance of L_1, L_2, and C_2, and ω is the angular frequency of the second and fourth orders harmonics in 5.2 and 5.3 respectively. After selecting the inductance values, which are capable of allowing the maximum *di/dt* at rated current, the angular frequency of the second harmonic in (5.2) and the angular frequency of the fourth harmonic in (5.3) are used. The desired capacitances are calculated by numerically solving (5.2) and (5.3). Figure 5.3 shows the impedance versus frequency measurement for the doubled tuned parallel resonant circuit. The filter is capable of eliminating both the second and fourth order harmonics.

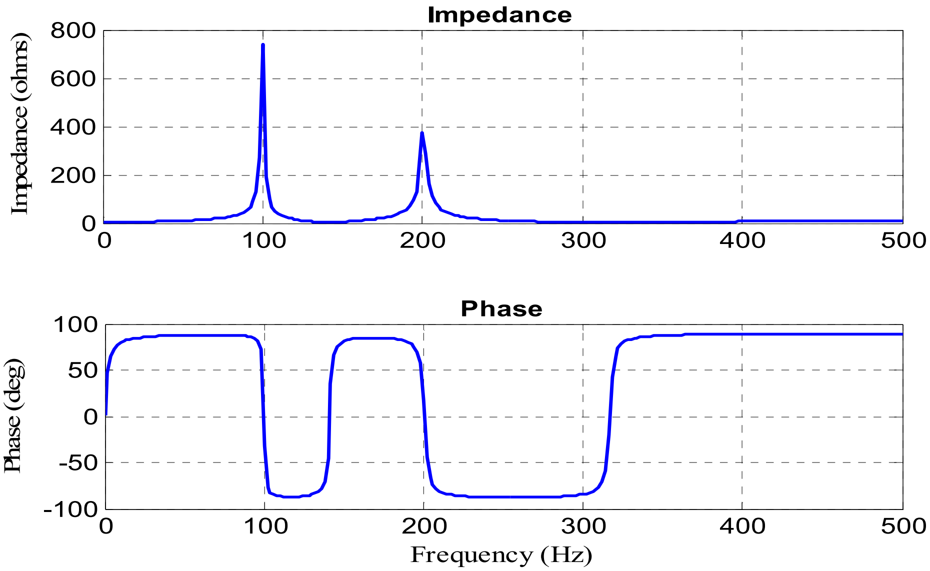

Figure 5.3. Impedance versus frequency measurement
for the doubled tuned parallel resonant circuit.

In order to obtain the relationship between the resonant inductances (L_1 and L_2), (5.1) and (5.2) are solved for C_1:

$$C_1 = \frac{\sqrt{L_1(L_1\omega_1^4 + L_1\omega_2^4 - 2L_1\omega_1^2\omega_2^2 - 4L_2\omega_1^2\omega_2^2)} + L_1\omega_1^2 + L_1\omega_2^2}{2L_1^2\omega_1^2\omega_2^2 + 2L_1L_2\omega_1^2\omega_2^2} \tag{5.4}$$

From (5.4), to avoid complex numbers in the solution, the relationship between L_1 and L_2 should be:

$$L_2 \le 1.778L_1 \tag{5.5}$$

To select the optimum values for the proposed filter components, the effects of varying resonant circuit inductance are analyzed. Figure 5.4 shows resonant capacitance (C_1 and C_2) as a function of the resonant inductances L_1 and L_2. It can be shown that C_1 is not significantly affected when varying L_1 and L_2, whereas C_2 is affected mainly by L_2 . As L_2 decreases the value of C_2 increases. Therefore, increasing the capacitance leads to reduced overall system weight and size by reducing the dc link inductance.

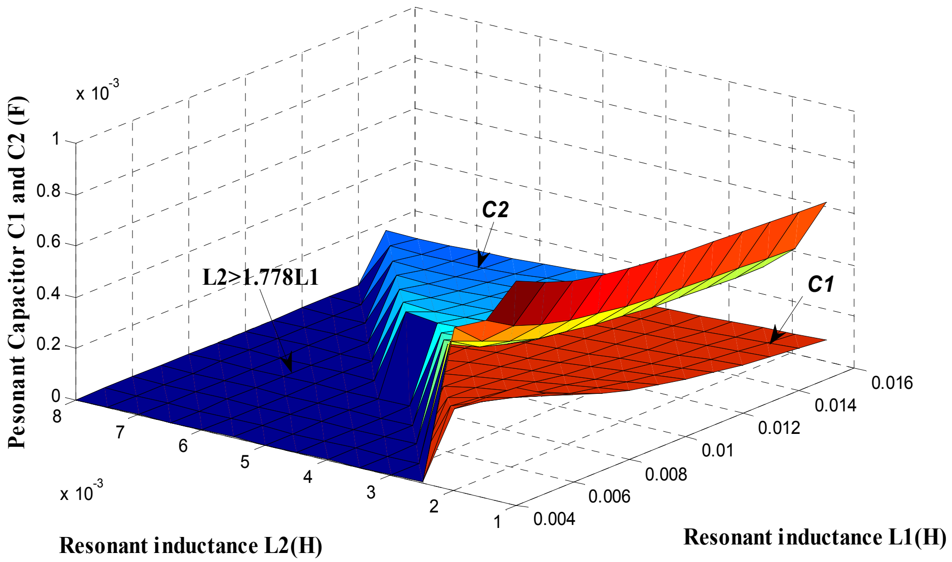

Figure 5.4. Characteristics of the double tuned resonant filter: the resonant capacitances (*C1* and *C2*) as a function of the resonant inductance (*L1*) and the resonant inductance (*L2*).

The proposed filter concept can be extended to eliminate any number of harmonics by employing the cascaded circuit shown in Figure 5.5. In order to compute the filter passive components, (5.6) is numerically solved for C_1 to C_n.

$$\begin{aligned} &L_1\omega_1 + \frac{1}{\omega_1 C_1} + Z_t = 0 \\ &L_1\omega_2 + \frac{1}{\omega_2 C_1} + Z_t = 0 \\ &\vdots \\ &L_1\omega_n + \frac{1}{\omega_n C_1} + Z_t = 0 \end{aligned} \tag{5.6}$$

where Z_t is the total impedance of the series-parallel circuit components L_2 to L_n and C_2 to C_n, and n is the harmonic order. To clarify the proposed filter design for the mitigation of more harmonics, an example of eliminating three harmonics is outlined. To eliminate the second, fourth and sixth order harmonics, (5.6) is rewritten as:

$$C_1 = \frac{-(C_2L_2\omega_2^2 + C_2L_3\omega_2^2 + C_3L_3\omega_2^2 - C_2C_3L_2L_3\omega_2^4 - 1)}{L_1\omega_2^2 + L_2\omega_2^2 + L_3\omega_2^2 - C_2L_1L_2\omega_2^4 - C_2L_1L_3\omega_2^4 - C_3L_1L_3\omega_2^4 - C_3L_2L_3\omega_2^4 + C_2C_3L_1L_2L_3\omega_2^6} \tag{5.7}$$

$$C_2 = \frac{-(C_1L_1\omega_4^2 + C_1L_2\omega_4^2 + C_1L_3\omega_4^2 + C_3L_3\omega_4^2 - C_1C_3L_1L_3\omega_4^4 - C_1C_3L_2L_3\omega_4^4 - 1)}{L_2\omega_4^2 + L_3\omega_4^2 - C_1L_1L_2\omega_4^4 - C_1L_1L_3\omega_4^4 - C_3L_2L_3\omega_4^4 + C_1C_3L_1L_2L_3\omega_4^6} \tag{5.8}$$

$$C_3 = \frac{C_1L_1\omega_6^2 + C_1L_2\omega_6^2 + C_1L_3\omega_6^2 + C_2L_2\omega_6^2 + C_2L_3\omega_6^2 - C_1C_2L_1L_2\omega_6^4 - C_1C_2L_1L_3\omega_6^4 - 1}{C_1L_1L_3\omega_6^4 - L_3\omega_6^2 + C_1L_2L_3\omega_6^4 + C_2L_2L_3\omega_6^4 - C_1C_2L_1L_2L_3\omega_6^6} \tag{5.9}$$

By numerically solving (5.7), (5.8) and (5.9), the capacitances that eliminate the desired harmonics can be computed.

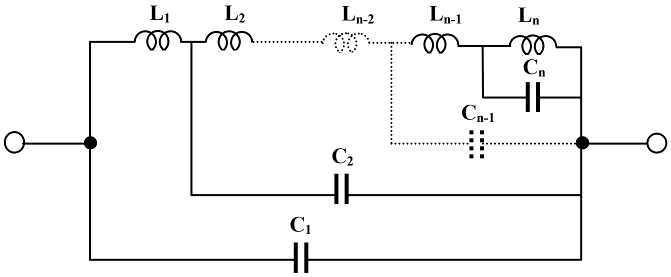

Figure 5.5. The proposed double tuned resonant filter for eliminating *n* harmonics.

5.4 Modified carrier based pulse width modulation

Modified carrier based pulse width modulation (CPWM) is proposed to control the switching pattern for the single-phase grid connected CSI. In order to provide a continuous path for the dc side current, at least one top switch in either arm and one bottom switch must be turned on during every switching period. In conventional sinusoidal pulse width modulation (SPWM), the existence of overlap time as the power devices change switching states allows a continuous path for the dc current. However the overlap time is insufficient to energise the dc link inductor, which results in increased THD. Therefore, CPWM is proposed to provide sufficient short circuit current after every active switching action. CPWM consists of two carriers and one reference. Figure 5.6 shows the reference and carrier waveforms along with the switching patterns. The carrier with a solid straight line shown in Figure 5.6 is responsible for the upper switches while the dashed line carrier is responsible for the lower switches, and is shifted by 180°. To understand the switching patterns of the proposed CPWM, Figure 5.6 is divided into ten regions (t_1-t_{10}) where each region represents one carrier frequency period. Table 1 shows the switch combinations for the ten regions. From Figure 5.6 and Table 1, CPWM operates in two modes, a conductive mode and a null mode and the switching action for each IGBT is equally distributed during each fundamental period. To validate the proposed CPWM, simulation results of a CSI operated with both CPWM and SPWM are shown in Figure 5.7. The CSI is operated in an island-mode and has the following specification:

> The dc voltage V_{dc} is 50V. In the double tuned resonant filter $L_1 = 10mH$, $L_2 = 5mH$, $C_1 = 125\ \mu F$ and $C_2 = 250\ \mu F$, the capacitor on the ac side is 20 μF, the inductance is 1 mH, resistive load is 50 Ω, output voltage is 110V and the switching frequency is 4 kHz.

Figure 5.7 shows that the proposed CPWM generates lower switching frequency harmonics in the ac output current, when compared with conventional SPWM. The THD is 1% with the proposed CPWM and 4.4% with conventional SPWM.

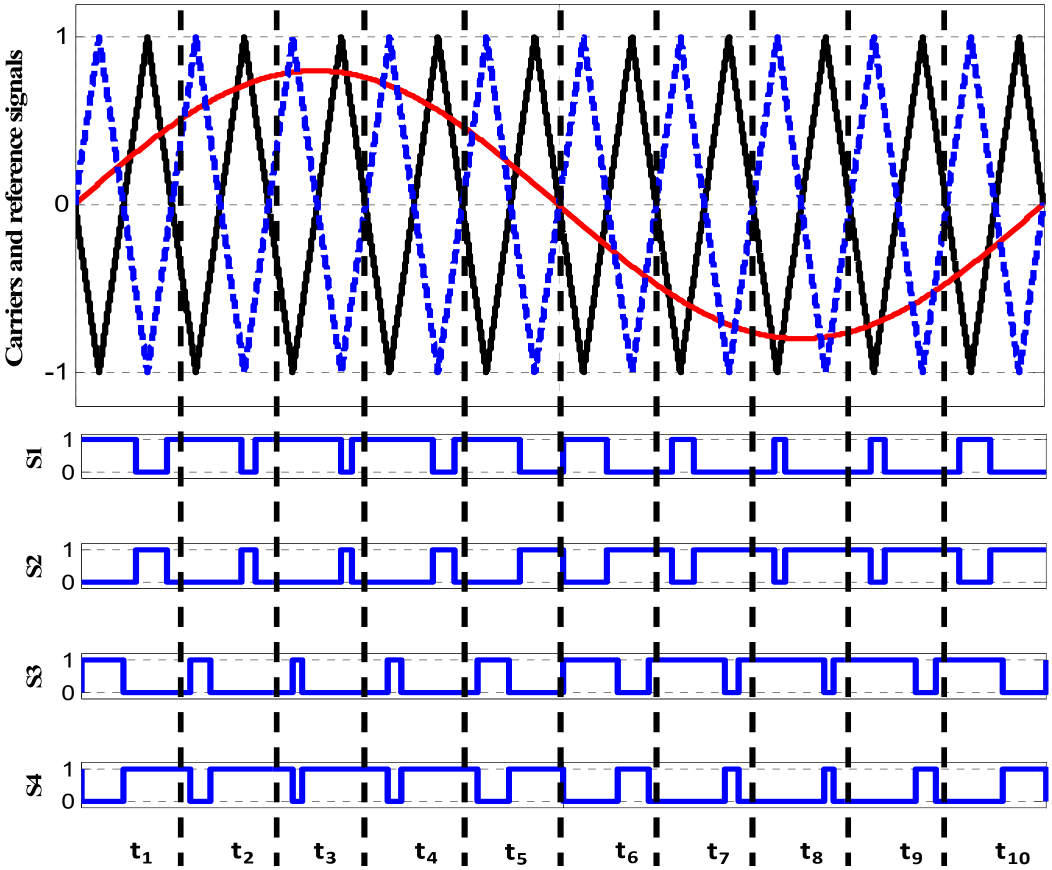

Figure 5.6. Proposed carriers based PWM along with switching sequence for one fundamental frequency.

Table 5.1. Switching combination sequence.

Region	combination sequence
t_1	(S_1-S_3) (S_1-S_4) (S_2-S_4) (S_1-S_4)
t_2	(S_1-S_3) (S_1-S_4) (S_2-S_4) (S_1-S_4)
t_3	(S_1-S_3) (S_1-S_4) (S_2-S_4) (S_1-S_4)
t_4	(S_1-S_3) (S_1-S_4) (S_2-S_4) (S_1-S_4)
t_5	(S_1-S_3) (S_1-S_4) (S_2-S_4)
t_6	(S_1-S_3) (S_2-S_3) (S_2-S_4) (S_2-S_3)
t_7	(S_1-S_3) (S_2-S_3) (S_2-S_4) (S_2-S_3)
t_8	(S_1-S_3) (S_2-S_3) (S_2-S_4) (S_2-S_3)
t_9	(S_1-S_3) (S_2-S_3) (S_2-S_4) (S_2-S_3)
t_{10}	(S_1-S_3) (S_2-S_3) (S_2-S_4)

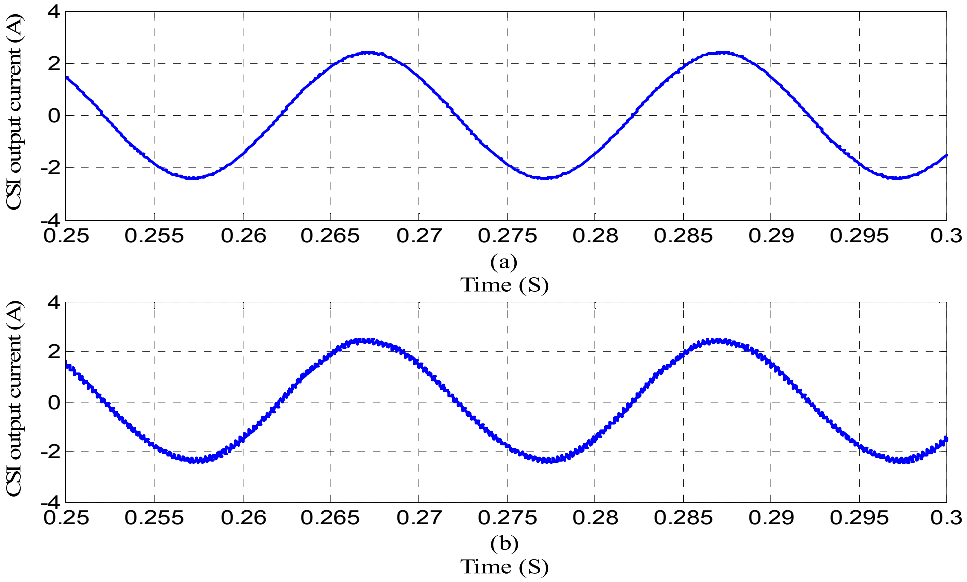

Figure 5.7. Comparison between the proposed CPWM and conventional SPWM; (a) CSI output current using CPWM and (b) CSI output current using SPWM.

5.5 Proposed system control technique

To design a grid-connected PV system using a CSI, the relationship between the PV output voltage and the grid voltage is derived as follows:

By neglecting inverter losses, the PV output power is equal to the grid power

$$V_{PV} I_{PV} = \tfrac{1}{2} I_{g,peak} V_{g,peak} \cos\theta \tag{5.10}$$

where θ is the phase angle, V_{pv} and I_{pv} are the PV output voltage and current, while $V_{g,peak}$ and $I_{g,peak}$ are the grid peak voltage and current, both respectively. The grid current is equal to the PV output current multiplied by the inverter modulation index M.

$$I_{g,peak} = M I_{PV} \tag{5.11}$$

Substituting (5.11) into (5.10), assuming unity power factor, the equation describing the relationship between the PV output voltage and the grid voltage is:

$$V_{PV} = \tfrac{1}{2} M V_{g,peak} \tag{5.12}$$

Therefore, in order to interface the PV system to the grid using a CSI, the PV voltage should not exceed half the grid peak voltage.

The CSI is utilized to track the PV maximum power point and to interface the PV system to the grid. In order to achieve these requirements, three control loops are employed, namely MPPT, an ac current loop, and a voltage loop.

To operate the PV at the MPP, MPPT is used to identify the optimum grid current peak value. Any conventional MPPT technique can be used. However, to prevent significant losses in power, the tracking technique should be fast enough to cater for any variation in load or weather conditions. Therefore, a fuzzy logic controller (FLC) is used to quickly locate the MPP.

The inputs of the FLC are:

$$\Delta P = P(k) - P(k-1) \tag{5.13}$$

$$\Delta I_{PV} = I_{PV}(k) - I_{PV}(k-1) \tag{5.14}$$

and the output equation is:

$$\Delta I_{g,ref} = I_{g,ref}(k) - I_{g,ref}(k-1) \tag{5.15}$$

where ΔP and ΔI_{PV} are the PV array output power and current change, $\Delta I_{g,ref}$ is the grid current amplitude change reference, $I_{g,ref}$ is the grid current reference, and k is the sample instant. The variable inputs and output are divided into four fuzzy subsets: PB (*Positive Big*), PS (*Positive Small*), NB (*Negative Big*), and NS (*Negative Small*). Therefore, the fuzzy algorithm requires 16 fuzzy control rules; these rules are based on the regulation of the hill climbing algorithm, where the fuzzy rules are shown in Table 5.2. To operate the fuzzy combination, Mamdani's method with Max-Min is used [5.25].

From the behaviour of the controller inputs and output, the shapes and fuzzy subset partitions of the membership function in both the inputs and output are shown in Figure 5.8. A centre of area algorithm (COA) is used in the defuzzification stage to convert the fuzzy subset duty cycle changes into real numbers.

$$\Delta I_{g,ref} = \frac{\sum_{i}^{n} \mu(I_{g,ref,i}) I_{g,ref,i}}{\sum_{i}^{n} \mu(I_{g,ref,i})} \tag{5.16}$$

where $\Delta I_{g,ref}$ is the fuzzy controller output and $I_{g,ref,i}$ is the centre of Max-Min composition at the output membership function.

To ensure synchronization between the grid current and voltage, a sinusoidal signal generated from a phase-locked-loop (PLL) is multiplied by the MPPT output. Figure 5.9 shows a block diagram of the MPPT structure.

Table 5.2. Fuzzy logic rules.

ΔP \ ΔI	**NB**	**NS**	**PS**	**PB**
NB	PB	PB	NB	NB
NS	PS	PS	NS	NS
PS	NS	NS	PS	PS
PB	NB	NB	PB	PB

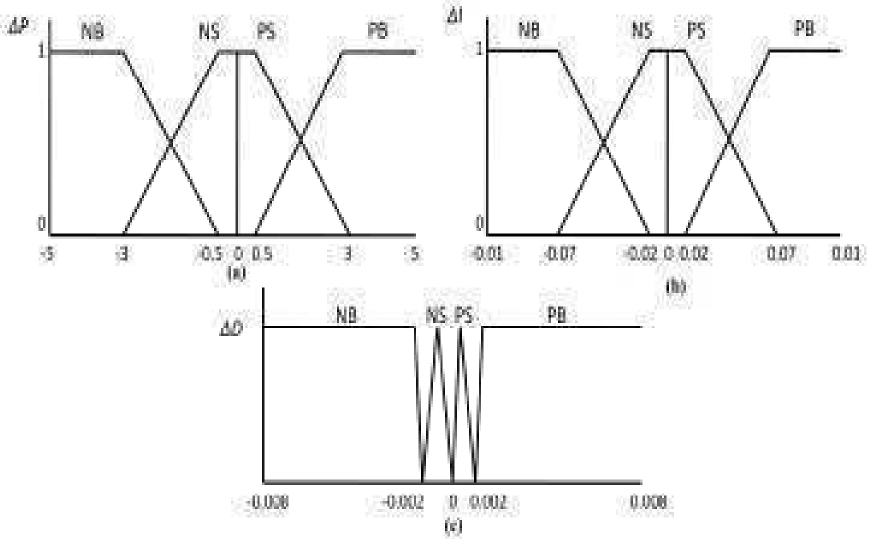

Figure 5.8. Membership function:
(a) input Δ*P* and (b) input Δ*I* and (c) output Δ*D*.

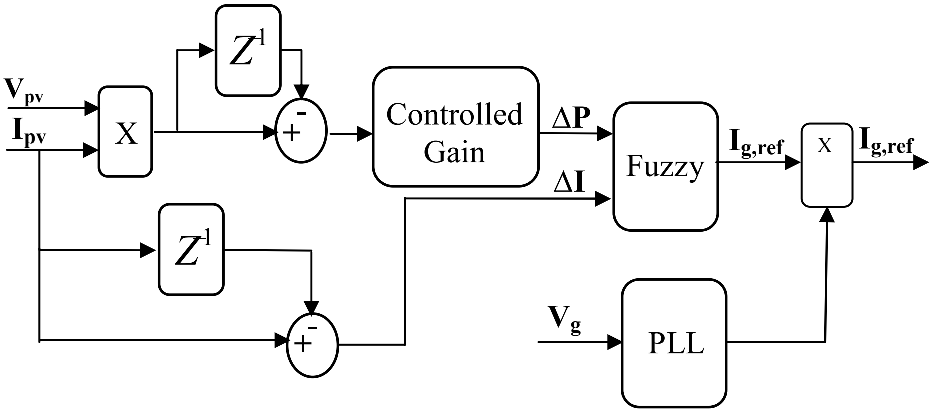

Figure 5.9. Block diagram of the FLC based MPPT.

For precise control of the single-phase inverter, proportional-resonant (PR) control is employed in the voltage and current loop controllers. The basic function of the PR controller is to introduce an infinite gain at a selected resonant frequency in order to eliminate steady-state error at that frequency. The (PR) controller transfer function is expressed as:

$$y = K_p e + K_i \frac{es}{s^2 + \omega_o^2} \tag{5.17}$$

where K_p is the proportional gain, K_i is the integral gain, e is the signal error, and ω_o is the fundamental angular frequency.

The transfer function of the PR controller is digitized using the following derivation:

Let

$$Z = K_i \frac{es}{s^2 + \omega_o^2} \tag{5.18}$$

Rearrange (5.18) as:

$$sZ + \frac{\omega_o^2}{s} Z = K_i e \tag{5.19}$$

Let

$$W = \frac{\omega_o^2 Z}{s} \tag{5.20}$$

By taking the derivative of (5.19) and (5.20):

$$\frac{dW}{dt} = \omega_o^2 Z \tag{5.21}$$

$$\frac{dZ}{dt} = K_i e - W \tag{5.22}$$

where Z and W are auxiliary control variables used to facilitate the control design. In the following section, the subscripts i and v are used with these control variables to signify the current and voltage controllers respectively.

From (5.17), (5.21), and (5.22), the output of the PR controller can be rewritten as:

$$y = k_p e + \int ((k_i e) - \int \omega_o^2 Z dt) dt \tag{5.23}$$

In order to compute the controller output equations 5.21, 5.22 and 5.23 are solved numerically as:

$$W^{k+1} = W^k + T_s \omega_o^2 Z^k \tag{5.24}$$

$$Z^{k+1} = Z^k + T_s (K_i e - W^{k+1}) \tag{5.25}$$

$$y = K_p e + Z^{k+1} \tag{5.26}$$

The ac current and voltage loops are designed from the equivalent circuit of the CSI ac side, which is shown in Figure 5.10, and the PR controller equations.

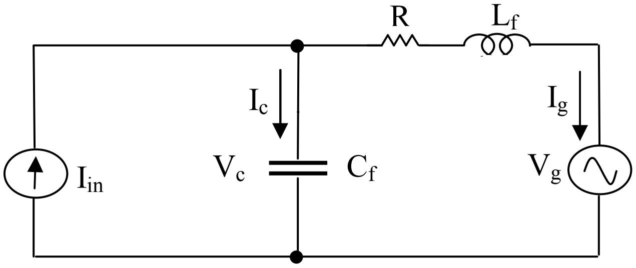

Figure 5.10. Equivalent circuit of the CSI ac side.

where I_{in} is the CSI output current, C_f is the filter capacitance, L_f is the filter inductance, R is the inductor internal resistance, I_c is the current passing through the capacitor, I_g is the grid current and V_g is the grid voltage.

The differential equation describing the ac side dynamic voltage is:

$$\frac{dI_g}{dt} = -\frac{R}{L_f} I_g + \frac{V_c - V_g}{L_f} \tag{5.27}$$

Let

$$u = V_c - V_g \tag{5.28}$$

From (5.27) and (5.28), by feeding the grid current error to the PR controller, the value of u is obtained from (5.23):

$$u = k_{pi}(I_{g,ref} - I_g) + \int (k_{ii}(I_{g,ref} - I_g) - \int \omega_o^2 Z_i dt)dt \tag{5.29}$$

Substituting equation 5.29 into 5.27

$$\frac{di_g}{dt} = \frac{k_{pi} I_{g,ref}}{L_f} - \frac{k_{pi} I_g}{L_f} - \frac{RI_g}{L_f} + \frac{Z_i}{L_f}$$

(5.30)

where

$$Z_i = \int (k_{ii}(I_{g,ref} - I_g) - W_i)dt \tag{5.31}$$

and

$$W_i = \int \omega_o^2 Z_i dt \tag{5.32}$$

where k_{pi} is the current controller proportional gain and k_{ii} is the current controller integral gain.

By taking the derivatives of (5.31) and (5.32):

$$\frac{dZ_i}{dt} = k_{ii}(I_{g,ref} - I_g) - W_i \tag{5.33}$$

$$\frac{dW_i}{dt} = \omega_o^2 Z_i \tag{5.34}$$

From (5.30), (5.33), and (5.34), the state space model of the current loop controller is:

$$\frac{d}{dt}\begin{pmatrix} I_g \\ Z_i \\ W_i \end{pmatrix} = \begin{pmatrix} \frac{-(R+K_{pi})}{L_f} & \frac{1}{L_f} & 0 \\ -K_{ii} & 0 & -1 \\ 0 & \omega_o^2 & 0 \end{pmatrix} \begin{pmatrix} I_g \\ Z_i \\ W_i \end{pmatrix} + \begin{pmatrix} \frac{K_{pi}}{L_f} \\ K_{ii} \\ 0 \end{pmatrix} I_{g,ref} \tag{5.35}$$

Similarly, the differential equation that describes the ac side dynamic current is:

$$\frac{dV_c}{dt} = \frac{I_{in} - I_g}{C_f} \tag{5.36}$$

let

$$\lambda = I_{in} - I_g \tag{5.37}$$

From equations 5.36 and 5.37, by feeding the grid current error into the PR controller, the value of *u* is obtained from equation 5.23:

$$\lambda = k_{pv}(V_{c,ref} - V_c) + \int (k_{iv}(V_{c,ref} - V_c) - \int \omega_o^2 Z_v dt) dt \tag{5.38}$$

Substituting equation 5.38 into 5.36

$$\frac{dV_c}{dt} = \frac{k_{pv}V_{c,ref}}{C_f} - \frac{k_{pv}V_c}{C_f} + \frac{Z_v}{C_f} \tag{5.39}$$

where

$$Z_v = \int (k_{iv}(V_{c,ref} - V_{cg}) - W_v) dt \tag{5.40}$$

and

$$W_v = \int \omega_o^2 Z_v dt \tag{5.41}$$

where k_{pv} is the voltage controller proportional gain and k_{iv} is the voltage controller integral gain.

By taking the derivatives of (5.40) and (5.41):

$$\frac{dZ_v}{dt} = k_{iv}(V_{c,ref} - V_c) - W_v \tag{5.42}$$

$$\frac{dW_v}{dt} = \omega_o^2 Z_v \tag{5.43}$$

From equations 5.39, 5.42, and 5.43, the state space model of the voltage loop controller is:

$$\frac{d}{dt}\begin{pmatrix} V_c \\ Z_v \\ W_v \end{pmatrix} = \begin{pmatrix} \frac{-K_{pv}}{C_f} & \frac{1}{C_f} & 0 \\ -K_{iv} & 0 & -1 \\ 0 & \omega_o^2 & 0 \end{pmatrix} \begin{pmatrix} V_c \\ Z_v \\ W_v \end{pmatrix} + \begin{pmatrix} \frac{K_{pv}}{C_f} \\ K_{iv} \\ 0 \end{pmatrix} V_{c,ref} \tag{5.44}$$

To obtain the overall state-space model of the controllers, equation 5.28 is rewritten as:

$$V_c, ref = u + V_g = k_{pi}(I_{g,ref} - I_g) + Z_i + V_g \tag{5.45}$$

By substituting equation 5.45 into equation 5.39:

$$\frac{dV_c}{dt} = -\frac{k_{pv}V_c}{C_f} + \frac{Z_v}{C_f} - \frac{k_{pv}K_{ii}I_{gc}}{C_f} + \frac{Z_i}{C_f} + \frac{k_{pv}K_{ii}I_{g,ref}}{C_f} + \frac{k_{pv}V_g}{C_f} \tag{5.46}$$

$$\frac{dZ_v}{dt} = -k_{iv}V_c - k_{iv}k_{pi}I_g + k_{iv}k_{pi}I_{g,ref} + k_{iv}Z_i + k_{iv}V_g - W_v \tag{5.47}$$

$$\frac{dW_v}{dt} = \omega_o^2 Z_v \tag{5.48}$$

From equations 5.30, 5.33, 5.34, 5.46, 5.47, and 5.48, the system state space model is:

$$\frac{d}{dt}\begin{pmatrix} V_c \\ Z_v \\ W_v \\ I_g \\ Z_i \\ W_i \end{pmatrix} = \begin{pmatrix} \frac{-k_{pv}}{C_f} & \frac{1}{C_f} & 0 & \frac{k_{pv}k_{pi}}{C_f} & \frac{k_{pv}}{C_f} & 0 \\ -k_{iv} & 0 & -1 & k_{iv}k_{pi} & k_{iv} & 0 \\ 0 & \omega_o^2 & 0 & 0 & 0 & 0 \\ 0 & 0 & 0 & \frac{-k_{pi}}{L_f} & \frac{1}{L_f} & 0 \\ 0 & 0 & 0 & -k_{ii} & 0 & -1 \\ 0 & 0 & 0 & 0 & \omega_o^2 & 0 \end{pmatrix} \begin{pmatrix} V_c \\ Z_v \\ W_v \\ I_g \\ Z_i \\ W_i \end{pmatrix} + \begin{pmatrix} \frac{k_{pv}k_{pi}}{C_f} & \frac{k_{pv}}{C_f} \\ k_{iv}k_{pi} & k_{iv} \\ 0 & 0 \\ \frac{k_{pi}}{L_f} & 0 \\ k_{ii} & 0 \\ 0 & 0 \end{pmatrix} \begin{pmatrix} I_{g,ref} \\ V_g \end{pmatrix} \tag{5.49}$$

Eq. (5.49) can be rewritten in short form as:

$$\frac{dx(t)}{dt} = Ax(t) + Bu(t) \tag{5.50}$$

Using the first-order Euler approximation, equation (5.50) can be written in discrete form as:

$$x(k+1) = (1+T_s A)x(k) + T_s Bu(k) \tag{5.51}$$

Therefore equation (49) can be expressed in discrete form as:

$$\begin{bmatrix} V_c(k+1) \\ Z_v(k+1) \\ W_v(k+1) \\ I_g(k+1) \\ Z_i(k+1) \\ W_i(k+1) \end{bmatrix} = \begin{bmatrix} 1-T_s\dfrac{k_{pv}}{C_f} & T_s\dfrac{1}{C_f} & 0 & T_s\dfrac{k_{pv}k_{pi}}{C_f} & T_s\dfrac{k_{pv}}{C_f} & 0 \\ -T_s k_{iv} & 1 & -T_s & T_s k_{iv} k_{pi} & T_s k_{iv} & 0 \\ 0 & \omega_0^2 T_s & 1 & 0 & 0 & 0 \\ 0 & 0 & 0 & 1-T_s\dfrac{k_{pi}}{L_f} & T_s\dfrac{1}{L_f} & 0 \\ 0 & 0 & 0 & T_s k_{ii} & 1 & -T_s \\ 0 & 0 & 0 & 0 & \omega_0^2 T & 1 \end{bmatrix} \begin{bmatrix} V_c(k) \\ Z_v(k) \\ W_v(k) \\ I_g(k) \\ Z_i(k) \\ W_i(k) \end{bmatrix} + \begin{bmatrix} T_s\dfrac{k_{pv}k_{pi}}{C_f} & T_s\dfrac{k_{pv}}{C_f} \\ T_s k_{iv} k_{pi} & T_s k_{iv} \\ 0 & 0 \\ T_s\dfrac{k_{pi}}{L_f} & 0 \\ T_s k_{ii} & 0 \\ 0 & 0 \end{bmatrix} \begin{bmatrix} I_{g,ref}(k) \\ V_g(k) \end{bmatrix}$$

(5.52)

where T_s is the control sample time, which is selected to be to the reciprocal of the PWM switching frequency.

The overall control structure is shown in Figure 5.11.

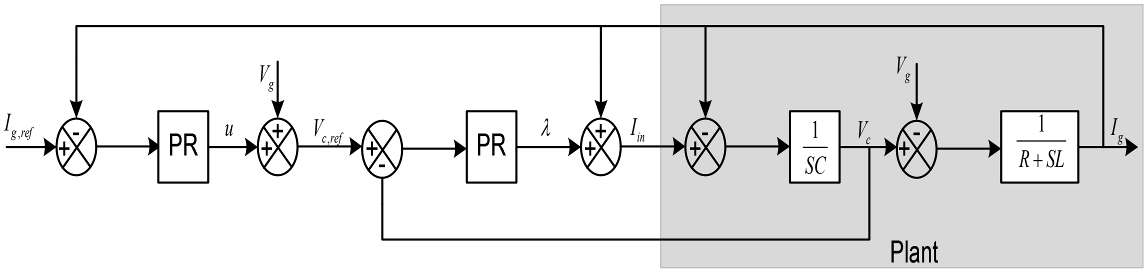

Figure 5.11. AC current and ac voltage loops.

5.6 Simulation

Ten series-connected PV modules with a total rated power of 500W are tested in the proposed system, for which the design specification and circuit parameters are given in Table 5.3. The ac side filter capacitor is selected to attenuate high frequency harmonics that are associated with switching frequency and it sidebands, taking into account the rated ac and dc currents. The converter at rated power is able to supply the ac side active and reactive power demands, and to compensate for filter capacitor and inductor reactive power without crossing the linear modulation index range boundary (*M*=1) into over-modulation. The parameters of the dc side tuned filter are selected as described in section 5.3.

To validate the performance of the proposed system, simulations are performed using Matlab/Simulink. The results of the proposed system under normal weather conditions are shown in Figure 5.12. The PV maximum power is extracted in a relatively short time with small oscillation in the steady state, as shown in Figure 5.12a. Moreover, MPPT successfully locks the dc current to the optimum value, as shown in Figure 5.12b. On the ac side, the PV maximum power is successfully injected into the grid with low THD, high efficiency, and unity power factor. The grid voltage and current are shown in Figure 5.12c, where both are synchronized and the THD of the grid current is only 1.5%. Figure 5.12d shows that the CSI output current restriction is not violated, in allowing switching of one current level at the same time. The grid active and reactive powers are shown in Figure 5.12e. The total system efficiency is 95%, and the power factor is almost unity.

Table 5.3. Design specification and circuit parameters.

Item			Value
PV array rated power,	P	(W)	500
Resonant filter inductor,	L_1	(mH)	10
Resonant filter inductor,	L_2	(mH)	5
Resonant filter capacitor,	C_1	(μF)	125
Resonant filter capacitor,	C_2	(μF)	250
dc link inductor,	L_{dc}	(mH)	5
Switching frequency,	f_s	(kHz)	4
AC line inductor,	L_f	(mH)	1
AC line capacitor,	C_f	(μF)	20
Grid voltage,	$V_{g,rms}$	(V)	110

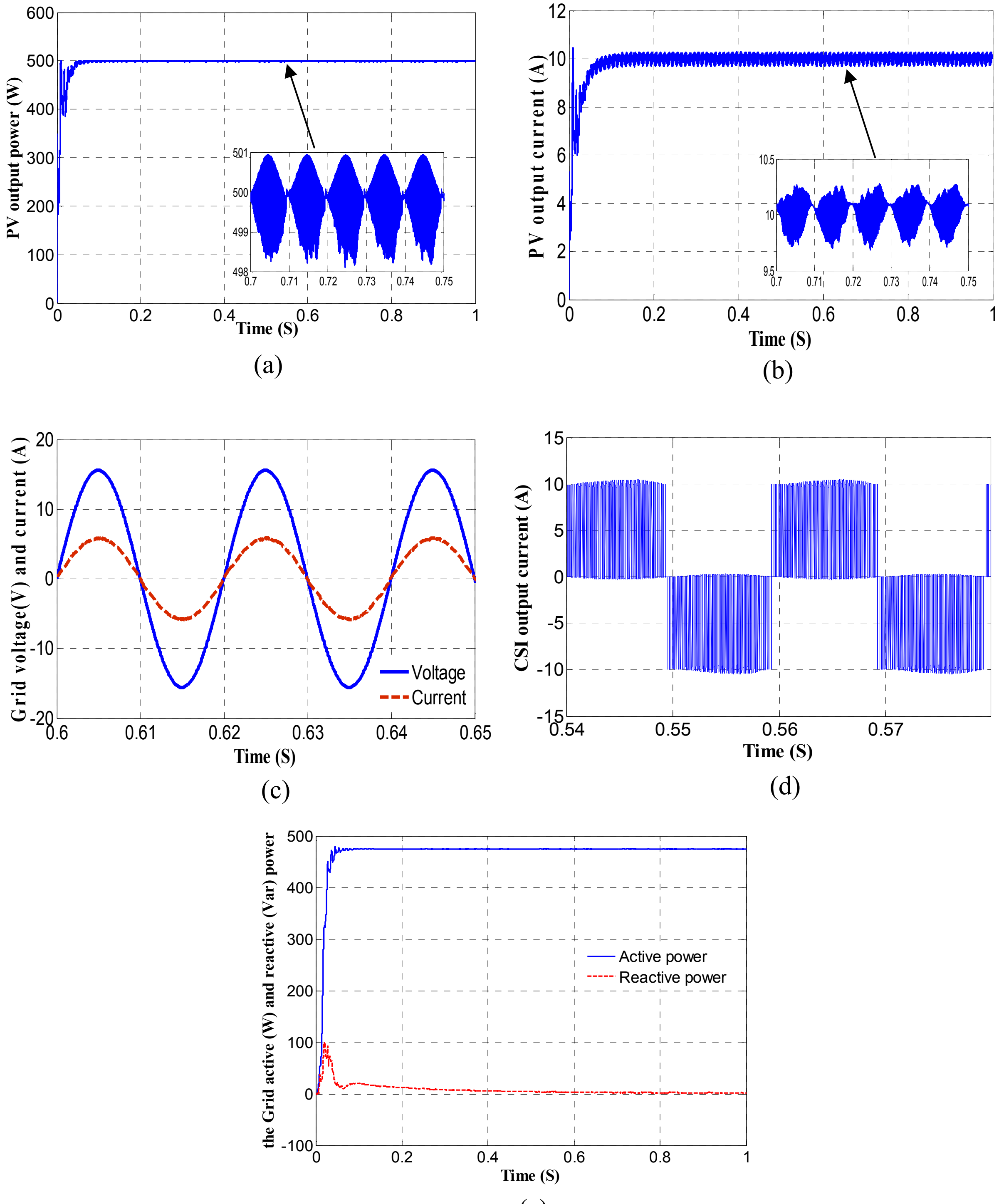

(a)

(b)

(c)

(d)

(e)

Figure 5.12. (a) PV output power,
(b) PV output current, (c) grid voltage (factored by 10) and current,
(d) CSI output current, and (e) grid active and reactive powers.

To demonstrate the effectiveness of the proposed system under varying weather conditions, simulation is carried out at two radiation levels, 500 W/m^2 and 1000 W/m^2. As shown in Figure 5.13a, the PV maximum power point is located in a relatively short time, has a small oscillation around the MPP during steady state, and the new MPP is correctly extracted during varying weather conditions. Also the MPPT maintains the PV output current at its optimum value during both weather conditions, Figure 5.13b shows the current on the dc side. Figure 5.13c shows that the grid current has low THD and unity power factor under both weather conditions. Figure 5.13d shows that the CSI output current does not violate the switching restriction of allowing switching of more than one current level at the same time, at both radiation levels. Figure 5.13f shows the active and reactive powers under both weather conditions. From Figure 5.13a and Figure 5.13e, the total system efficiency is approximately 95% for each radiation level. For further validation of the proposed system efficiency, Figure 5.14 illustrates the efficiency as a function of the input power at different radiation levels.

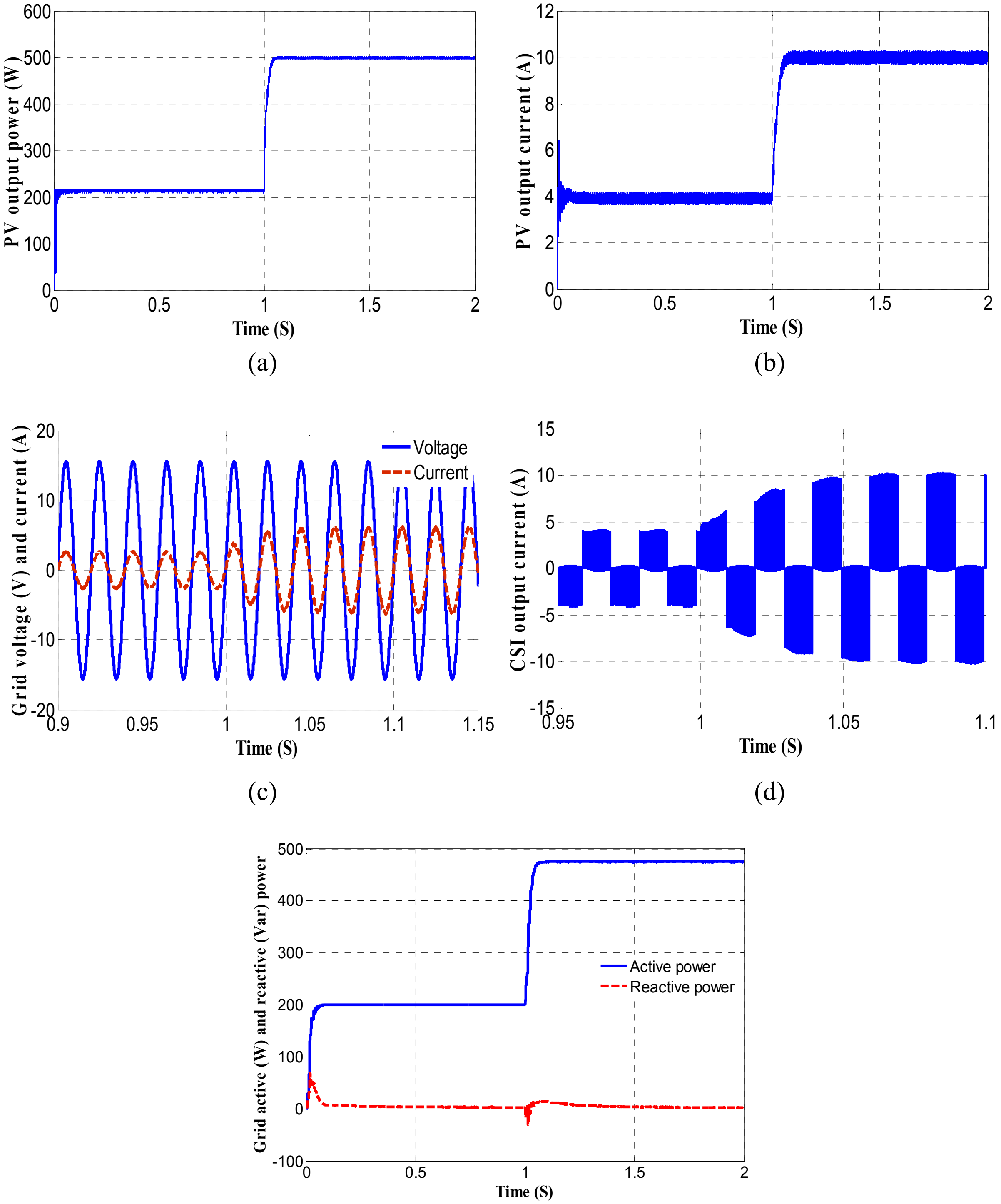

(a) (b)

(c) (d)

(e)

Figure 5.13. Simulation results of the proposed system at two radiation levels, 500 W/m^2 and 1000 W/m^2: (a) PV output power, (b) PV output current, (c) grid voltage (factored by 10) and current, (d) CSI output current, and (e) grid active and reactive powers.

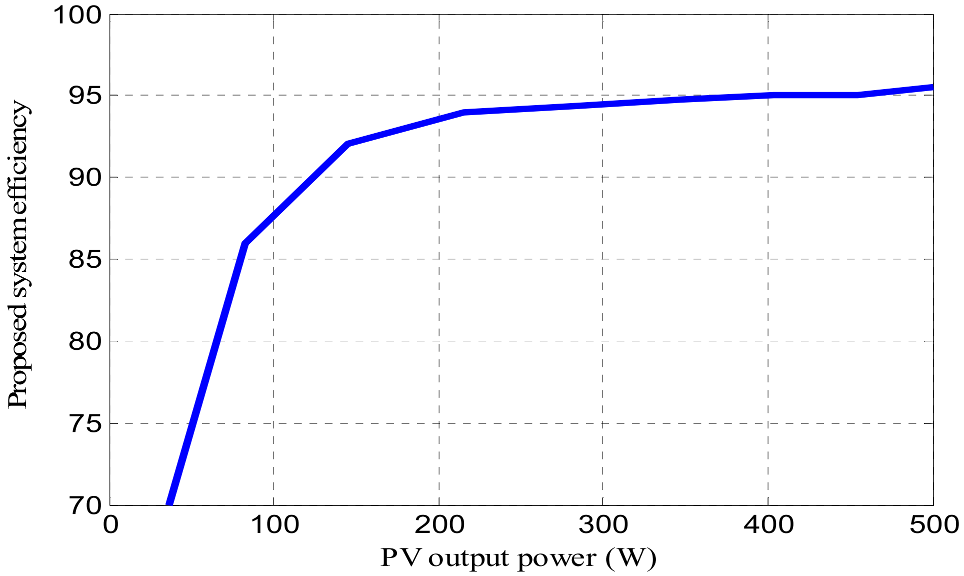

Figure 5.14. Converter efficiency as function of PV output power.

5.7 Experimental results

The performance of the proposed grid-connected CSI is verified experimentally with the hardware shown in Figure 5.15. The experimental setup consists of an Agilent modular solar array simulator to emulate PV system operation; a CSI with a 4 kHz switching frequency to boost the output voltage, track the maximum power point, and interface the PV system to the grid; and a single-phase auto-transformer to emulate the power grid. An Infineon TriCore TC1796 is used to generate the PWM signals and realize the proposed feedback loop controllers.

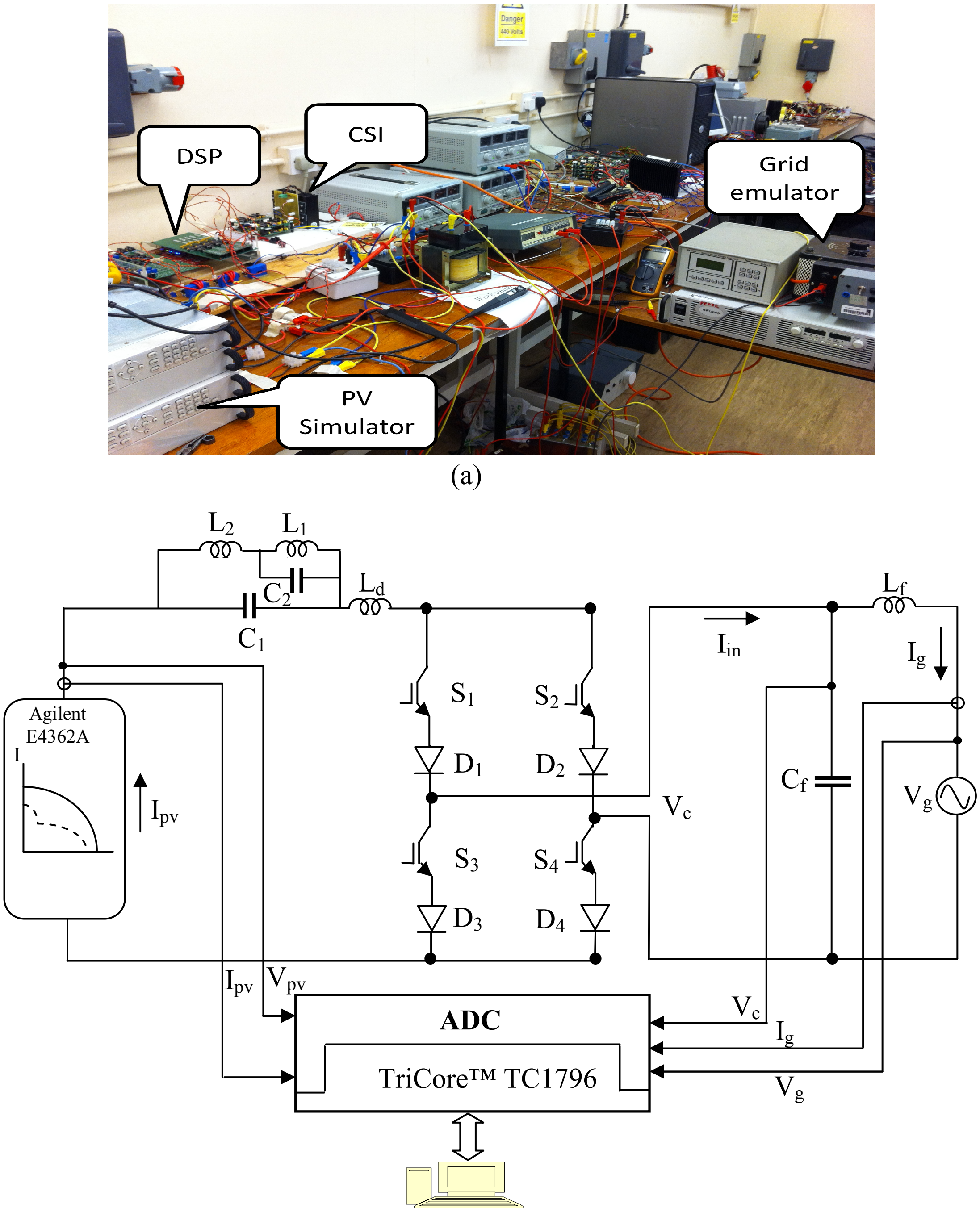

(a)

(b)

Figure 5.15. (a) Test rig photograph and (b) hardware diagram.

5.7.1 Practical Validation of the proposed filter

To validate the effectiveness of the proposed system, the results of the CSI with the double tuned resonant filter are compared with those from the CSI with large dc link inductance, L=300mH. Figure 5.16 shows the input dc current and the output ac voltage and current of the current source inverter under both test conditions. From Figure 5.16a and Figure 5.16b, the double tuned resonant filter and the large inductance filter successfully eliminate even harmonic effects at low modulation indices. The THD at the ac side for the CSI with a resonant filter is 1.29%, whereas the THD for the CSI with large link inductance is 1.92%. On the other converter side, Figure 5.16c and Figure 5.16d show the harmonic effects of both cases at a high modulation index. The proposed double tuned resonant filter successfully eliminates the even-order harmonics in the dc current, reducing the THD on the ac side to 2.73%. However, the CSI with large inductance reduces the THD to 6.16%, which does not meet the IEEE-519 harmonics standard. Since PV applications operate over a wide range of modulation indices to track the MPP, the proposed double tuned filter system is better suited for PV applications.

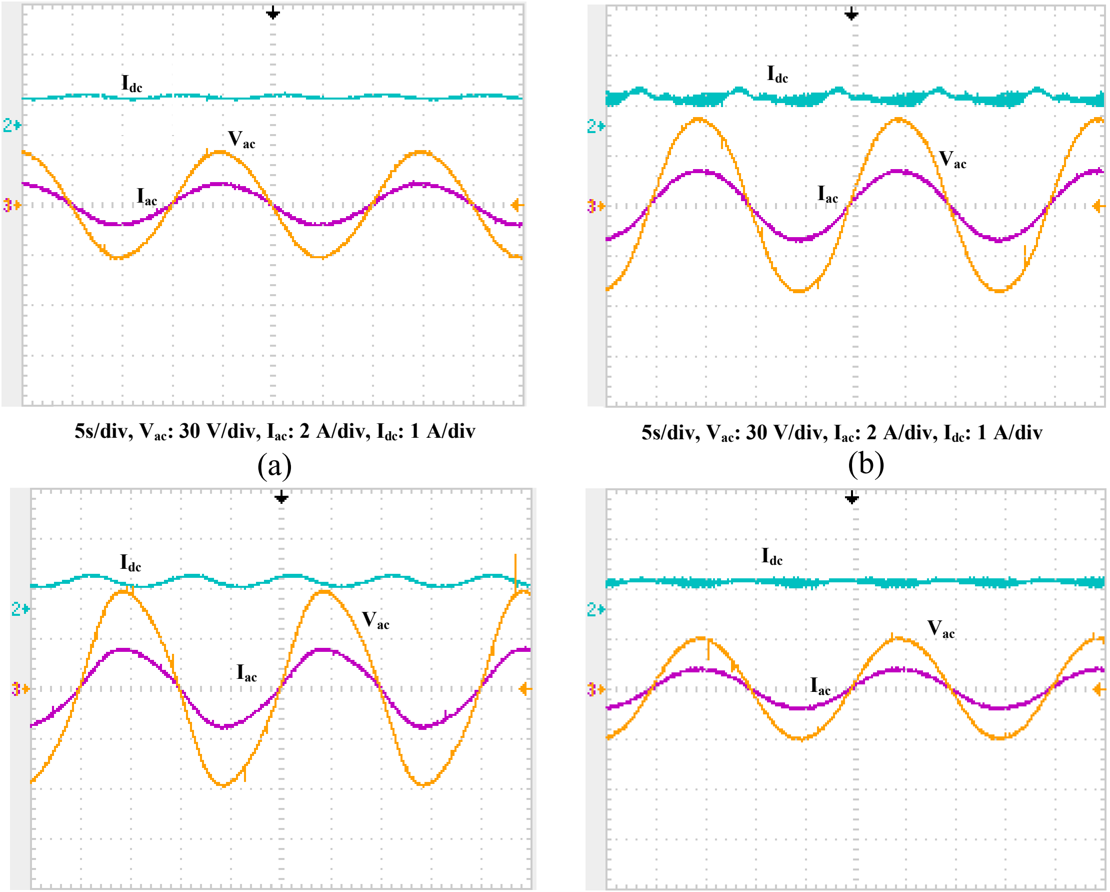

5s/div, V_{ac}: 30 V/div, I_{ac}: 2 A/div, I_{dc}: 1 A/div
(a)

5s/div, V_{ac}: 30 V/div, I_{ac}: 2 A/div, I_{dc}: 1 A/div
(b)

5s/div, V_{ac}: 30 V/div, I_{ac}: 2 A/div, I_{dc}: 1 A/div
(c)

5s/div, V_{ac}: 30 V/div, I_{ac}: 2 A/div, I_{dc}: 1 A/div
(d)

Figure 5.16. Comparison of even harmonics effect on CSI performance (a) CSI with large inductor at M=0.5, (b) CSI with resonant filter at M=0.5, (c) CSI with large inductor at M=0.9, and (d) CSI with resonant filter at M=0.9.

5.7.2 Grid Connection Validation

I-V curves are programmed into the PV source simulator to test the experimental system. The results of the proposed grid-connected CSI are shown in Figure 5.17. The optimum PV current is attained in a relatively short time and has a small steady-state oscillation. Also, the CSI successfully injects the PV current into the grid with low total harmonics distortion.

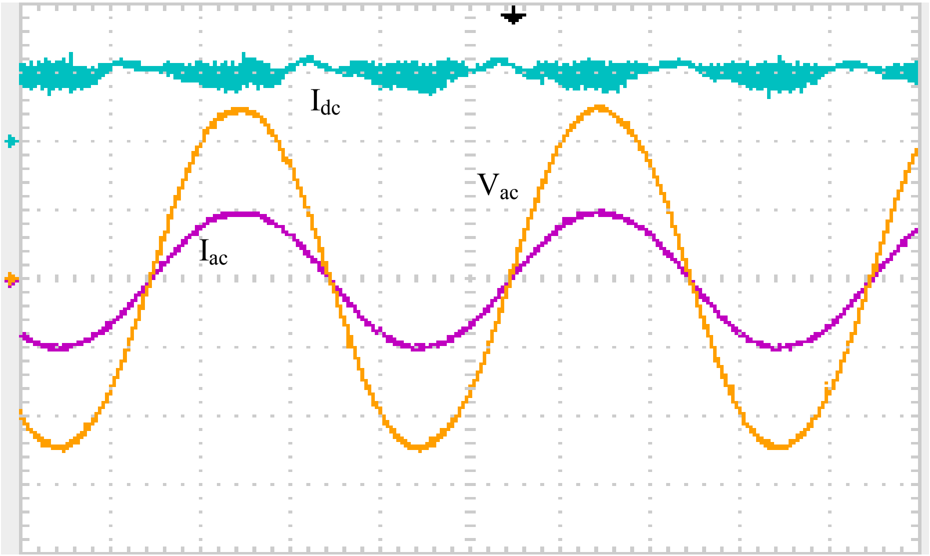

5s/div, V_{ac}: 30 *V*/div, I_{ac}: 2 *A*/div, I_{dc}: 1 *A*/div

Figure 5.17. Experimental results of the proposed grid connected system.

5.8 Summary

A single-stage single-phase grid connected PV system using a CSI has been assessed that meets the grid requirements without using a high dc voltage or a bulky transformer. The control structure of the proposed system consists of MPPT, a current loop, and a voltage loop to improve system performance during normal and varying weather conditions. Since the system consists of a single-stage, the PV power is delivered to the grid with high efficiency, low cost and small footprint. A modified carrier based modulation technique has been proposed to provide a short circuit current path on the dc side to magnetize the inductor after every conduction mode. A dc side double-tuned resonant filter has been used to suppress the second and fourth order harmonics on the dc side, with relatively small inductance. The THD of the grid injected current was 1.5% in simulation and around 2% practically. The feasibility and effectiveness of the proposed system has been successfully evaluated by various simulation studies and practical implementation.

References

[5.1] Y. Bo, L. Wuhua, Z. Yi, and H. Xiangning, "Design and Analysis of a Grid-Connected Photovoltaic Power System," Power Electronics, IEEE Transactions on, vol. 25, pp. 992-1000, 2010.

[5.2] W. Tsai-Fu, C. Chih-Hao, L. Li-Chiun, and K. Chia-Ling, "Power Loss Comparison of Single- and Two-Stage Grid-Connected Photovoltaic Systems," Energy Conversion, IEEE Transactions on, vol. 26, pp. 707-715, 2011.

[5.3] J. M. Carrasco, L. G. Franquelo, J. T. Bialasiewicz, E. Galvan, R. C. P. Guisado, M. A. M. Prats, J. I. Leon, and N. Moreno-Alfonso, "Power-Electronic Systems for the Grid Integration of Renewable Energy Sources: A Survey," Industrial Electronics, IEEE Transactions on, vol. 53, pp. 1002-1016, 2006.

[5.4] D. Barater, G. Buticchi, A. S. Crinto, G. Franceschini, and E. Lorenzani, "Unipolar PWM Strategy for Transformerless PV Grid-Connected Converters," Energy Conversion, IEEE Transactions on, vol. 27, pp. 835-843, 2012.

[5.5] R. A. Mastromauro, M. Liserre, and A. Dell'Aquila, "Control Issues in Single-Stage Photovoltaic Systems: MPPT, Current and Voltage Control," Industrial Informatics, IEEE Transactions on, vol. 8, pp. 241-254, 2012.

[5.6] L. Wuhua and H. Xiangning, "Review of Nonisolated High-Step-Up DC/DC Converters in Photovoltaic Grid-Connected Applications," Industrial Electronics, IEEE Transactions on, vol. 58, pp. 1239-1250, 2011.

[5.7] E. S. Sreeraj, K. Chatterjee, and S. Bandyopadhyay, "One-Cycle-Controlled Single-Stage Single-Phase Voltage-Sensorless Grid-Connected PV System," Industrial Electronics, IEEE Transactions on, vol. 60, pp. 1216-1224, 2013.

[5.8] S. B. Kjaer, J. K. Pedersen, and F. Blaabjerg, "A review of single-phase grid-connected inverters for photovoltaic modules," Industry Applications, IEEE Transactions on, vol. 41, pp. 1292-1306, 2005.

[5.9] G. Petrone, G. Spagnuolo, and M. Vitelli, "A Multivariable Perturb-and-Observe Maximum Power Point Tracking Technique Applied to a Single-Stage Photovoltaic Inverter," Industrial Electronics, IEEE Transactions on, vol. 58, pp. 76-84, 2011.

[5.10] E. Villanueva, P. Correa, J. Rodriguez, and M. Pacas, "Control of a Single-Phase Cascaded H-Bridge Multilevel Inverter for Grid-Connected Photovoltaic Systems," Industrial Electronics, IEEE Transactions on, vol. 56, pp. 4399-4406, 2009.

[5.11] C. Cecati, F. Ciancetta, and P. Siano, "A Multilevel Inverter for Photovoltaic Systems With Fuzzy Logic Control," Industrial Electronics, IEEE Transactions on, vol. 57, pp. 4115-4125, 2010.

[5.12] S. Busquets-Monge, J. Rocabert, P. Rodriguez, S. Alepuz, and J. Bordonau, "Multilevel Diode-Clamped Converter for Photovoltaic Generators With Independent Voltage Control of Each Solar Array," Industrial Electronics, IEEE Transactions on, vol. 55, pp. 2713-2723, 2008.

[5.13] N. A. Rahim, K. Chaniago, and J. Selvaraj, "Single-Phase Seven-Level Grid-Connected Inverter for Photovoltaic System," Industrial Electronics, IEEE Transactions on, vol. 58, pp. 2435-2443, 2011.

[5.14] J. Selvaraj and N. A. Rahim, "Multilevel Inverter For Grid-Connected PV System Employing Digital PI Controller," Industrial Electronics, IEEE Transactions on, vol. 56, pp. 149-158, 2009.

[5.15] L. Liming, L. Hui, W. Zhichao, and Z. Yan, "A Cascaded Photovoltaic System Integrating Segmented Energy Storages With Self-Regulating Power Allocation Control and Wide Range Reactive Power Compensation," Power Electronics, IEEE Transactions on, vol. 26, pp. 3545-3559, 2011.

[5.16] B. Sahan, Arau, x, S. V. jo, No, C. ding, and P. Zacharias, "Comparative Evaluation of Three-Phase Current Source Inverters for Grid Interfacing of Distributed and Renewable Energy Systems," Power Electronics, IEEE Transactions on, vol. 26, pp. 2304-2318, 2011.

[5.17] B. Sahan, A. N. Vergara, N. Henze, A. Engler, and P. Zacharias, "A Single-Stage PV Module Integrated Converter Based on a Low-Power Current-Source Inverter," Industrial Electronics, IEEE Transactions on, vol. 55, pp. 2602-2609, 2008.

[5.18] P. P. Dash and M. Kazerani, "Dynamic Modeling and Performance Analysis of a Grid-Connected Current-Source Inverter-Based Photovoltaic System," Sustainable Energy, IEEE Transactions on, vol. 2, pp. 443-450, 2011.

[5.19] S. Jain and V. Agarwal, "A Single-Stage Grid Connected Inverter Topology for Solar PV Systems With Maximum Power Point Tracking," Power Electronics, IEEE Transactions on, vol. 22, pp. 1928-1940, 2007.

[5.20] A. Darwish, A. K. Abdelsalam, A. M. Massoud, and S. Ahmed, "Single phase grid connected curent source inverter: Mitigation of oscillating power effect on the grid current," in Renewable Power Generation (RPG 2011), IET Conference on, 2011, pp. 1-7.

[5.21] R. T. H. Li, C. Henry Shu-hung, and T. K. M. Chan, "An Active Modulation Technique for Single-Phase Grid-Connected CSI," Power Electronics, IEEE Transactions on, vol. 22, pp. 1373-1382, 2007.

[5.22] K. Hirachi and Y. Tomokuni, "A novel control strategy on single-phase PWM current source inverter incorporating pulse area modulation," in Power Conversion Conference - Nagaoka 1997., Proceedings of the, 1997, pp. 289-294 vol.1.

[5.23] S. Nonaka, "A suitable single-phase PWM current source inverter for utility connected residential PV system," Solar Energy Materials and Solar Cells, vol. 35, pp. 437-444, 1994.

[5.24] S. B. Kjaer, J. K. Pedersen, and F. Blaabjerg, "Power inverter topologies for photovoltaic modules-a review," in Industry Applications Conference, 2002. 37th IAS Annual Meeting. Conference Record of the, 2002, pp. 782-788 vol.2.

[5.25] S. V. Kartalopoulos and I. N. N. Council, Understanding neural networks and fuzzy logic: basic concepts and applications: Institute of Electrical and Electronics Engineers, 1996.

Chapter 6

Conclusions

6.1 General conclusion

After the energy crisis and environmental issues such as global warming and pollution, the development of renewable energy sources has attracted research attention. The penetration into the power grid of renewable power from resources such as solar, wind and tidal has significantly increased. PV (photovoltaic) systems are considered to be one of the most efficient and well accepted renewable energy sources for small and large scale power generation, because of their suitability in distributed generation, mobile applications, and transportation and satellite systems. However, the PV array voltage and current characteristics are highly nonlinear and are affected by irradiance and temperature variation. Moreover, when the radiation is not equally distributed, local and global maxima are introduced in the characteristic curves. For grid-connected PV application, the dc/ac inverter is considered to be the least reliable part. PV system technologies and applications were discussed in chapters one and two.

In chapter three, a new hill climbing search technique was modified based on fuzzy logic control for maximum power point tracking (MPPT) under rapidly changing weather conditions. The rules of hill-climbing search methods have been fuzzified in the proposed MPPT approach to reduce conventional hill climbing disadvantages. The advantages of the proposed controller were verified by Matlab/Simulink simulations and practical experimentation. When compared with conventional hill climbing, the results of the proposed MPPT exhibit faster convergence speed, less oscillation around the MPP under steady-state conditions, and no divergence from the MPP during varying weather conditions. For further validation, the proposed MPPT was evaluated with different simulation studies and compared with existing FLC MPPT techniques.

In chapter four, the MPPT proposed in chapter three was modified to extract the global maximum power point under partially shaded PV system conditions. The proposed MPPT was implemented by combining fuzzy-logic based MPPT with a scanning and storing technique. Three scanning methods were proposed to scan the PV power characteristic curve and store the maximum power value, during initial and varying weather conditions. In addition, the behaviour of the PV characteristic under partial shading conditions has been represented by a new mathematical model.

A single-stage single-phase grid connected PV system using a current source inverter was proposed in chapter five. The system meets grid requirements without using a high dc voltage or a bulky 50/60Hz transformer. To improve system performance during normal and varying weather conditions, the proposed MPPT along with a current loop and a voltage loop are employed in the control system. Utilizing a single stage results in high power efficiency, low cost, and a small footprint. A modified carrier based modulation technique was proposed to provide a short circuit current path on the dc side after every conduction period. Also a double tuned resonant filter was proposed to suppress the second and fourth order harmonics on the dc side, with relatively small inductance. The proposed system has been successfully evaluated with various simulation studies and practical implementation.

6.2 Author's contribution

The contribution of this thesis can be summarized as follows:

- A new fuzzy-logic-based hill-climbing technique is proposed for a MPPT PV system, under rapidly changing weather conditions.
- A modified maximum power point tracking method is proposed to increase PV system performance during partially shaded conditions.
- A mathematical model of a PV system under partial shading conditions is derived.
- A single-phase, single-stage current source inverter based photovoltaic system for grid connection is proposed and substantiated. The system utilizes a transformerless single-stage converter for tracking the maximum power point and interfacing the photovoltaic arrays to the grid.
- To improve the power quality and system efficiency, a double tuned parallel resonant circuit is proposed to attenuate the second and fourth order harmonics on the inverter dc side.

- A modified carrier based modulation technique for the current source inverter is arranged to magnetize the dc link inductor by alternatively short circuiting the bridge converter legs after every active switching cycle.

6.3 Suggestion for future research

The research undertaken in this thesis addresses some PV system challenges related to maximum power point tracking under varying weather conditions, partial shaded effects on the PV model and maximum power point tracking, and interfacing options for the PV system. Suggestions for future research are:

- Standalone photovoltaic storage pumping systems have gained attention for water supply applications. Currently, the existing system utilizes inefficient MPPT. Therefore, the proposed MPPT in this thesis can be further modified to improve MPPT in such systems.
- Investigation of the power-duty cycle characteristic curve can be undertaken to study its behaviour during partial shading conditions.
- The PV emulator is able to behave electrically similar to PV arrays without depending on weather conditions. However, the available PV emulators are quite expensive; therefore, simple and inexpensive PV emulators can be practically implemented by applying the proposed mathematical equation in chapter four.
- Integration options of PVs using different current source inverter configurations could include parallel connection of CSIs and multilevel CSIs.

Appendix A
Test Rig Structure

In this section, hardware elements and simulation package software are introduced in detail. The developed power and control circuits are presented for MPPT under equally distributed radiation, MPPT under partial shadowed conditions, and a grid-connected PV system using CSI.

A.1 Hardware Structure

In figure A.1, a photograph of the system shows that the boost converter and current source inverter are comprised of the following components:

Boost converter:

- DSP: 32-bit TriCore microcontroller;
- Interface circuit;
- Gate drive;
- Current and voltage measuring;
- Power L-filter;
- Agilent modular solar array simulator (Agilent E4362A);
- DC power supply;

Current source inverter:

- DSP: 32-bit TriCore microcontroller;
- Interface circuit;
- Gate drive;
- Current and voltage measuring;
- Power LC-filter;
- Agilent modular solar array simulator (Agilent E4362A);
- DC power supply;

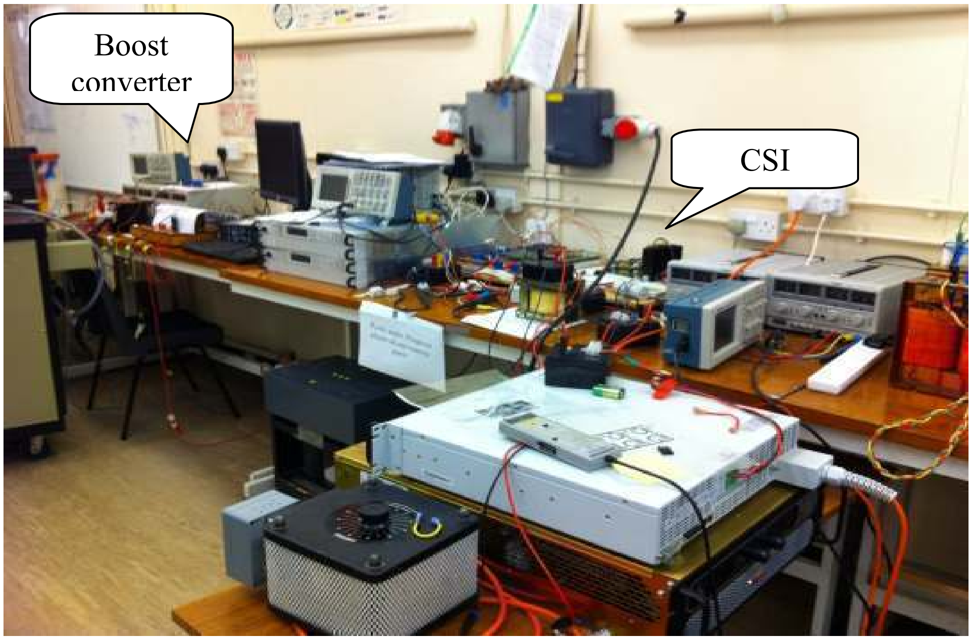

Figure A.1. The whole system photograph.

A.1.1 Microcontroller

During practical evaluation, the control strategy is changed by using an embedded controller. The controller must have some features such as processer speed, storage memory, programming simplicity, and interfacing ability. One of the available candidates is the 32-Bit floating point microcontroller TC1796, Single-Chip TriCoreTM from Infineon. In term of flexibility, reliability, and facilities, the TriCore is considered to be the heart of the control system. The main task of the TriCore is to generate the switching pattern driving the boost converter switch or the current source inverter switches according to the software algorithm of the proposed system. Two interfacing boards are adapted in this system. The first board is connected to the TriCore input; it receives the analogue data from the transducer circuits for the TriCore for calculation. The second interfacing board is connected to the TriCore outputs to send the computed switching pattern driving the boost converter switch or the current source inverter switches. The interfacing circuits are mainly used to isolate the TriCore ground from test rig ground.

The TC 1796 member of the AUDO-NG family - is optimized for highly demanding applications where embedded real-time performance and DSP capabilities combined with an extremely fast interrupt response time and highest level of fault tolerance are needed. AUDO-NG is based on the award-winning unified 32-bit TriCore TM architecture combining RISC, CISC and DSP functionality in a single chip. New innovative peripherals like the Micro Second bus, fast analog-to-digital converter unit or the Micro Link Interface as well as the advanced triple bus structure boosting the overall system performance turn the TC1796 into the most powerful 32-bit microcontroller in the automotive arena.

Figure A.2. TriCore microcontroller.

Features

- High performance 32-bit super-scalar TriCoreTM V1.3 CPU with 4 stage pipeline
  - Superior real-time performance
  - Strong bit handling
  - Fully integrated DSP capabilities
  - Single precision floating point unit (FPU)
  - 150 MHz at full automotive temperature range
- 32-bit Peripheral Control Processor with single cycle instruction (PCP2)
- Memories
  - 2 MByte embedded program flash with ECC
  - 128 KByte data flash for scalable 16 KByte EEPROM emulation
  - 192 KByte on-chip SRAM
  - 16 KByte instruction cache
- 16-channel DMA controller
- 32-bit external bus interface unit with synchronous burst flash access capability
- Sophisticated interrupt system with 2 x 255 hardware priority arbitration levels serviced by CPU and PCP2
- High performing triple bus structure
  - 64-bit local memory buses to internal flash and data memory
  - 32-bit system peripheral bus for interconnections of on-chip peripherals and further functional units
  - 32-bit remote peripheral bus serving the requirements of high speed peripherals
- Two Micro Second bus interfaces (MSC) for port expansion to external Power ASICs
- Two general purpose timer array modules plus separate LTC array with a digital signal filtering and timer functionality to realize autonomous and complex I/O management (GPTA4)
- Two asynchronous/synchronous serial channels with baud rate generator, parity, framing and overrun error detection (ASC)

- Two high speed synchronous serial channels with programmable data length and shift direction (SSC)
- Two high-speed Micro Link Interfaces for serial inter-processor communication (MLI)
- MultiCAN module with four CAN nodes and 128 free assignable message objects for high efficiency data handling via FIFO buffering and gateway data transfer; one CAN node with TTCAN functionality
- 4-channel fast analog-to-digital converter unit (FADC) with concatenated comb filters for hardware data reduction; 10-bit resolution/min. conversion time 280 ns
- Two 16-channel analog-to-digital converter units (ADC) with 8-bit, 10-bit or 12-bit resolution
- 44 analog input lines for ADC and FADC
- 123 digital general purpose I/O lines, 4 input lines
- Digital I/O ports with 3.3 V capability
- On-chip debug support OCDS level 1 + 2 (CPU, PCP, DMA)
- Dedicated emulation device chip for multicore debugging, tracing and calibration via USB .1 interface (TC1796ED)
- Power management system
- Clock generation unit with PLL
- Supply Voltage 1.5 V
- I/O Voltage 3.3 V
- Full automotive temperature range -40° to +125°C
- P-BGA-416 package

A.1.2 Interface circuits

For safety purposes, two interfacing board have been used to isolate the DSP from the external circuits. The first interfacing board isolates the ADC channels of the microcontroller from the voltage and current transducers while the second interfacing board isolates the PWM channels from the gate drive circuits. The interfacing board circuit consists of differential amplifiers, linear optocouplers, and emitter-followers. A photograph of the interfacing circuit is shown in figure A.3. Schematics diagrams of the output and analogue input interfacing circuit are shown in figures A.4 and A.5, respectively.

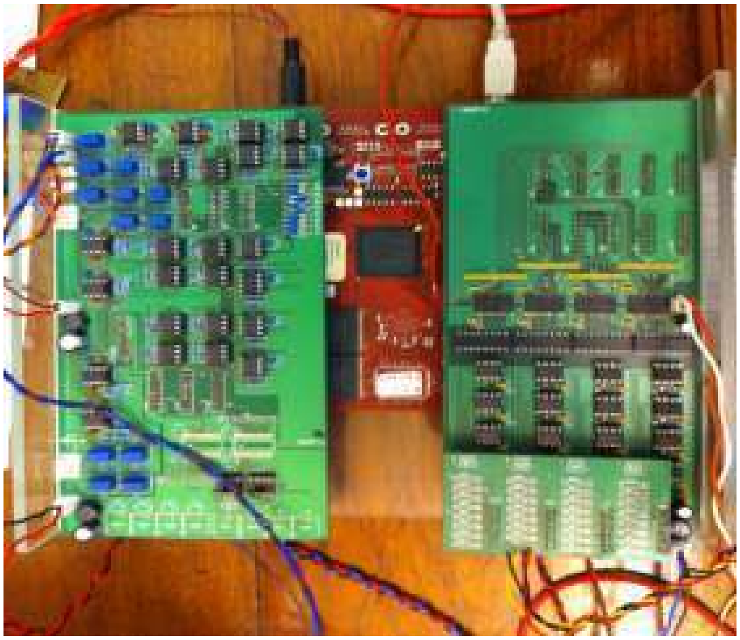

Figure A.3. Interfacing board.

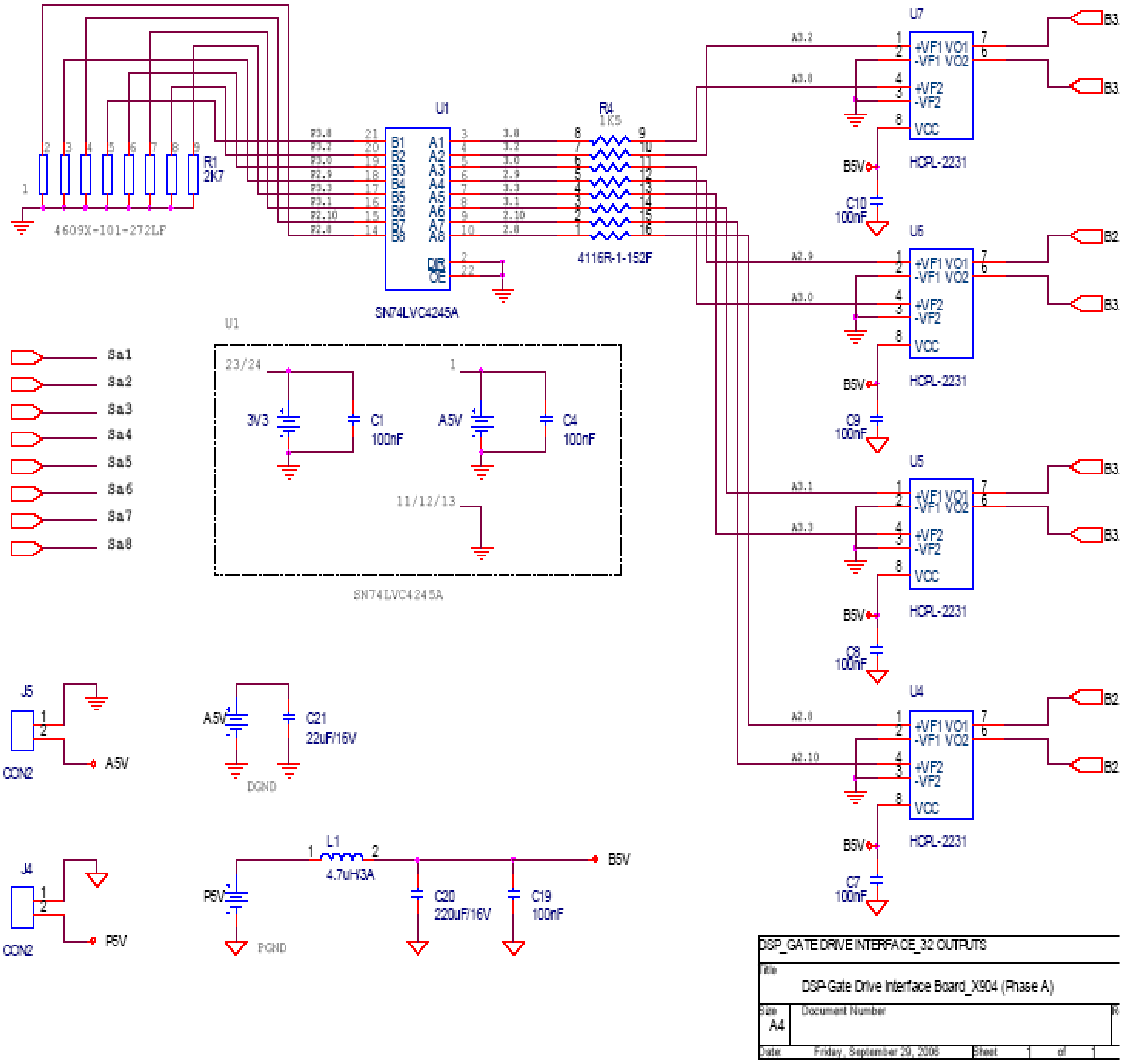
U7
U6
U5
U4
+VF1 VO1
-VF1 VO2
+VF2
-VF2
VCC
HCPL-2231
B5V
C10
C9
C8
C7
100nF
A3.2
A3.0
A2.9
A3.1
A3.3
A2.8
A2.10
B3
B2
R4
1K5
4116R-1-152F
U1
B1
B2
B3
B4
B5
B6
B7
B8
A1
A2
A3
A4
A5
A6
A7
A8
DIR
OE
SN74LVC4245A
R1
2K7
4609X-101-272LF
P3.8
P3.2
P3.0
P2.9
P3.3
P3.1
P2.10
P2.8
P2.8
P2.10
P3.1
P3.3
P2.9
P3.0
P3.2
P3.8
Sa1
Sa2
Sa3
Sa4
Sa5
Sa6
Sa7
Sa8
U1
23/24
3V3
C1
100nF
1
A5V
C4
100nF
11/12/13
SN74LVC4245A
J5
CON2
A5V
C21
22uF/16V
DGND
J4
CON2
P5V
L1
4.7uH3A
C20
220uF/16V
C19
100nF
B5V
PGND
DSP_GATE DRIVE INTERFACE_32 OUTPUTS
Title
DSP-Gate Drive Interface Board_X904 (Phase A)
Size
A4
Document Number
Date:
Friday, September 29, 2006
Sheet
1
of
1

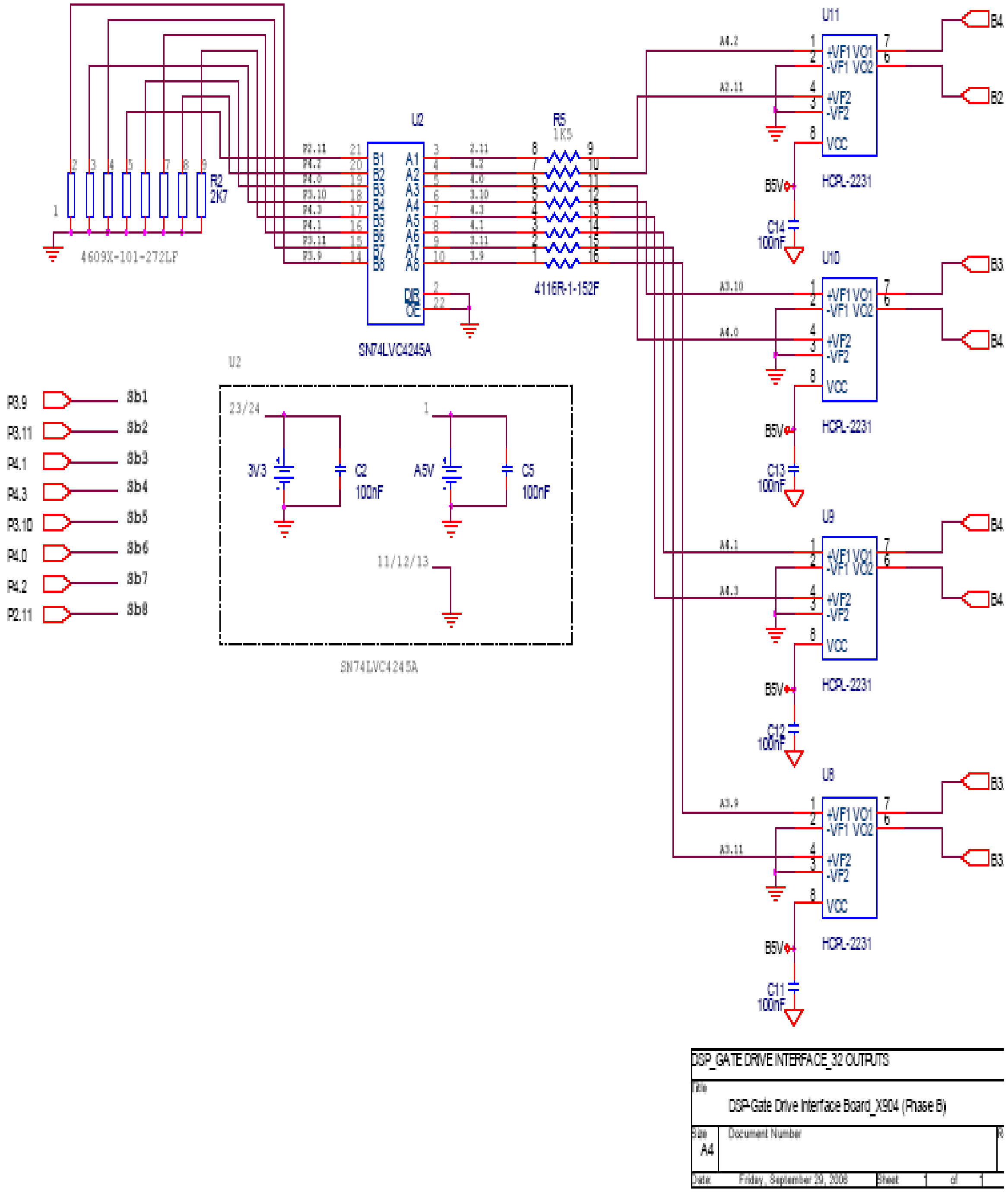
R2
2K7
4609X-101-272LF
U2
B1
B2
B3
B4
B5
B6
B7
B8
A1
A2
A3
A4
A5
A6
A7
A8
DIR
OE
SN74LVC4245A
P2.11
P4.2
P4.0
P3.10
P4.3
P4.1
P3.11
P3.9
2.11
4.2
4.0
3.10
4.3
4.1
3.11
3.9
R5
1K5
4116R-1-152F
U11
U10
U9
U8
+VF1
-VF1
+VF2
-VF2
VCC
VO1
VO2
HCPL-2231
A4.2
A2.11
A3.10
A4.0
A4.1
A4.3
A3.9
A3.11
B5V
C14
C13
C12
C11
100nF
B4
B2
B3
P3.9
P3.11
P4.1
P4.3
P3.10
P4.0
P4.2
P2.11
Sb1
Sb2
Sb3
Sb4
Sb5
Sb6
Sb7
Sb8
U2
23/24
1
11/12/13
3V3
A5V
C2
C5
100nF
SN74LVC4245A
DSP_GATE DRIVE INTERFACE_32 OUTPUTS
Title
DSP-Gate Drive Interface Board_X904 (Phase B)
Size
A4
Document Number
R
Date:
Friday, September 29, 2008
Sheet
1
of
1

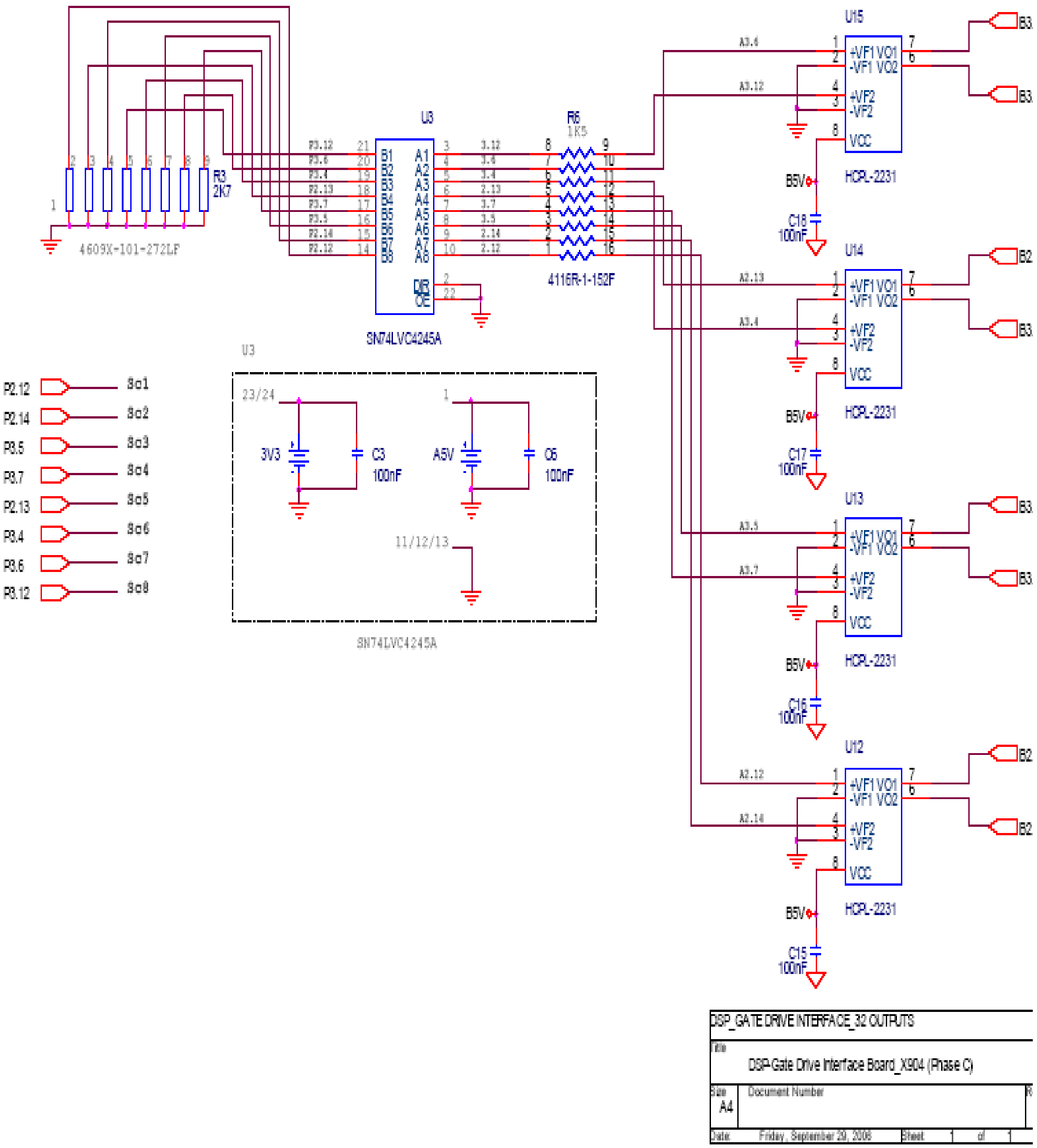
U3
SN74LVC4245A
B1 B2 B3 B4 B5 B6 B7 B8
A1 A2 A3 A4 A5 A6 A7 A8
DIR
OE
R3
2K7
4609X-101-272LF
R6
1K5
4116R-1-152F
U15
U14
U13
U12
+VF1 VO1
-VF1 VO2
+VF2
-VF2
VCC
HCPL-2231
B5V
C18 100nF
C17 100nF
C16 100nF
C15 100nF
A3.6
A3.12
A2.13
A3.4
A3.5
A3.7
A2.12
A2.14
B3
B2
P2.12 Sa1
P2.14 Sa2
P3.5 Sa3
P3.7 Sa4
P2.13 Sa5
P3.4 Sa6
P3.6 Sa7
P3.12 Sa8
U3
23/24
3V3
C3 100nF
1
A5V
C6 100nF
11/12/13
SN74LVC4245A
DSP_GATE DRIVE INTERFACE_32 OUTPUTS
Title
DSP-Gate Drive Interface Board_X904 (Phase C)
Size
A4
Document Number
Date: Friday, September 29, 2006
Sheet 1 of 1

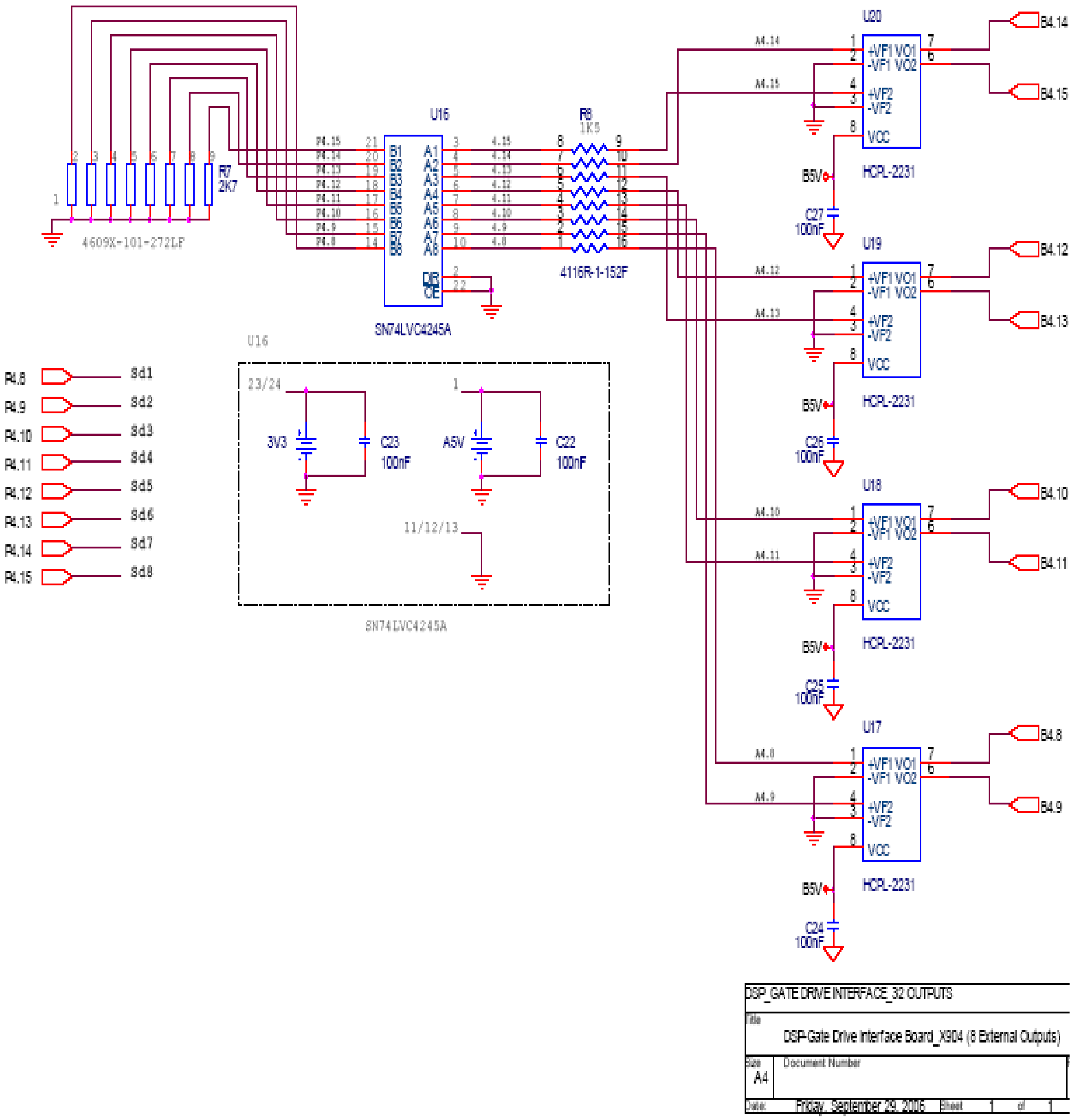
U16
SN74LVC4245A
R7
2K7
4609X-101-272LF
R8
1K5
4116R-1-152F
U20
U19
U18
U17
HCPL-2231
+VF1 VO1
-VF1 VO2
+VF2
-VF2
VCC
B5V
C27
C26
C25
C24
100nF
B4.14
B4.15
B4.12
B4.13
B4.10
B4.11
B4.8
B4.9
A4.14
A4.15
A4.12
A4.13
A4.10
A4.11
A4.8
A4.9
DIR
OE
P4.8
P4.9
P4.10
P4.11
P4.12
P4.13
P4.14
P4.15
Sd1
Sd2
Sd3
Sd4
Sd5
Sd6
Sd7
Sd8
3V3
C23
100nF
A5V
C22
100nF
23/24
1
11/12/13
SN74LVC4245A
DSP_GATE DRIVE INTERFACE_32 OUTPUTS
Title
DSP-Gate Drive Interface Board_X904 (8 External Outputs)
Size
A4
Document Number
Date:
Friday, September 29, 2006
Sheet
1
of
1

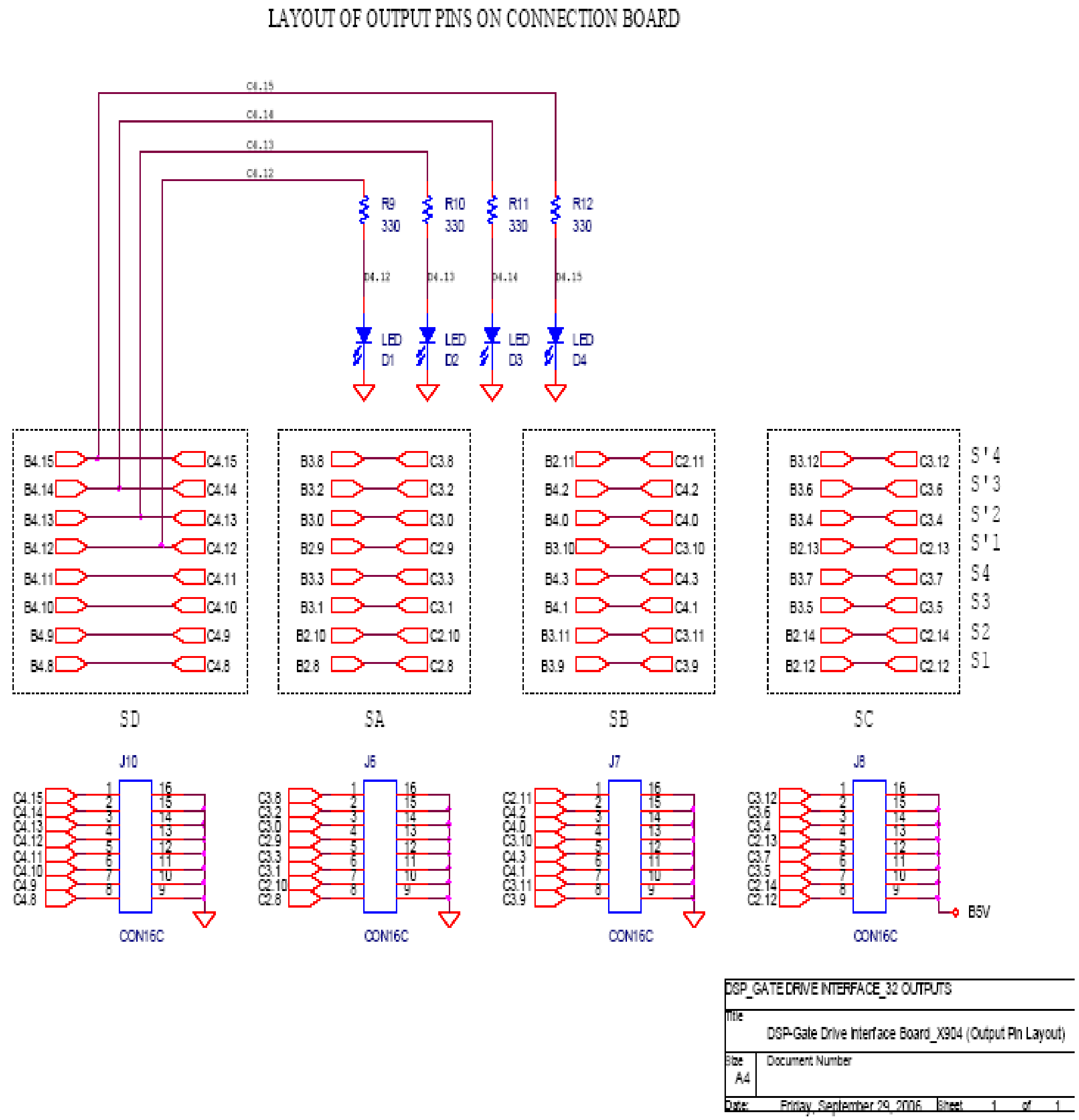

Figure A.4. 8-output PWM interfacing board.

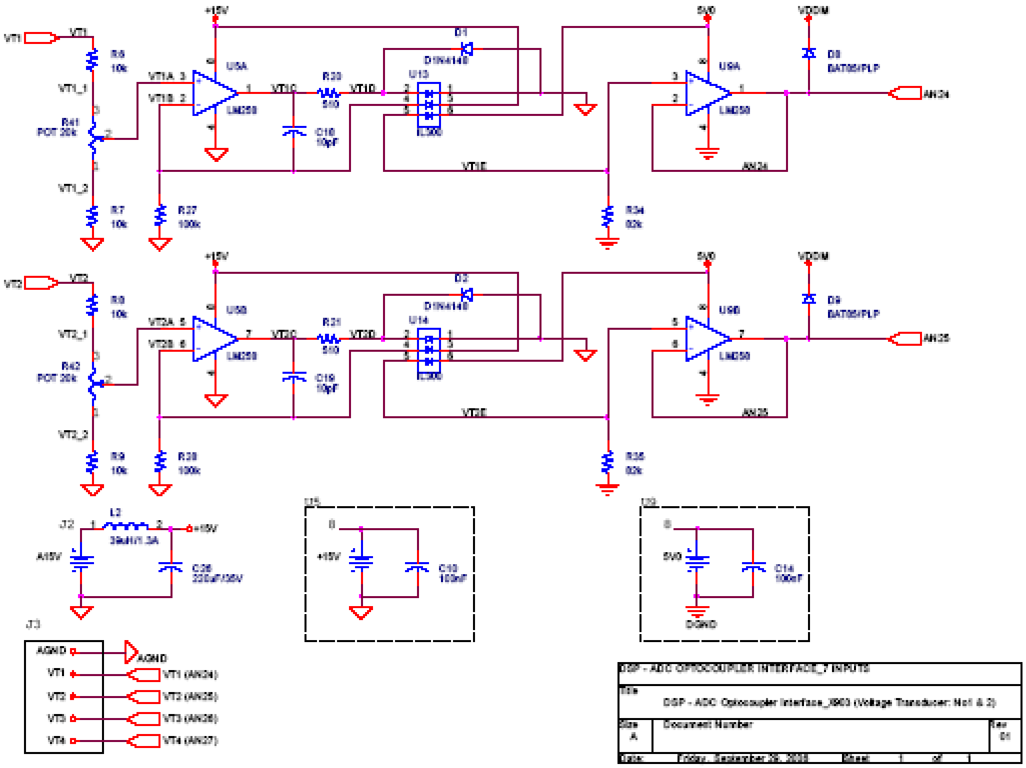
VT1
VT1
R6
10k
VT1_1
R41
POT 20k
VT1_2
R7
10k
+15V
VT1A 3
VT1B 2
U5A
LM258
1
VT1C
C18
10pF
R27
100k
R20
510
VT1D
D1
D1N4148
U13
IL300
VT1E
R34
82k
5V0
U9A
LM358
AN24
VDDM
D8
BAT85/PLP
AN24
VT2
VT2
R8
10k
VT2_1
R42
POT 20k
VT2_2
R9
10k
+15V
VT2A 5
VT2B 6
U5B
LM258
7
VT2C
C19
10pF
R28
100k
R21
510
VT2D
D2
D1N4148
U14
IL300
VT2E
R35
82k
5V0
U9B
LM358
AN25
VDDM
D9
BAT85/PLP
AN25
J2
L2
39uH/1.3A
A15V
+15V
C26
220uF/35V
U5
8
+15V
C13
100nF
U9
8
5V0
C14
100nF
DGND
J3
AGND
VT1
VT2
VT3
VT4
AGND
VT1 (AN24)
VT2 (AN25)
VT3 (AN26)
VT4 (AN27)
DSP - ADC OPTOCOUPLER INTERFACE_7 INPUTS
Title
DSP - ADC Optocoupler Interface_8903 (Voltage Transducer: No1 & 2)
Size
A
Document Number
Rev
01
Date:
Friday, September 26, 2008
Sheet
1
of
1

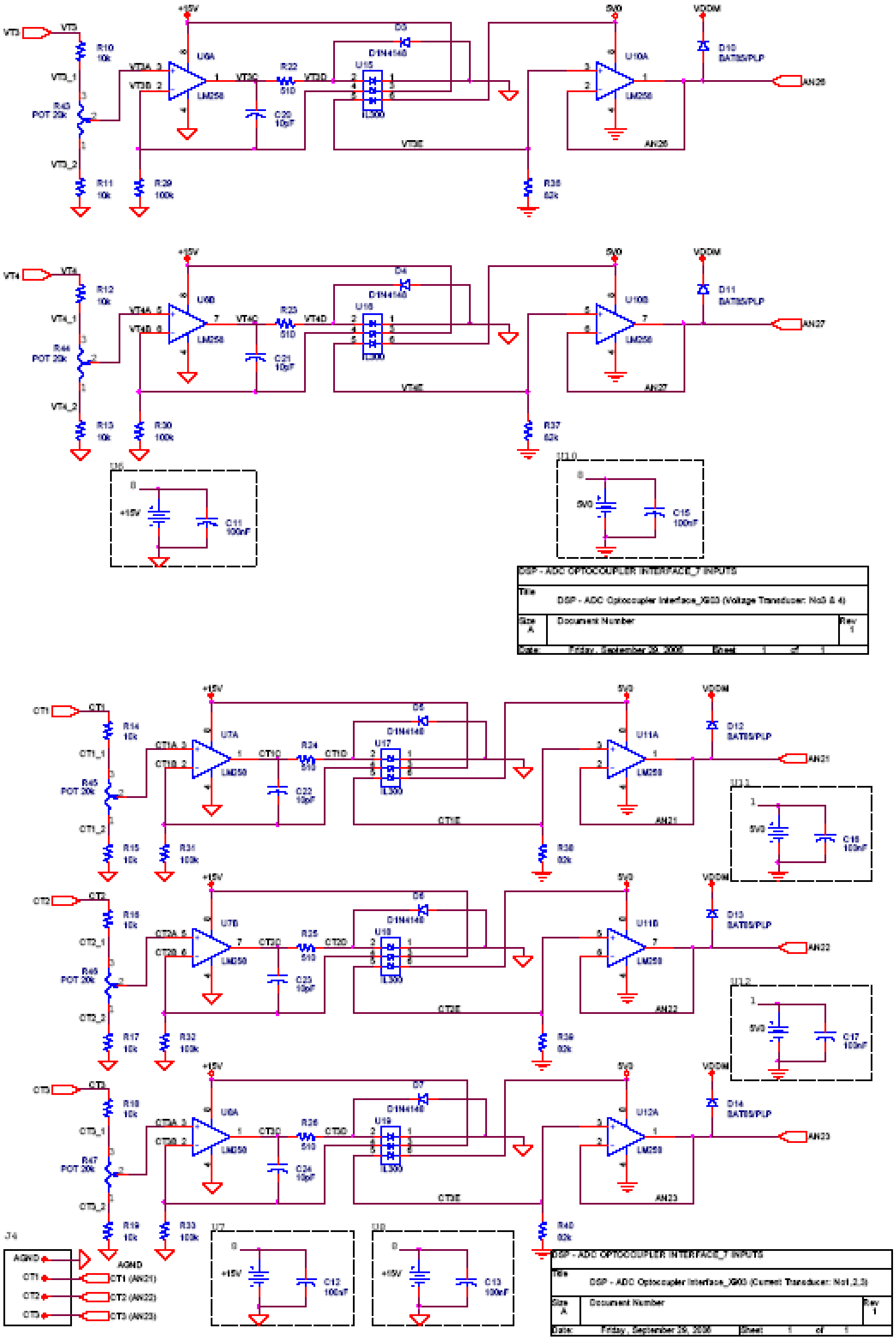

Figure A.5. 7-inputs ADC interfacing board.

A.1.3 Gate drive circuit

Normally, the control circuit sinks milli-ampere level current, while the gate terminal of an IGBT requires a large spike of instantaneous current to quickly charge the gate capacitance and enhance the turning on time of the switch. Therefore, gate drive circuits are required to source enough current for the switches. Moreover, galvanic isolation between the controller common ground and the switches common points is required. The gate drive photo and the circuit schematic are shown in figures A.6 and A.7, respectively. Table A.1 shows the parameters of the gate drive circuit.

Table A.1. Gate drive circuit parameters.

Output voltage	15 V
Output current	±3A
Supply voltage (max)	5V
Output frequency (max)	75kHz
$t_{d\ on}$	60 ns
$t_{s\ off}$	60 ns

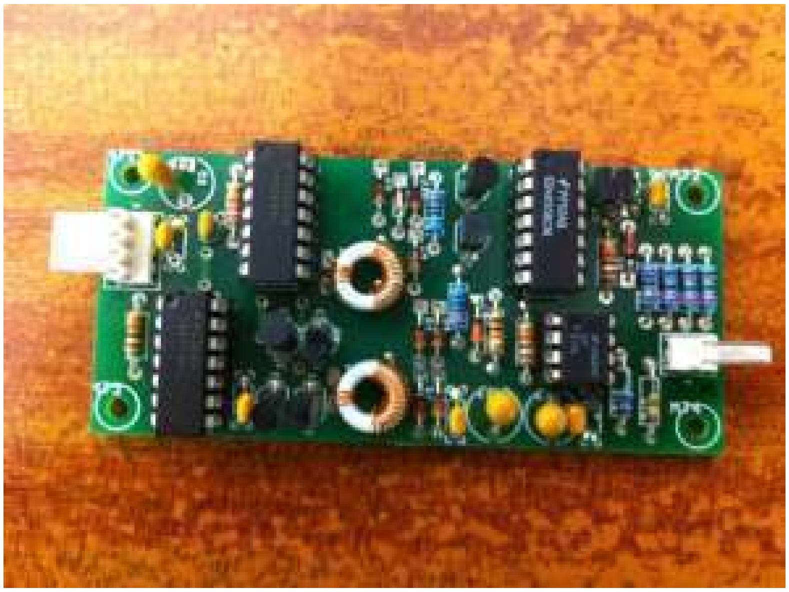

Figure A.6. Gate drive circuit.

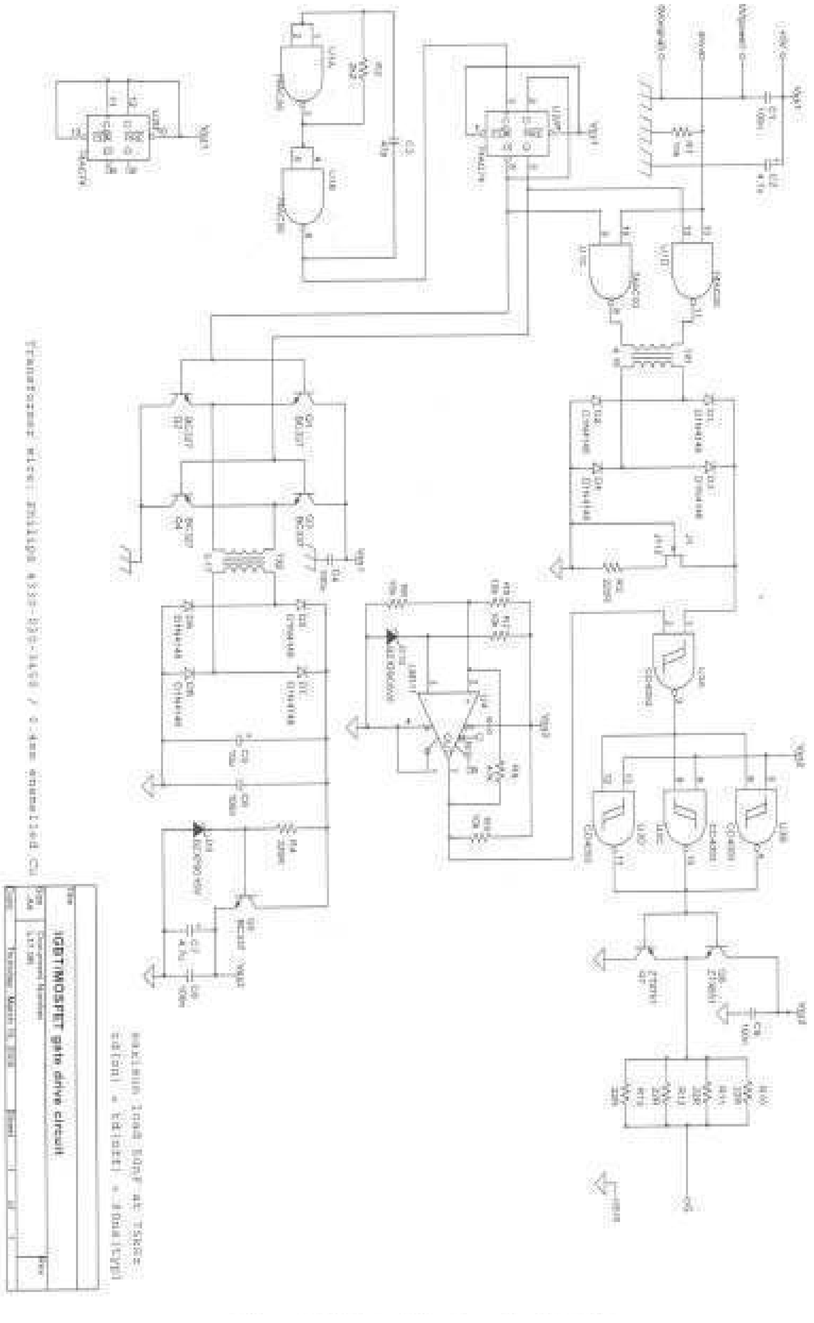

Figure A.7. Schematic diagram of the current transducer circuit.

A.1.4 Current and voltage measurement

To provide feedback signals to the controller, current and voltage sensing is required. Therefore, current and voltage transducer boards are used.

i. Current Sensing

In chapter three and four, the PV output current is needed for the maximum power point tracker. In chapter five, the dc side current is required for the maximum power point tracker and the ac current is required for the current loop. In this thesis, Hall effect current sensor devices **LEM (FB-55P)** were used. This type of sensor has the advantage of isolating the sensing signal and is easy to implement. The sensing range of the Hall effect current sensor varies between 0A to 50A, and the frequency range varies between dc to 100 kHz. For appropriate operation, signal conditioning is applied to amplify the transducer output and fed to the controller circuit. Figure A.8 shows the schematic diagram of the current transducer along with the signal conditioning circuit.

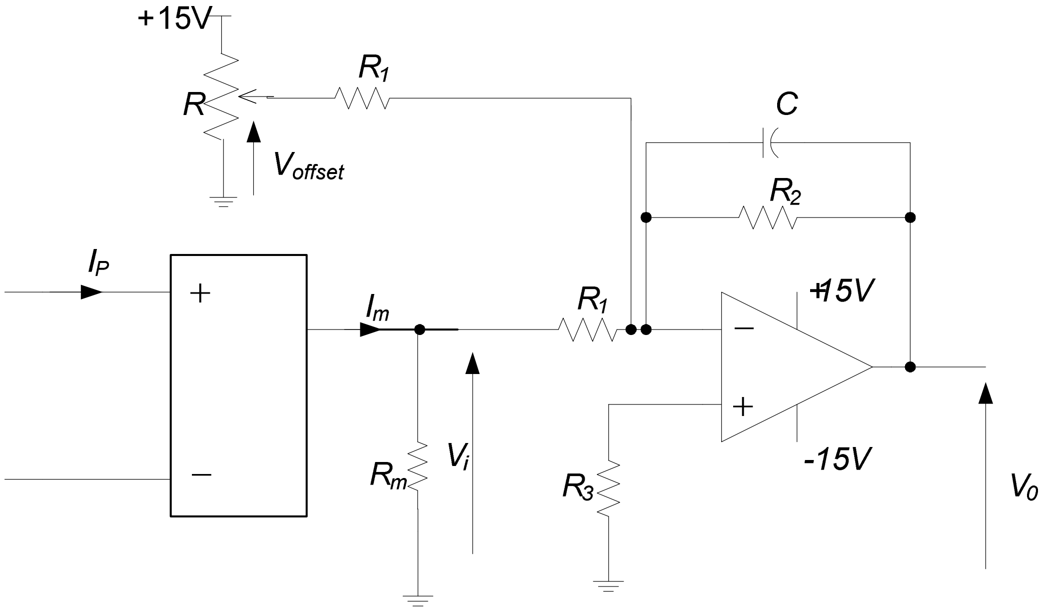

Figure A.8. Schematic diagram of the current transducer circuit.

Current Transducer LA 55-P

I_{PN} = 50 A

For the electronic measurement of currents : DC, AC, pulsed..., with a galvanic isolation between the primary circuit (high power) and the secondary circuit (electronic circuit).

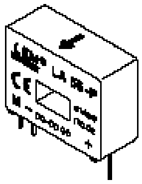

Electrical data

I_{PN}	Primary nominal r.m.s. current	50	A
I_P	Primary current, measuring range	0 .. ± 70	A
R_M	Measuring resistance @		

		T_A = 70°C $R_{M\,min}$	 $R_{M\,max}$	T_A = 85°C $R_{M\,min}$	 $R_{M\,max}$	
with ± 12 V	@ ± 50 A_{max}	10	100	60	95	Ω
	@ ± 70 A_{max}	10	50	60[1]	60[1]	Ω
with ± 15 V	@ ± 50 A_{max}	50	160	135	155	Ω
	@ ± 70 A_{max}	50	90	135[2]	135[2]	Ω

I_{SN}	Secondary nominal r.m.s. current	50	mA
K_N	Conversion ratio	1 : 1000	
V_C	Supply voltage (± 5 %)	± 12 .. 15	V
I_C	Current consumption	10 (@ ±15 V) + I_S	mA
V_d	R.m.s. voltage for AC isolation test, 50 Hz, 1 mn	2.5	kV

Accuracy - Dynamic performance data

X	Accuracy @ I_{PN} , T_A = 25°C	@ ± 15 V (± 5 %)	± 0.65	%
		@ ± 12 .. 15 V (± 5 %)	± 0.90	%
ε_L	Linearity		< 0.15	%

			Typ	Max	
I_O	Offset current @ I_P = 0, T_A = 25°C			± 0.2	mA
I_{OM}	Residual current[3] @ I_P = 0, after an overload of 3 x I_{PN}			± 0.3	mA
I_{OT}	Thermal drift of I_O	0°C .. + 70°C	± 0.1	± 0.5	mA
		- 25°C .. + 85°C	± 0.1	± 0.6	mA

t_{ra}	Reaction time @ 10 % of $I_{P\,max}$	< 500	ns
t_r	Response time @ 90 % of $I_{P\,max}$	< 1	µs
di/dt	di/dt accurately followed	> 200	A/µs
f	Frequency bandwidth (- 1 dB)	DC .. 200	kHz

General data

T_A	Ambient operating temperature		- 25 .. + 85	°C
T_S	Ambient storage temperature		- 40 .. + 90	°C
R_S	Secondary coil resistance @	T_A = 70°C	80	Ω
		T_A = 85°C	85	Ω
m	Mass		18	g
	Standards[4]		EN 50178	

Features

- Closed loop (compensated) current transducer using the Hall effect
- Printed circuit board mounting
- Insulated plastic case recognized according to UL 94-V0.

Advantages

- Excellent accuracy
- Very good linearity
- Low temperature drift
- Optimized response time
- Wide frequency bandwidth
- No insertion losses
- High immunity to external interference
- Current overload capability.

Applications

- AC variable speed drives and servo motor drives
- Static converters for DC motor drives
- Battery supplied applications
- Uninterruptible Power Supplies (UPS)
- Switched Mode Power Supplies (SMPS)
- Power supplies for welding applications.

Notes :
[1] Measuring range limited to ± 60 A_{max}
[2] Measuring range limited to ± 55 A_{max}
[3] Result of the coercive field of the magnetic circuit
[4] A list of corresponding tests is available

980706/8

ii. Voltage sensing

In chapter three and four, the PV output voltage needs to be measured for the maximum power point tracker. In chapter five, the dc side voltage is required for the maximum power point tracker and the capacitor voltage and grid voltage are required for the voltage control loop. Connecting the voltage directly to the controller will likely damage the whole control circuit. Therefore, to get the proper voltage, operational amplifier a signal conditioning circuitry is used. Hall effect voltage sensor devices **LEM (LV25-P)** were used. The sensing range of the voltage sensor varies between 0V to 500V with a high frequency bandwidth. Figure A.9 shows the schematic diagram of the voltage transducer along with the signal conditioning circuit.

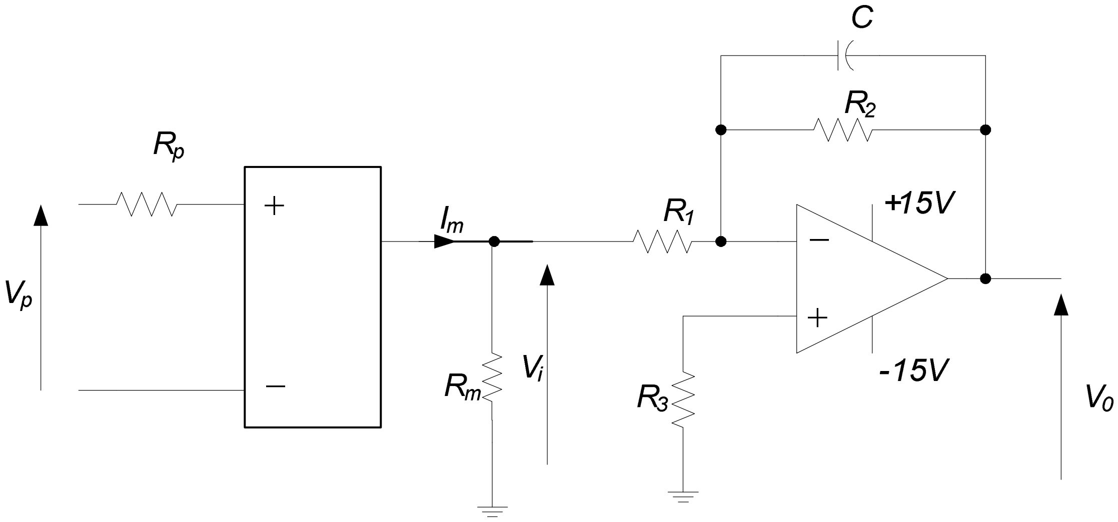

Figure A.9. Schematic diagram of the voltage transducer circuit.

Voltage Transducer LV 25-P

For the electronic measurement of voltages : DC, AC, pulsed..., with a galvanic isolation between the primary circuit (high voltage) and the secondary circuit (electronic circuit).

Electrical data

I_{PN}	Primary nominal r.m.s. current		10		mA
I_P	Primary current, measuring range		0 .. ± 14		mA
R_M	Measuring resistance		$R_{M\,min}$	$R_{M\,max}$	
	with ± 12 V	@ ± 10 mA$_{max}$	30	190	Ω
		@ ± 14 mA$_{max}$	30	100	Ω
	with ± 15 V	@ ± 10 mA$_{max}$	100	350	Ω
		@ ± 14 mA$_{max}$	100	190	Ω
I_{SN}	Secondary nominal r.m.s. current		25		mA
K_N	Conversion ratio		2500 : 1000		
V_C	Supply voltage (± 5 %)		± 12 .. 15		V
I_C	Current consumption		10 (@±15 V)+I_S		mA
V_d	R.m.s. voltage for AC isolation test 1), 50 Hz, 1 mn		2.5		kV

Accuracy - Dynamic performance data

X_G	Overall Accuracy @ I_{PN}, T_A = 25°C	@ ± 12 .. 15 V	± 0.9		%
		@ ± 15 V (± 5 %)	± 0.8		%
ε_L	Linearity		< 0.2		%
			Typ	Max	
I_O	Offset current @ I_P = 0, T_A = 25°C			± 0.15	mA
I_{OT}	Thermal drift of I_O	0°C .. + 25°C	± 0.06	± 0.25	mA
		+ 25°C .. + 70°C	± 0.10	± 0.35	mA
t_r	Response time 2) @ 90 % of $V_{P\,max}$		40		μs

General data

T_A	Ambient operating temperature	0 .. + 70	°C
T_S	Ambient storage temperature	- 25 .. + 85	°C
R_P	Primary coil resistance @ T_A = 70°C	250	Ω
R_S	Secondary coil resistance @ T_A = 70°C	110	Ω
m	Mass	22	g
	Standards 3)	EN 50178	

I_{PN} = 10 mA

V_{PN} = 10 .. 500 V

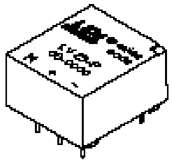

Features

- Closed loop (compensated) voltage transducer using the Hall effect
- Insulated plastic case recognized according to UL 94-V0.

Principle of use

- For voltage measurements, a current proportional to the measured voltage must be passed through an external resistor R_1 which is selected by the user and installed in series with the primary circuit of the transducer.

Advantages

- Excellent accuracy
- Very good linearity
- Low thermal drift
- Low response time
- High bandwidth
- High immunity to external interference
- Low disturbance in common mode.

Applications

- AC variable speed drives and servo motor drives
- Static converters for DC motor drives
- Battery supplied applications
- Uninterruptible Power Supplies (UPS)
- Power supplies for welding applications.

Notes : 1) Between primary and secondary

2) R_1 = 25 kΩ (L/R constant, produced by the resistance and inductance of the primary circuit)

3) A list of corresponding tests is available

981125/14

A.1.5 Agilent E4362A modules and Agilent E4360A mainframe

The PV simulator Agilent E4362A modules and Agilent E4360 mainframe is a dc current source with low output capacitance that simulates the output characteristics of a PV array. It is capable of simulating the PV characteristic curve under different weather conditions. GPIB, LAN, and USB interfaces as well as from the front panel can be used to program the PV characteristic. The SAS has different operation modes such as fixed mode, SAS mode and table mode. The specification guide of the PV simulator is shown in figure A.10.

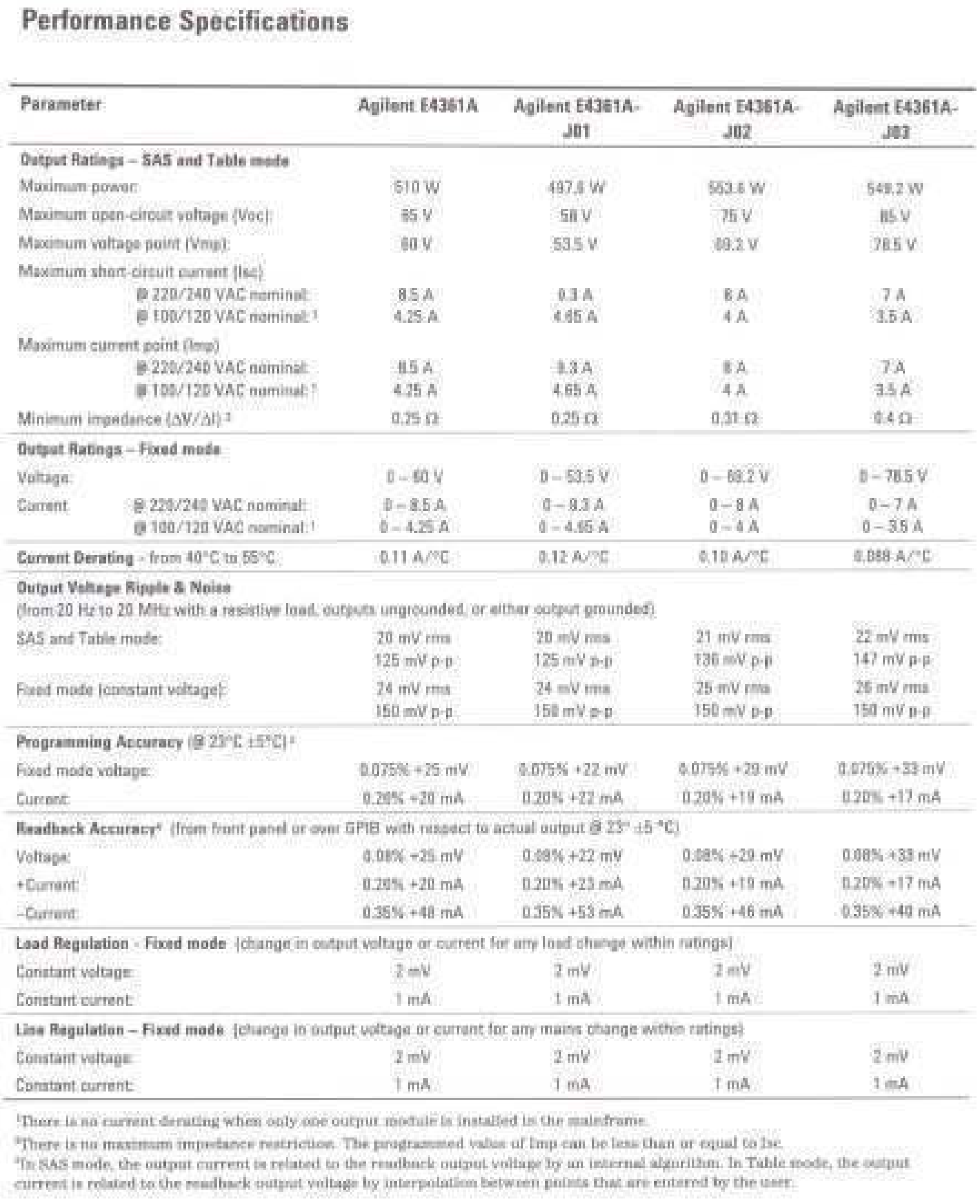

Performance Specifications

Parameter		Agilent E4361A	Agilent E4361A-J01	Agilent E4361A-J02	Agilent E4361A-J03
Output Ratings – SAS and Table mode					
Maximum power:		510 W	497.6 W	553.6 W	549.2 W
Maximum open-circuit voltage (Voc):		65 V	58 V	75 V	85 V
Maximum voltage point (Vmp):		60 V	53.5 V	69.2 V	78.5 V
Maximum short-circuit current (Isc)					
	@ 220/240 VAC nominal:	8.5 A	9.3 A	8 A	7 A
	@ 100/120 VAC nominal: [1]	4.25 A	4.65 A	4 A	3.5 A
Maximum current point (Imp)					
	@ 220/240 VAC nominal:	8.5 A	9.3 A	8 A	7 A
	@ 100/120 VAC nominal: [1]	4.25 A	4.65 A	4 A	3.5 A
Minimum impedance (ΔV/ΔI) [2]		0.25 Ω	0.25 Ω	0.31 Ω	0.4 Ω
Output Ratings – Fixed mode					
Voltage:		0 – 60 V	0 – 53.5 V	0 – 69.2 V	0 – 78.5 V
Current	@ 220/240 VAC nominal:	0 – 8.5 A	0 – 9.3 A	0 – 8 A	0 – 7 A
	@ 100/120 VAC nominal: [1]	0 – 4.25 A	0 – 4.65 A	0 – 4 A	0 – 3.5 A
Current Derating - from 40°C to 55°C		0.11 A/°C	0.12 A/°C	0.10 A/°C	0.088 A/°C
Output Voltage Ripple & Noise (from 20 Hz to 20 MHz with a resistive load, outputs ungrounded, or either output grounded)					
SAS and Table mode:		20 mV rms 125 mV p-p	20 mV rms 125 mV p-p	21 mV rms 136 mV p-p	22 mV rms 147 mV p-p
Fixed mode (constant voltage):		24 mV rms 150 mV p-p	24 mV rms 150 mV p-p	25 mV rms 150 mV p-p	26 mV rms 150 mV p-p
Programming Accuracy (@ 23°C ±5°C) [3]					
Fixed mode voltage:		0.075% +25 mV	0.075% +22 mV	0.075% +29 mV	0.075% +33 mV
Current:		0.20% +20 mA	0.20% +22 mA	0.20% +19 mA	0.20% +17 mA
Readback Accuracy [3] (from front panel or over GPIB with respect to actual output @ 23° ±5 °C)					
Voltage:		0.08% +25 mV	0.08% +22 mV	0.08% +29 mV	0.08% +33 mV
+Current:		0.20% +20 mA	0.20% +23 mA	0.20% +19 mA	0.20% +17 mA
-Current:		0.35% +48 mA	0.35% +53 mA	0.35% +46 mA	0.35% +40 mA
Load Regulation - Fixed mode (change in output voltage or current for any load change within ratings)					
Constant voltage:		2 mV	2 mV	2 mV	2 mV
Constant current:		1 mA	1 mA	1 mA	1 mA
Line Regulation – Fixed mode (change in output voltage or current for any mains change within ratings)					
Constant voltage:		2 mV	2 mV	2 mV	2 mV
Constant current:		1 mA	1 mA	1 mA	1 mA

[1] There is no current derating when only one output module is installed in the mainframe.

[2] There is no maximum impedance restriction. The programmed value of Imp can be less than or equal to Isc.

[3] In SAS mode, the output current is related to the readback output voltage by an internal algorithm. In Table mode, the output current is related to the readback output voltage by interpolation between points that are entered by the user.

Supplemental Characteristics

Parameter	Agilent E4361A	Agilent E4361A-J01	Agilent E4361A-J02	Agilent E4361A-J03
Output Current Ripple & Noise (from 20 Hz to 20 MHz with a resistive load, outputs ungrounded, or either output grounded)				
SAS and Table mode:	4 mA rms 32 mA p-p	4 mA rms 32 mA p-p	4 mA rms 32 mA p-p	4 mA rms 32 mA p-p
Fixed mode (constant current):	2.5 mA rms 19 mA p-p	2.5 mA rms 19 mA p-p	2.5 mA rms 19 mA p-p	2.5 mA rms 19 mA p-p
Output Programming Range (maximum programmable values)				
SAS and Table mode voltage:	0 – 65 V	0 – 58 V	0 – 75 V	0 – 85 V
Fixed mode voltage:	0 – 61.5 V	0 – 54.8 V	0 – 71.0 V	0 – 80.4 V
Output current @ 220/240 VAC nominal:	0 – 8.67A	0 – 9.48 A	0 – 8.18 A	0 – 7.14 A
@ 100/120 VAC nominal:[1]	0 – 4.33 A	0 – 4.75 A	0 – 4.08 A	0 – 3.57 A
Over-voltage protection:	0 – 74 V	0 – 66.7 V	0 – 84.3 V	0 – 94.6 V
Over-current limit:	0 – 10.6 A	0 – 11.6 A	0 – 10.0 A	0 – 8.8 A
Programming Resolution (average values)				
Voltage:	19 mV	17 mV	21 mV	24 mV
Current:	2.7 mA	3.0 mA	2.5 mA	2.2 mA
Over-voltage protection:	325 mV	295 mV	367 mV	409 mV
Over-current limit:	46 mA	52 mA	43 mA	38 mA
Programming Accuracy				
Over-voltage protection:	0.65 V	0.60 V	0.73 V	0.82 V
Over-current limit:	0.5% +215 mA	0.5% +235 mA	0.5% +202 mA	0.5% +177 mA
Current monitor (referenced to P common):	1.0% +130 mA	1.0% +140 mA	1.0% +122 mA	1.0% +107 mA
Fixed Mode Analog Current Programming				
Analog programming:	1.0% +5.5 mA	1.0% +6 mA	1.0% +5.2 mA	1.0% +4.5 mA
+Ip to –Ip Differential Input (0 to full scale):	0 to –4 V	0 to –4 V	0 to –4 V	0 to –4 V
Maximum common mode voltage (referenced to +):	±18 V	±18 V	±18 V	±18 V
Nominal input impedance:	20 kΩ	20 kΩ	20 kΩ	20 kΩ
Drift/Temperature Stability (change in output over 8 hours under constant load, line, and ambient, following a 30-minute warmup)				
Voltage:	0.04% +1 mV	0.04% +0.9 mV	0.04% +1.2 mV	0.04% +1.3 mV
Current:	0.10% +0.85 mA	0.10% +0.93 mA	0.10% +0.8 mA	0.10% +0.7 mA
Temperature Coefficients (output change per °C)				
Voltage:	0.01% +325 µV	0.01% +290 µV	0.01% +375 µV	0.01% +425 µV
Current:	0.025% +215 µA	0.025% +235 µA	0.025% +202 µA	0.025% +177 µA
Output Capacitance				
Capacitance:	< 100 nF	< 100 nF	< 100 nF	< 100 nF
Maximum Reverse Diode Current (with fans running)				
Current:	8.5 A	9.3 A	8.0 A	7.0 A

[1] There is no current derating when only one output module is installed in the mainframe.

Supplemental Characteristics (continued)

Parameter	All E4361A Output Modules
Output Current Settling Time (recovery to within 1.5 A of an operating point on the I-V curve (V < 90% of VMP) after switching from a short circuit to a fixed load)	< 5 µs
Current Monitor Output (IM– with respect to P∇)	0 V to –4 V represents zero to the rated output current
Maximum Capacitive Load for stable operation	
SAS and Table mode:	2000 µF
Fixed mode:	2000 µF
Load Lead Drop with Remote Sensing	
SAS and Table mode:	up to 2 volts + (Voc - Vmp)
Fixed mode:	up to 2 volts total
Current Sinking Capability	
SAS and Table mode:	560 mA
Fixed mode:	440 mA
Voltage Programming Rise/Fall Time (time for output to change from 90% to 10% or 10% to 90% of its total excursion)	< 8 ms
Voltage Programming Settling Time (time for output change to settle within 0.1% of its Fixed mode voltage rating)	25 ms typical
Monotonicity	Output is monotonic over entire rated voltage, current, and temperature range
Auto-Parallel Configuration	Up to 4 outputs
Series and Shunt Switching Frequency (frequency is controlling by a customer-supplied external series or shunt FET connected to the output.)	50 kHz maximum[1]
Output Terminal Isolation (from any terminal to chassis ground - this includes float plus output voltage)	±240 Vdc maximum
Recommended Calibration Interval	1 year

[1] Higher switching frequencies may be possible given the right load conditions consisting of but not necessarily limited to the inductance of the load cable to the shunt switch and the on/off edge rate of the shunt switch.

Figure A.10. E4361A-E4362A output modules and E4360A SAS mainframe specification guide.

A.2 Software development structure

In order to validate the proposed MPPTs and the PV grid connected system, practical implementation is required. Also, the simulation package software is important to test the proposed systems before practical implementation. MATLAB/SIMULINK simulation is used to investigate the proposed control algorithm performance. For graphical user interface and on-line monitoring, the Visual Basic 2008 platform is used.

A.2.1 DSP software

To generate optimized C code for the modulator, the development tool Digital Application Virtual Engineering (DAVE) is used. Another development tool called TASKING (Embedded Development Environment) is used to convert the proposed control algorithm and PWM into ANSI-standard C-code. These development tools can directly access the hardware devices. Appendix B contains the C-codes are used for the practical implementation. A PC is used to write, debug, compile and download the code to the TriCore microprocessor throughout a USB port. The specifications of the used PC are **Core^{TM}2 Duo** microprocessor, and 2 GB RAM. In chapter 3 and 4, PWM is implemented with a switching frequency of 4 kHz. Four local timer cells (LTC) are used to generate one gate signal for the boost converter. The first LTC is configured as a free running timer. The second LTC is configured in the compare mode with an interrupt to determine the carrier or switching period. The other LTCs are used in the compared mode to determine the rising and falling edge of the gate signal during one cycle. Similarly in chapter 5, ten LTCs are applied to generate the four gate signals for the current source inverter.

A.2.2 Simulation analysis program

For the software analysis program, MATLAB® [7.13] and SIMULINK® v7.6 from Mathworks are utilized.

A.2.3 Agilent 14360A System Control Tools

The programming and control of the Agilent E4362A modules PV array simulator can be accomplished by using a powerful software driver called Agilent 14360A System Control Tools. There are three components of the 14360A System Control Tools: the system driver, the configuration wizard, and the server control. Figure A.11 shows the web server of the Agilent E4360A.

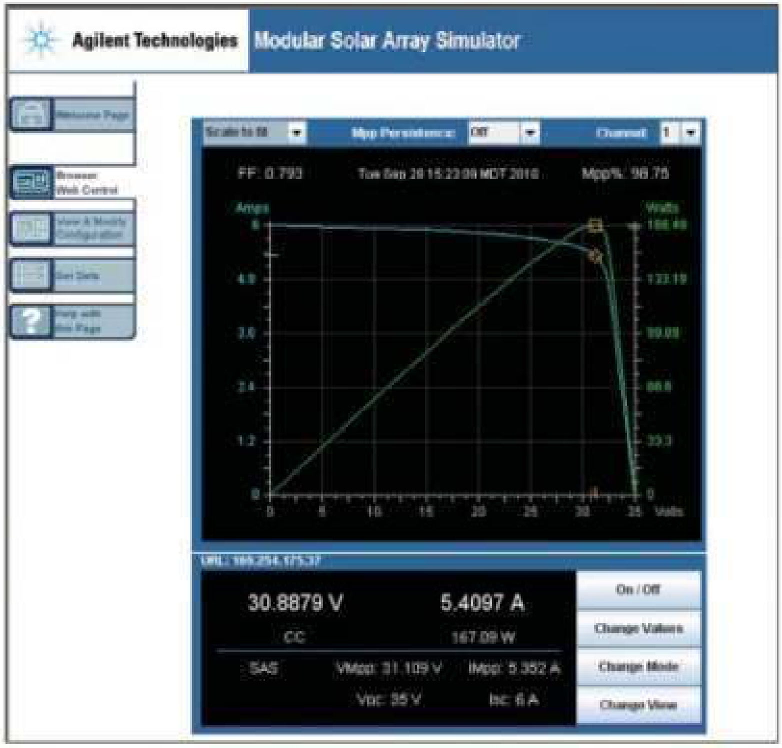

FF: 0.793
Tue Sep 28 15:23:09 MDT 2010
Mpp%: 98.75

30.8879 V
5.4097 A
CC
167.09 W
SAS
VMpp: 31.109 V
IMpp: 5.352 A
Voc: 35 V
Isc: 6 A

Figure A.11. Agilent E4360A built-in web server.

Appendix B

Programs Codes for Different Control Algorithm

B.1 conventional hill climbing maximum power point tracker

```
current_power=Ipv*Vpv;

///////////////////////duty cycle limit/////////////////////////////////
if (duty < 500)
                         {
                                      duty=750;
                         }
if (duty > 2250)
                         {
                                       duty = 2250;
                         }

///////////////////////hill climbing/////////////////////////////////

 if ( previous_power < current_power)
                         {
                                      duty = duty + state*step;
                                      previous_power = current_power;

                         }

else if ( previous_power == current_power)

             else
             {
                                      state=-1*state;
                                      duty = duty + state*step;
                                      previous_power = current_power;
             }
             }

  a=1250-duty/2;
  b=1250+duty/2;
```

B.2 Fuzzy based maximum power point tracker

```
current_power=Ipv*Vpv;

///////////////////////duty cycle limit/////////////////////////////////
if (duty < 500)
{
duty=500;
}
if (duty > 2250)
 {
duty = 2250;
}
     if (j==4)
   {
  j=0;
```

```
 ////////////////////////Fuzzy MPPT//////////////////////////////////
Fuzzy_Practical_U.Delta_P=(current_power-previous_power);
                                        previous_power = current_power;
Fuzzy_Practical_U.Delta_I=(Ipv-Ipv1);
                                       Ipv1=Ipv;
P2_OUT_P11=1;

                                    Fuzzy_Practical_step();
                                    P2_OUT_P11=0;

                                    D=Fuzzy_Practical_Y.Delta_D;
                                    duty=duty+D*150;

                          }
                           j++;



           a=1250-duty/2;
      b=1250+duty/2;
////////////////////////////////////Fuzzy data////////////////////////////////////////
#include "Fuzzy_Practical.h"
#include "Fuzzy_Practical_private.h"

/* Constant parameters (auto storage) */
const ConstParam_Fuzzy_Practical Fuzzy_Practical_ConstP = {
  /* Expression: Xdata
   * '<S3>/x data'
   */
  { -0.008, -0.00784, -0.00768, -0.00752, -0.00736, -0.0072, -0.00704, -0.00688,
    -0.00672, -0.00656, -0.0064, -6.2400000000000008E-003, -0.00608, -0.00592,
    -5.7599999999999995E-003, -5.6000000000000008E-003, -0.00544, -0.00528,
    -5.1199999999999996E-003, -4.9600000000000009E-003, -4.8000000000000004E-003,
    -0.00464, -4.4800000000000005E-003, -0.00432, -4.1600000000000005E-003,
    -0.004, -3.8399999999999997E-003, -0.00368, -3.5199999999999997E-003,
    -0.00336, -3.2000000000000006E-003, -0.00304, -2.8799999999999997E-003,
    -0.00272, -2.5599999999999998E-003, -2.3999999999999994E-003, -0.00224,
    -2.0800000000000003E-003, -1.9200000000000007E-003, -1.7600000000000003E-003,
    -1.5999999999999999E-003, -1.4400000000000003E-003, -1.2799999999999999E-003,
    -1.1199999999999995E-003, -9.6000000000000078E-004, -8.0000000000000036E-004,
    -6.3999999999999994E-004, -4.8000000000000039E-004, -3.1999999999999997E-004,
    -1.6000000000000042E-004, 0.0, 1.6000000000000042E-004,
    3.2000000000000084E-004, 4.7999999999999952E-004, 6.3999999999999994E-004,
    8.0000000000000036E-004, 9.6000000000000078E-004, 1.1199999999999995E-003,
    1.2799999999999999E-003, 1.4400000000000003E-003, 1.5999999999999990E-003,
    1.7599999999999994E-003, 1.9199999999999998E-003, 2.0800000000000003E-003,
    2.2400000000000007E-003, 2.3999999999999994E-003, 2.5599999999999998E-003,
    0.00272, 2.8800000000000006E-003, 3.0400000000000010E-003,
    3.2000000000000015E-003, 3.3600000000000019E-003, 3.5200000000000006E-003,
    3.6799999999999992E-003, 3.8399999999999997E-003, 0.004,
    4.1599999999999988E-003, 4.3199999999999992E-003, 0.00448, 0.00464,
    4.8000000000000004E-003, 4.9600000000000009E-003, 5.1199999999999996E-003,
    0.00528, 0.00544, 5.6000000000000008E-003, 5.7600000000000012E-003,
    5.9200000000000016E-003, 6.0799999999999986E-003, 6.2399999999999990E-003,
    6.3999999999999994E-003, 0.00656, 0.00672, 6.8799999999999990E-003,
    7.0399999999999994E-003, 0.0072, 0.00736, 7.5200000000000006E-003,
    7.6799999999999993E-003, 0.00784, 0.008 },
```

```
 /* Expression: trapmf(linspace(fis.output(1).range(1),fis.output(1).range(2),101),fis.output(1).mf(4).params)
  * '<S23>/PB'
  */
 { 0.0, 0.0, 0.0, 0.0, 0.0, 0.0, 0.0, 0.0, 0.0, 0.0, 0.0, 0.0, 0.0, 0.0, 0.0,
   0.0, 0.0, 0.0, 0.0, 0.0, 0.0, 0.0, 0.0, 0.0, 0.0, 0.0, 0.0, 0.0, 0.0, 0.0,
   0.0, 0.0, 0.0, 0.0, 0.0, 0.0, 0.0, 0.0, 0.0, 0.0, 0.0, 0.0, 0.0, 0.0, 0.0,
   0.0, 0.0, 0.0, 0.0, 0.0, 0.0, 0.0, 0.0, 0.0, 0.0, 0.0, 0.0,
   1.7499999999999885E-001, 0.575, 9.7500000000000098E-001, 1.0, 1.0, 1.0, 1.0,
   1.0, 1.0, 1.0, 1.0, 1.0, 1.0, 1.0, 1.0, 1.0, 1.0, 1.0, 1.0, 1.0, 1.0, 1.0,
   1.0, 1.0, 1.0, 1.0, 1.0, 1.0, 1.0, 1.0, 1.0, 1.0, 1.0, 1.0, 1.0, 1.0, 1.0,
   1.0, 1.0, 1.0, 1.0, 1.0, 1.0, 1.0 },

 /* Expression: trapmf(linspace(fis.output(1).range(1),fis.output(1).range(2),101),fis.output(1).mf(1).params)
  * '<S23>/NB'
  */
 { 1.0, 1.0, 1.0, 1.0, 1.0, 1.0, 1.0, 1.0, 1.0, 1.0, 1.0, 1.0, 1.0, 1.0, 1.0,
   1.0, 1.0, 1.0, 1.0, 1.0, 1.0, 1.0, 1.0, 1.0, 1.0, 1.0, 1.0, 1.0, 1.0, 1.0,
   1.0, 1.0, 1.0, 1.0, 1.0, 1.0, 1.0, 1.0, 1.0, 1.0, 1.0,
   9.7500000000000098E-001, 0.575, 1.7499999999999885E-001, 0.0, 0.0, 0.0, 0.0,
   0.0, 0.0, 0.0, 0.0, 0.0, 0.0, 0.0, 0.0, 0.0, 0.0, 0.0, 0.0, 0.0, 0.0, 0.0,
   0.0, 0.0, 0.0, 0.0, 0.0, 0.0, 0.0, 0.0, 0.0, 0.0, 0.0, 0.0, 0.0, 0.0, 0.0,
   0.0, 0.0, 0.0, 0.0, 0.0, 0.0, 0.0, 0.0, 0.0, 0.0, 0.0, 0.0, 0.0, 0.0, 0.0,
   0.0, 0.0, 0.0, 0.0, 0.0, 0.0, 0.0, 0.0 },

 /* Expression: trimf(linspace(fis.output(1).range(1),fis.output(1).range(2),101),fis.output(1).mf(3).params)
  * '<S23>/PS'
  */
 { 0.0, 0.0, 0.0, 0.0, 0.0, 0.0, 0.0, 0.0, 0.0, 0.0, 0.0, 0.0, 0.0, 0.0, 0.0,
   0.0, 0.0, 0.0, 0.0, 0.0, 0.0, 0.0, 0.0, 0.0, 0.0, 0.0, 0.0, 0.0, 0.0, 0.0,
   0.0, 0.0, 0.0, 0.0, 0.0, 0.0, 0.0, 0.0, 0.0, 0.0, 0.0, 0.0, 0.0, 0.0, 0.0,
   0.0, 0.0, 0.0, 0.0, 0.0, 0.0, 3.2000000000000084E-001,
   6.4000000000000168E-001, 9.5999999999999908E-001, 7.2000000000000008E-001,
   3.9999999999999930E-001, 7.9999999999998475E-002, 0.0, 0.0, 0.0, 0.0, 0.0,
   0.0, 0.0, 0.0, 0.0, 0.0, 0.0, 0.0, 0.0, 0.0, 0.0, 0.0, 0.0, 0.0, 0.0, 0.0,
   0.0, 0.0, 0.0, 0.0, 0.0, 0.0, 0.0, 0.0, 0.0, 0.0, 0.0, 0.0, 0.0, 0.0, 0.0,
   0.0, 0.0, 0.0, 0.0, 0.0, 0.0, 0.0, 0.0, 0.0 },

 /* Expression: trimf(linspace(fis.output(1).range(1),fis.output(1).range(2),101),fis.output(1).mf(2).params)
  * '<S23>/NS'
  */
 { 0.0, 0.0, 0.0, 0.0, 0.0, 0.0, 0.0, 0.0, 0.0, 0.0, 0.0, 0.0, 0.0, 0.0, 0.0,
   0.0, 0.0, 0.0, 0.0, 0.0, 0.0, 0.0, 0.0, 0.0, 0.0, 0.0, 0.0, 0.0, 0.0, 0.0,
   0.0, 0.0, 0.0, 0.0, 0.0, 0.0, 0.0, 0.0, 0.0, 0.0, 0.0, 0.0, 0.0, 0.0,
   7.9999999999998475E-002, 3.9999999999999930E-001, 7.2000000000000008E-001,
   9.6000000000000074E-001, 6.3999999999999990E-001, 3.2000000000000084E-001,
   0.0, 0.0, 0.0, 0.0, 0.0, 0.0, 0.0, 0.0, 0.0, 0.0, 0.0, 0.0, 0.0, 0.0, 0.0,
   0.0, 0.0, 0.0, 0.0, 0.0, 0.0, 0.0, 0.0, 0.0, 0.0, 0.0, 0.0, 0.0, 0.0, 0.0,
   0.0, 0.0, 0.0, 0.0, 0.0, 0.0, 0.0, 0.0, 0.0, 0.0, 0.0, 0.0, 0.0, 0.0, 0.0,
   0.0, 0.0, 0.0, 0.0, 0.0, 0.0 }
};

///////////////////////////////////// Fuzzy logic algorithm //////////////////////////////////////
/* Block signals (auto storage) */
BlockIO_Fuzzy_Practical Fuzzy_Practical_B;

/* External inputs (root inport signals with auto storage) */
ExternalInputs_Fuzzy_Practical Fuzzy_Practical_U;

/* External outputs (root outports fed by signals with auto storage) */
ExternalOutputs_Fuzzy_Practical Fuzzy_Practical_Y;
```

```
/* Real-time model */
RT_MODEL_Fuzzy_Practical Fuzzy_Practical_M_;
RT_MODEL_Fuzzy_Practical *Fuzzy_Practical_M = &Fuzzy_Practical_M_;

/* Output and update for action system:
 *  '<S26>/If Action Subsystem1'
 *  '<S27>/If Action Subsystem1'
 *  '<S28>/If Action Subsystem1'
 *  '<S29>/If Action Subsystem1'
 *  '<S46>/If Action Subsystem1'
 *  '<S47>/If Action Subsystem1'
 *  '<S48>/If Action Subsystem1'
 *  '<S49>/If Action Subsystem1'
 */
void Fuzzy_Practi_IfActionSubsystem1(real_T rtu_x, real_T *rty_0, real_T rtp_a,
  real_T rtp_b)
{
  /* Product: '<S31>/Product ab (trimf)' incorporates:
   *  Constant: '<S31>/a'
   *  Constant: '<S31>/b'
   *  Sum: '<S31>/Sum'
   *  Sum: '<S31>/Sum1'
   */
  (*rty_0) = (rtu_x - rtp_a) / (rtp_b - rtp_a);
}

/* Output and update for action system:
 *  '<S26>/If Action Subsystem3'
 *  '<S27>/If Action Subsystem3'
 *  '<S28>/If Action Subsystem3'
 *  '<S29>/If Action Subsystem3'
 *  '<S46>/If Action Subsystem3'
 *  '<S47>/If Action Subsystem3'
 *  '<S48>/If Action Subsystem3'
 *  '<S49>/If Action Subsystem3'
 */
void Fuzzy_Practi_IfActionSubsystem3(real_T rtu_x, real_T *rty_0, real_T rtp_c,
  real_T rtp_d)
{
  /* Product: '<S33>/Product cd (trimf)' incorporates:
   *  Constant: '<S33>/c'
   *  Constant: '<S33>/d'
   *  Sum: '<S33>/Sum2'
   *  Sum: '<S33>/Sum3'
   */
  (*rty_0) = 1.0 / (rtp_d - rtp_c) * (rtp_d - rtu_x);
}

/* Model step function */
void Fuzzy_Practical_step(void)
{
  {
    real_T min;
    real_T rtb_Weighting;
    real_T min_0[101];
    real_T min_1[101];
    real_T rtb_Weighting_c;
    real_T min_2[101];
    real_T rtb_Weighting_p;
```

```
real_T min_3[101];
real_T rtb_Weighting_p1;
real_T min_4[101];
real_T rtb_Weighting_m;
real_T min_5[101];
real_T rtb_Weighting_l;
real_T min_6[101];
real_T rtb_Weighting_k;
real_T min_7[101];
real_T rtb_Weighting_o;
real_T min_8[101];
real_T rtb_Weighting_n;
real_T min_9[101];
real_T rtb_Weighting_d;
real_T min_a[101];
real_T rtb_Weighting_h;
real_T min_b[101];
real_T rtb_Weighting_d5;
real_T min_c[101];
real_T rtb_Weighting_kf;
real_T rtb_Weighting_b;
real_T rtb_Weighting_i;
real_T rtb_Weighting_a;
real_T rtb_Sum1;
real_T rtb_Sum;
int32_T i;
real_T tmp;
real_T tmp_0;
real_T tmp_1;
real_T tmp_2;

/* If: '<S26>/If' incorporates:
 *  ActionPort: '<S30>/Action Port'
 *  ActionPort: '<S31>/Action Port'
 *  ActionPort: '<S32>/Action Port'
 *  ActionPort: '<S33>/Action Port'
 *  Inport: '<Root>/Delta_P'
 *  SubSystem: '<S26>/If Action Subsystem'
 *  SubSystem: '<S26>/If Action Subsystem1'
 *  SubSystem: '<S26>/If Action Subsystem2'
 *  SubSystem: '<S26>/If Action Subsystem3'
 */
if (Fuzzy_Practical_U.Delta_P > -0.5) {
  /* Constant: '<S30>/0' */
  Fuzzy_Practical_B.Merge = 0.0;
} else if ((Fuzzy_Practical_U.Delta_P >= (rtMinusInf)) &&
           (Fuzzy_Practical_U.Delta_P <= -3.0)) {
  /* Constant: '<S32>/0' */
  Fuzzy_Practical_B.Merge = 1.0;
} else {
  Fuzzy_Practi_IfActionSubsystem3(Fuzzy_Practical_U.Delta_P,
    &Fuzzy_Practical_B.Merge, -3.0, -0.5);
}

/* If: '<S46>/If' incorporates:
 *  ActionPort: '<S50>/Action Port'
 *  ActionPort: '<S51>/Action Port'
 *  ActionPort: '<S52>/Action Port'
 *  ActionPort: '<S53>/Action Port'
 *  Inport: '<Root>/Delta_I'
```

```
 *  SubSystem: '<S46>/If Action Subsystem'
 *  SubSystem: '<S46>/If Action Subsystem1'
 *  SubSystem: '<S46>/If Action Subsystem2'
 *  SubSystem: '<S46>/If Action Subsystem3'
 */
if (Fuzzy_Practical_U.Delta_I > -0.002) {
  /* Constant: '<S50>/0' */
  Fuzzy_Practical_B.Merge_d = 0.0;
} else if ((Fuzzy_Practical_U.Delta_I >= (rtMinusInf)) &&
           (Fuzzy_Practical_U.Delta_I <= -0.007)) {
  /* Constant: '<S52>/0' */
  Fuzzy_Practical_B.Merge_d = 1.0;
} else {
  Fuzzy_Practi_IfActionSubsystem3(Fuzzy_Practical_U.Delta_I,
    &Fuzzy_Practical_B.Merge_d, -0.007, -0.002);
}

/* MinMax: '<S4>/andorMethod' */
min = rt_MINd_snf(Fuzzy_Practical_B.Merge, Fuzzy_Practical_B.Merge_d);

/* Product: '<S4>/Weighting' incorporates:
 *  Constant: '<S4>/Weight'
 */
rtb_Weighting = min;

/* MinMax: '<S4>/impMethod' incorporates:
 *  Constant: '<S23>/PB'
 */
for (i = 0; i < 101; i++) {
  min_1[i] = rt_MINd_snf(min, Fuzzy_Practical_ConstP.PB_Value[i]);
}

/* If: '<S47>/If' incorporates:
 *  ActionPort: '<S54>/Action Port'
 *  ActionPort: '<S55>/Action Port'
 *  ActionPort: '<S56>/Action Port'
 *  ActionPort: '<S57>/Action Port'
 *  Inport: '<Root>/Delta_I'
 *  SubSystem: '<S47>/If Action Subsystem'
 *  SubSystem: '<S47>/If Action Subsystem1'
 *  SubSystem: '<S47>/If Action Subsystem2'
 *  SubSystem: '<S47>/If Action Subsystem3'
 */
if ((Fuzzy_Practical_U.Delta_I < -0.00665) || (Fuzzy_Practical_U.Delta_I >
     0.0)) {
  /* Constant: '<S54>/0' */
  Fuzzy_Practical_B.Merge_k = 0.0;
} else if ((Fuzzy_Practical_U.Delta_I >= -0.002) &&
           (Fuzzy_Practical_U.Delta_I <= 0.0)) {
  /* Constant: '<S56>/0' */
  Fuzzy_Practical_B.Merge_k = 1.0;
} else if (Fuzzy_Practical_U.Delta_I < -0.002) {
  Fuzzy_Practi_IfActionSubsystem1(Fuzzy_Practical_U.Delta_I,
    &Fuzzy_Practical_B.Merge_k, -0.00665, -0.002);
} else {
  Fuzzy_Practi_IfActionSubsystem3(Fuzzy_Practical_U.Delta_I,
    &Fuzzy_Practical_B.Merge_k, 0.0, 0.0);
}

/* MinMax: '<S13>/andorMethod' */
```

```
min = rt_MINd_snf(Fuzzy_Practical_B.Merge, Fuzzy_Practical_B.Merge_k);

/* Product: '<S13>/Weighting' incorporates:
 *  Constant: '<S13>/Weight'
 */
rtb_Weighting_c = min;

/* MinMax: '<S13>/impMethod' incorporates:
 *  Constant: '<S23>/PB'
 */
for (i = 0; i < 101; i++) {
  min_2[i] = rt_MINd_snf(min, Fuzzy_Practical_ConstP.PB_Value[i]);
}

/* If: '<S49>/If' incorporates:
 *  ActionPort: '<S62>/Action Port'
 *  ActionPort: '<S63>/Action Port'
 *  ActionPort: '<S64>/Action Port'
 *  ActionPort: '<S65>/Action Port'
 *  Inport: '<Root>/Delta_I'
 *  SubSystem: '<S49>/If Action Subsystem'
 *  SubSystem: '<S49>/If Action Subsystem1'
 *  SubSystem: '<S49>/If Action Subsystem2'
 *  SubSystem: '<S49>/If Action Subsystem3'
 */
if ((Fuzzy_Practical_U.Delta_I < 0.0) || (Fuzzy_Practical_U.Delta_I >
     0.00665)) {
  /* Constant: '<S62>/0' */
  Fuzzy_Practical_B.Merge_o = 0.0;
} else if ((Fuzzy_Practical_U.Delta_I >= 0.0) && (Fuzzy_Practical_U.Delta_I <=
            0.002)) {
  /* Constant: '<S64>/0' */
  Fuzzy_Practical_B.Merge_o = 1.0;
} else if (Fuzzy_Practical_U.Delta_I < 0.0) {
  Fuzzy_Practi_IfActionSubsystem1(Fuzzy_Practical_U.Delta_I,
    &Fuzzy_Practical_B.Merge_o, 0.0, 0.0);
} else {
  Fuzzy_Practi_IfActionSubsystem3(Fuzzy_Practical_U.Delta_I,
    &Fuzzy_Practical_B.Merge_o, 0.002, 0.00665);
}

/* MinMax: '<S14>/andorMethod' */
min = rt_MINd_snf(Fuzzy_Practical_B.Merge, Fuzzy_Practical_B.Merge_o);

/* Product: '<S14>/Weighting' incorporates:
 *  Constant: '<S14>/Weight'
 */
rtb_Weighting_p = min;

/* MinMax: '<S14>/impMethod' incorporates:
 *  Constant: '<S23>/NB'
 */
for (i = 0; i < 101; i++) {
  min_3[i] = rt_MINd_snf(min, Fuzzy_Practical_ConstP.NB_Value[i]);
}

/* If: '<S48>/If' incorporates:
 *  ActionPort: '<S58>/Action Port'
 *  ActionPort: '<S59>/Action Port'
 *  ActionPort: '<S60>/Action Port'
```

```
 *  ActionPort: '<S61>/Action Port'
 *  Inport: '<Root>/Delta_I'
 *  SubSystem: '<S48>/If Action Subsystem'
 *  SubSystem: '<S48>/If Action Subsystem1'
 *  SubSystem: '<S48>/If Action Subsystem2'
 *  SubSystem: '<S48>/If Action Subsystem3'
 */
if (Fuzzy_Practical_U.Delta_I < 0.002) {
  /* Constant: '<S58>/0' */
  Fuzzy_Practical_B.Merge_g = 0.0;
} else if ((Fuzzy_Practical_U.Delta_I >= 0.007) &&
           (Fuzzy_Practical_U.Delta_I <= (rtInf))) {
  /* Constant: '<S60>/0' */
  Fuzzy_Practical_B.Merge_g = 1.0;
} else if (Fuzzy_Practical_U.Delta_I < 0.007) {
  Fuzzy_Practi_IfActionSubsystem1(Fuzzy_Practical_U.Delta_I,
    &Fuzzy_Practical_B.Merge_g, 0.002, 0.007);
} else {
  Fuzzy_Practi_IfActionSubsystem3(Fuzzy_Practical_U.Delta_I,
    &Fuzzy_Practical_B.Merge_g, rtInf, rtInf);
}

/* MinMax: '<S15>/andorMethod' */
min = rt_MINd_snf(Fuzzy_Practical_B.Merge, Fuzzy_Practical_B.Merge_g);

/* Product: '<S15>/Weighting' incorporates:
 *  Constant: '<S15>/Weight'
 */
rtb_Weighting_p1 = min;

/* MinMax: '<S15>/impMethod' incorporates:
 *  Constant: '<S23>/NB'
 */
for (i = 0; i < 101; i++) {
  min_4[i] = rt_MINd_snf(min, Fuzzy_Practical_ConstP.NB_Value[i]);
}

/* If: '<S27>/If' incorporates:
 *  ActionPort: '<S34>/Action Port'
 *  ActionPort: '<S35>/Action Port'
 *  ActionPort: '<S36>/Action Port'
 *  ActionPort: '<S37>/Action Port'
 *  Inport: '<Root>/Delta_P'
 *  SubSystem: '<S27>/If Action Subsystem'
 *  SubSystem: '<S27>/If Action Subsystem1'
 *  SubSystem: '<S27>/If Action Subsystem2'
 *  SubSystem: '<S27>/If Action Subsystem3'
 */
if ((Fuzzy_Practical_U.Delta_P < -3.0) || (Fuzzy_Practical_U.Delta_P > 0.0))
{
  /* Constant: '<S34>/0' */
  Fuzzy_Practical_B.Merge_de = 0.0;
} else if ((Fuzzy_Practical_U.Delta_P >= -0.5) && (Fuzzy_Practical_U.Delta_P
           <= 0.0)) {
  /* Constant: '<S36>/0' */
  Fuzzy_Practical_B.Merge_de = 1.0;
} else if (Fuzzy_Practical_U.Delta_P < -0.5) {
  Fuzzy_Practi_IfActionSubsystem1(Fuzzy_Practical_U.Delta_P,
    &Fuzzy_Practical_B.Merge_de, -3.0, -0.5);
} else {
```

```
  Fuzzy_Practi_IfActionSubsystem3(Fuzzy_Practical_U.Delta_P,
    &Fuzzy_Practical_B.Merge_de, 0.0, 0.0);
}

/* Product: '<S16>/Weighting' incorporates:
 *  Constant: '<S16>/Weight'
 *  MinMax: '<S16>/andorMethod'
 */
rtb_Weighting_m = rt_MINd_snf(Fuzzy_Practical_B.Merge_de,
  Fuzzy_Practical_B.Merge_d);

/* Product: '<S17>/Weighting' incorporates:
 *  Constant: '<S17>/Weight'
 *  MinMax: '<S17>/andorMethod'
 */
rtb_Weighting_l = rt_MINd_snf(Fuzzy_Practical_B.Merge_de,
  Fuzzy_Practical_B.Merge_k);

/* Product: '<S18>/Weighting' incorporates:
 *  Constant: '<S18>/Weight'
 *  MinMax: '<S18>/andorMethod'
 */
rtb_Weighting_k = rt_MINd_snf(Fuzzy_Practical_B.Merge_de,
  Fuzzy_Practical_B.Merge_o);

/* MinMax: '<S19>/andorMethod' */
min = rt_MINd_snf(Fuzzy_Practical_B.Merge_de, Fuzzy_Practical_B.Merge_g);

/* Product: '<S19>/Weighting' incorporates:
 *  Constant: '<S19>/Weight'
 */
rtb_Weighting_o = min;

/* MinMax: '<S19>/impMethod' incorporates:
 *  Constant: '<S23>/NS'
 *  Constant: '<S23>/PS'
 *  MinMax: '<S16>/impMethod'
 *  MinMax: '<S17>/impMethod'
 *  MinMax: '<S18>/impMethod'
 */
for (i = 0; i < 101; i++) {
  min_5[i] = rt_MINd_snf(rtb_Weighting_m, Fuzzy_Practical_ConstP.PS_Value[i]);
  min_6[i] = rt_MINd_snf(rtb_Weighting_l, Fuzzy_Practical_ConstP.PS_Value[i]);
  min_7[i] = rt_MINd_snf(rtb_Weighting_k, Fuzzy_Practical_ConstP.NS_Value[i]);
  min_8[i] = rt_MINd_snf(min, Fuzzy_Practical_ConstP.NS_Value[i]);
}

/* If: '<S29>/If' incorporates:
 *  ActionPort: '<S42>/Action Port'
 *  ActionPort: '<S43>/Action Port'
 *  ActionPort: '<S44>/Action Port'
 *  ActionPort: '<S45>/Action Port'
 *  Inport: '<Root>/Delta_P'
 *  SubSystem: '<S29>/If Action Subsystem'
 *  SubSystem: '<S29>/If Action Subsystem1'
 *  SubSystem: '<S29>/If Action Subsystem2'
 *  SubSystem: '<S29>/If Action Subsystem3'
 */
if ((Fuzzy_Practical_U.Delta_P < 0.0) || (Fuzzy_Practical_U.Delta_P > 3.0))
{
```

```
  /* Constant: '<S42>/0' */
  Fuzzy_Practical_B.Merge_o1 = 0.0;
} else if ((Fuzzy_Practical_U.Delta_P >= 0.0) && (Fuzzy_Practical_U.Delta_P <=
           0.5)) {
  /* Constant: '<S44>/0' */
  Fuzzy_Practical_B.Merge_o1 = 1.0;
} else if (Fuzzy_Practical_U.Delta_P < 0.0) {
  Fuzzy_Practi_IfActionSubsystem1(Fuzzy_Practical_U.Delta_P,
    &Fuzzy_Practical_B.Merge_o1, 0.0, 0.0);
} else {
  Fuzzy_Practi_IfActionSubsystem3(Fuzzy_Practical_U.Delta_P,
    &Fuzzy_Practical_B.Merge_o1, 0.5, 3.0);
}

/* Product: '<S20>/Weighting' incorporates:
 *  Constant: '<S20>/Weight'
 *  MinMax: '<S20>/andorMethod'
 */
rtb_Weighting_n = rt_MINd_snf(Fuzzy_Practical_B.Merge_o1,
  Fuzzy_Practical_B.Merge_d);

/* Product: '<S5>/Weighting' incorporates:
 *  Constant: '<S5>/Weight'
 *  MinMax: '<S5>/andorMethod'
 */
rtb_Weighting_d = rt_MINd_snf(Fuzzy_Practical_B.Merge_o1,
  Fuzzy_Practical_B.Merge_k);

/* Product: '<S6>/Weighting' incorporates:
 *  Constant: '<S6>/Weight'
 *  MinMax: '<S6>/andorMethod'
 */
rtb_Weighting_h = rt_MINd_snf(Fuzzy_Practical_B.Merge_o1,
  Fuzzy_Practical_B.Merge_o);

/* MinMax: '<S7>/andorMethod' */
min = rt_MINd_snf(Fuzzy_Practical_B.Merge_o1, Fuzzy_Practical_B.Merge_g);

/* Product: '<S7>/Weighting' incorporates:
 *  Constant: '<S7>/Weight'
 */
rtb_Weighting_d5 = min;

/* MinMax: '<S7>/impMethod' incorporates:
 *  Constant: '<S23>/NB'
 *  Constant: '<S23>/NS'
 *  Constant: '<S23>/PS'
 *  MinMax: '<S20>/impMethod'
 *  MinMax: '<S5>/impMethod'
 *  MinMax: '<S6>/impMethod'
 */
for (i = 0; i < 101; i++) {
  min_9[i] = rt_MINd_snf(rtb_Weighting_n, Fuzzy_Practical_ConstP.NB_Value[i]);
  min_a[i] = rt_MINd_snf(rtb_Weighting_d, Fuzzy_Practical_ConstP.NS_Value[i]);
  min_b[i] = rt_MINd_snf(rtb_Weighting_h, Fuzzy_Practical_ConstP.PS_Value[i]);
  min_c[i] = rt_MINd_snf(min, Fuzzy_Practical_ConstP.PS_Value[i]);
}

/* If: '<S28>/If' incorporates:
 *  ActionPort: '<S38>/Action Port'
```

```
 *  ActionPort: '<S39>/Action Port'
 *  ActionPort: '<S40>/Action Port'
 *  ActionPort: '<S41>/Action Port'
 *  Inport: '<Root>/Delta_P'
 *  SubSystem: '<S28>/If Action Subsystem'
 *  SubSystem: '<S28>/If Action Subsystem1'
 *  SubSystem: '<S28>/If Action Subsystem2'
 *  SubSystem: '<S28>/If Action Subsystem3'
 */
if (Fuzzy_Practical_U.Delta_P < 0.5) {
  /* Constant: '<S38>/0' */
  Fuzzy_Practical_B.Merge_e = 0.0;
} else if ((Fuzzy_Practical_U.Delta_P >= 3.0) && (Fuzzy_Practical_U.Delta_P <=
           (rtInf))) {
  /* Constant: '<S40>/0' */
  Fuzzy_Practical_B.Merge_e = 1.0;
} else if (Fuzzy_Practical_U.Delta_P < 3.0) {
  Fuzzy_Practi_IfActionSubsystem1(Fuzzy_Practical_U.Delta_P,
    &Fuzzy_Practical_B.Merge_e, 0.5, 3.0);
} else {
  Fuzzy_Practi_IfActionSubsystem3(Fuzzy_Practical_U.Delta_P,
    &Fuzzy_Practical_B.Merge_e, rtInf, rtInf);
}

/* Product: '<S8>/Weighting' incorporates:
 *  Constant: '<S8>/Weight'
 *  MinMax: '<S8>/andorMethod'
 */
rtb_Weighting_kf = rt_MINd_snf(Fuzzy_Practical_B.Merge_e,
  Fuzzy_Practical_B.Merge_d);

/* Product: '<S9>/Weighting' incorporates:
 *  Constant: '<S9>/Weight'
 *  MinMax: '<S9>/andorMethod'
 */
rtb_Weighting_b = rt_MINd_snf(Fuzzy_Practical_B.Merge_e,
  Fuzzy_Practical_B.Merge_k);

/* Product: '<S10>/Weighting' incorporates:
 *  Constant: '<S10>/Weight'
 *  MinMax: '<S10>/andorMethod'
 */
rtb_Weighting_i = rt_MINd_snf(Fuzzy_Practical_B.Merge_e,
  Fuzzy_Practical_B.Merge_o);

/* Product: '<S11>/Weighting' incorporates:
 *  Constant: '<S11>/Weight'
 *  MinMax: '<S11>/andorMethod'
 */
rtb_Weighting_a = rt_MINd_snf(Fuzzy_Practical_B.Merge_e,
  Fuzzy_Practical_B.Merge_g);

/* MinMax: '<S12>/andorMethod' */
min = rt_MINd_snf(Fuzzy_Practical_B.Merge_e, Fuzzy_Practical_B.Merge_g);

/* MinMax: '<S2>/AggMethod1' incorporates:
 *  Constant: '<S23>/NB'
 *  Constant: '<S23>/PB'
 *  MinMax: '<S10>/impMethod'
 *  MinMax: '<S11>/impMethod'
```

```
 *  MinMax: '<S12>/impMethod'
 *  MinMax: '<S8>/impMethod'
 *  MinMax: '<S9>/impMethod'
 */
for (i = 0; i < 101; i++) {
  rtb_Sum = rt_MINd_snf(rtb_Weighting_kf, Fuzzy_Practical_ConstP.NB_Value[i]);
  rtb_Sum1 = rt_MINd_snf(rtb_Weighting_b, Fuzzy_Practical_ConstP.NB_Value[i]);
  tmp_2 = rt_MINd_snf(rtb_Weighting_i, Fuzzy_Practical_ConstP.PB_Value[i]);
  tmp_1 = rt_MINd_snf(rtb_Weighting_a, Fuzzy_Practical_ConstP.PB_Value[i]);
  tmp_0 = rt_MINd_snf(min, Fuzzy_Practical_ConstP.NB_Value[i]);
  tmp = rt_MAXd_snf(min_1[i], min_2[i]);
  tmp = rt_MAXd_snf(tmp, min_3[i]);
  tmp = rt_MAXd_snf(tmp, min_4[i]);
  tmp = rt_MAXd_snf(tmp, min_5[i]);
  tmp = rt_MAXd_snf(tmp, min_6[i]);
  tmp = rt_MAXd_snf(tmp, min_7[i]);
  tmp = rt_MAXd_snf(tmp, min_8[i]);
  tmp = rt_MAXd_snf(tmp, min_9[i]);
  tmp = rt_MAXd_snf(tmp, min_a[i]);
  tmp = rt_MAXd_snf(tmp, min_b[i]);
  tmp = rt_MAXd_snf(tmp, min_c[i]);
  tmp = rt_MAXd_snf(tmp, rtb_Sum);
  tmp = rt_MAXd_snf(tmp, rtb_Sum1);
  tmp = rt_MAXd_snf(tmp, tmp_2);
  tmp = rt_MAXd_snf(tmp, tmp_1);
  tmp = rt_MAXd_snf(tmp, tmp_0);
  min_0[i] = tmp;
}

/* Sum: '<S3>/Sum1' */
rtb_Sum1 = min_0[0];
for (i = 0; i < 100; i++) {
  rtb_Sum1 += min_0[i + 1];
}

/* If: '<S3>/If' incorporates:
 *  ActionPort: '<S24>/Action Port'
 *  ActionPort: '<S25>/Action Port'
 *  SubSystem: '<S3>/Action: One'
 *  SubSystem: '<S3>/Action: u1'
 */
if (rtb_Sum1 < 0.0) {
  /* Constant: '<S24>/One' */
  rtb_Sum1 = 1.0;
}

/* Switch: '<S2>/Switch' incorporates:
 *  Constant: '<S2>/MidRange'
 *  Constant: '<S2>/Zero'
 *  Product: '<S3>/Averaging (COA)'
 *  RelationalOperator: '<S2>/Zero Firing Strength?'
 *  Sum: '<S2>/Total Firing Strength'
 */
if ((((((((((((((((rtb_Weighting + rtb_Weighting_c) + rtb_Weighting_p) +
                rtb_Weighting_p1) + rtb_Weighting_m) + rtb_Weighting_l) +
              rtb_Weighting_k) + rtb_Weighting_o) + rtb_Weighting_n) +
            rtb_Weighting_d) + rtb_Weighting_h) + rtb_Weighting_d5) +
          rtb_Weighting_kf) + rtb_Weighting_b) + rtb_Weighting_i) +
        rtb_Weighting_a) + min > 0.0) >= 1) {
  /* Product: '<S3>/Product (COA)' incorporates:
```

```
       *  Constant: '<S3>/x data'
       */
      for (i = 0; i < 101; i++) {
        min_0[i] *= Fuzzy_Practical_ConstP.xdata_Value[i];
      }

      /* Sum: '<S3>/Sum' */
      rtb_Sum = min_0[0];
      for (i = 0; i < 100; i++) {
        rtb_Sum += min_0[i + 1];
      }

      min = rtb_Sum / rtb_Sum1;
    } else {
      min = 0.0;
    }

    /* Outport: '<Root>/Delta_D' */
    Fuzzy_Practical_Y.Delta_D = min;
  }
}

/* Model initialize function */
void Fuzzy_Practical_initialize(boolean_T firstTime)
{
  (void)firstTime;

  /* Registration code */

  /* initialize non-finites */
  rt_InitInfAndNaN(sizeof(real_T));
}
```

B.3 Fuzzy based maximum power point tracker for partial shadowing condition

```
current_power=Ipv*Vpv;

///////////////////////Store power/////////////////////////////////
if(current_power>P)
{
 PP=current_power;
 P=PP;
}
else
{
  PP=P;
}

////////////////////// scanning and tracking ////////////////////////////////
if (Time<=100)
        {

                                                duty=JJ;
                              JJ=JJ+20;
        }
else
{
```

```
 Fuzzy_Practical_U.Delta_P=(current_power-previous_power);
                                             previous_power = current_power;
 Fuzzy_Practical_U.Delta_I=(Ipv-Ipv1);
                                            Ipv1=Ipv;
 P2_OUT_P11=1;

                                       Fuzzy_Practical_step();
                                       P2_OUT_P11=0;

                                       D=Fuzzy_Practical_Y.Delta_D;
                                       duty=duty+D*150;

                          }
                           j++;
       a=1250-duty/2;
       b=1250+duty/2;
```

B.4 Grid connected current source inverter

```
////////////////////////////////PLL//////////////////////////////////////////
                          Vpll0=Vac1;
                           if(Vpll0>=0 && Vpll<0)
                           {
                           alfa=0;
                            }
                            else
                            {
                          alfa=alfa+360*50*0.00025;
                          }
                          if (alfa>=360)
                          {
                          alfa=alfa-360;
                          }
                          Vpll=Vpll0;
                yy=(1*sin(alfa*2*asin(1)/180));
//////////////////////////////////////////////////////////////////////////////
                          ID=Idc-1;
                          Kp=0.02;
                          Kii=10;//0.1;
                          ff=0.00025;;//0.0002442002442;
                          if (Ki<Kii)
                          {
                          Ki=Ki+(Kii)/(4000*5);
                          }
                          else
                          {
                          Ki=Kii;
                          }
                          Im=Imo+(ff/2)*(IDo+ID)*Ki;
                          Imo=Im;
                          IDo=ID;
                          B= (Im+Kp*ID);
                          if (B>=6)
                          {
                          B=6;
                          }
                          else if (B<=0)
                          {
```

```
B=0;
}
else
{
B=(Im+Kp*ID);
}
BB=B*yy;
ID1=(Iac/10)-BB;
Kp1=10;
Ki1=15;
a=3;
Wo=Wi+ff*(2*2*asin(1)*a*50)*(2*2*asin(1)*a*50)*Zi;
Zo=Zi+ff*(ID1*Ki1-Wo);
Wi=Wo;
Zi=Zo;
BB1=-(Kp1*ID1+Zo)+(Vac1/155.56);
ID2=(Vac2/155.56)-BB1;
Kp2=0.05;
Ki2=0;
Wo1=Wi1+ff*(2*2*asin(1)*a*50)*(2*2*asin(1)*a*50)*Zi1;
Zo1=Zi1+ff*(ID2*Ki2-Wo1);
Wi1=Wo1;
Zi1=Zo1;
BB2=-(Kp2*ID2+Zo1)+(Iac/10);
if (BB2>=1)
{
BB2=1;
}
else if (BB2<=-1)
{
BB2=-1;
}
else
{
BB2=BB2;
}
y=BB2;

/////////////////////////////CPWM/////////////////////////////
Toff=(1-y)/2*Ts;
Ton=(1+y)/2*Ts;
T2r=(Ts-Ton)/2;
T2f=(Ts+Ton)/2;
T3f=(Ts-Toff)/2;
T3r=(Ts+Toff)/2;
///////////////////////////////////////////////////////////////////
```

Appendix C

Digital implementation of the proposed carrier based pulse width modulation for a single-phase current source inverter

This appendix presents a brief description of the real time implementation of the proposed carrier based pulse width modulation (CPWM), including its formulation. The proposed CPWM uses two carriers shifted 180 from each other and one modulating signal (y). Figure C.1 depicts the carrier waveforms and target modulating signal within one switching cycle, T_s. It has been assumed that the carrier frequency is much higher than the fundamental frequency; hence a linear approximation of the fundamental signal within each switching cycle is valid. The solid straight line carrier shown in Figure C.1 is used to generate the gating signals for the upper switches, while the carrier designated by the dashed line is responsible for generating the gating signals for the lower switches. A single-phase current source inverter shown in figure C.2 is used to aid illustration. In the proposed modulation techniques, switches (S_1, S_2) and (S3, S4) are complementary pairs. Turning S_1 precludes S_2 from being turning on, and the same applicable to the lower switches. The proposed modulation strategy operates a single-phase current source inverter in a similar manner to a voltage source inverter in the sense that the on and off states of the inverter switches is determine by comparison of the reference modulating signal and carrier signals. For instance, when the modulating signal is greater than the solid red carrier, upper switch S_2 must be turned on, and that implies S_1 must be off. Assuming T_{r2} and T_{r3} are rising times for switches S_2 and S_3, and T_{f2} and T_{f3} are falling times for switches S_2 and S_3, these times can be calculated in real time by using the following equations:

The dwelling time for switch S3 is calculated using proportionality, from:

$$\frac{2T_{off}}{T_s} = \frac{y}{1} \tag{C.1}$$

Rearranged as:

$$T_{off} = y\frac{T_s}{2} \tag{C.2}$$

T_{r3} is computed from

$$T_{r3} = \tfrac{1}{2}\left[\tfrac{1}{2}T_s - T_{off}\right] \tag{C.3}$$

Substituting (C.2) into (C.3), the following expressions are obtained:

$$T_{r3} = \tfrac{1}{4}T_s\left[1 - y\right] \tag{C.4}$$

$$T_{f3} = \tfrac{1}{4}T_s\left[1 + y\right] \tag{C.5}$$

similarly the expressions used to determine the rising and falling times of the switch s2 are obtained, below:

$$T_{r2} = \tfrac{1}{4}T_s\left[3 - y\right] \tag{C.6}$$

$$T_{f2} = \tfrac{1}{4}T_s\left[3 + y\right] \tag{C.7}$$

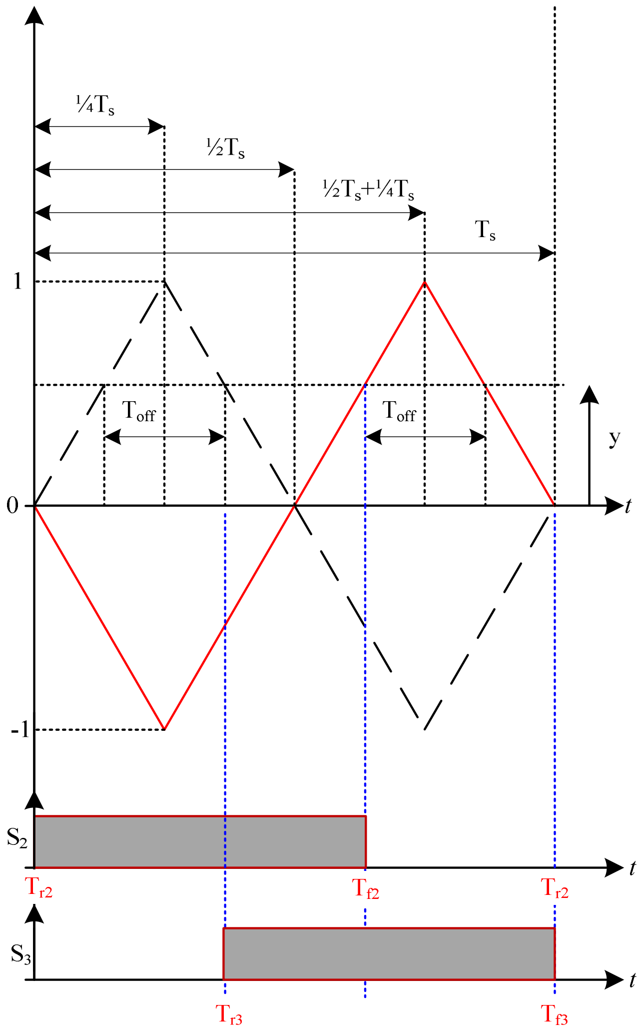

Figure C.1. The proposed carrier based PWM.

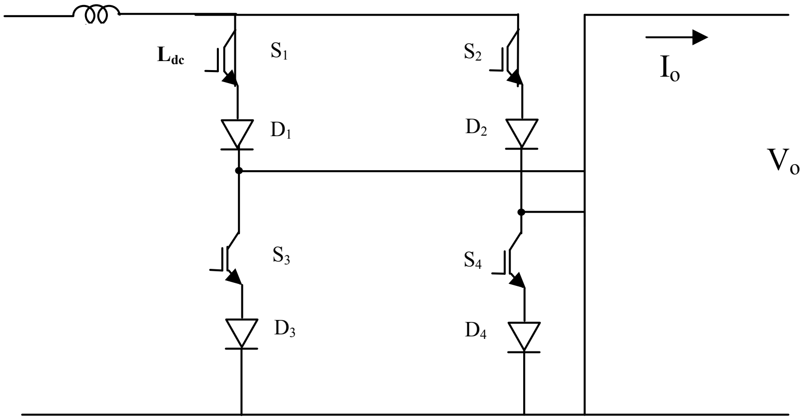

Figure C.1. Single phase current source inverter.

Appendix D

List of Tables and Figures

List of Figures

Chapter 1: Introduction

Chapter 2: Photovoltaic system configuration

Chapter 3: A Modified Hill-Climbing Method for Maximum Power Point Tracking in Standalone Photovoltaic Systems

Chapter 4: A Maximum Power Point Tracking Technique for Partially Shaded Photovoltaic Systems

Chapter 5: Single-Phase Single-Stage Transformerless Grid Connected PV System

List of Tables

Chapter 1: Introduction

Chapter 3: A Modified Hill-Climbing Method for Maximum Power Point Tracking in Standalone Photovoltaic Systems

Chapter 4: A Maximum Power Point Tracking Technique for Partially Shaded Photovoltaic Systems

Chapter 5: Single-Phase Single-Stage Transformerless Grid Connected PV System

Appendix E

Summary of relevant published work by the author

[1] B. N. Alajmi, K. H. Ahmed, S. J. Finney, and B. W. Williams, "Fuzzy-Logic Control Approach of a Modified Hill-Climbing Method for Maximum Power Point in Microgrid Standalone Photovoltaic System,"
Power Electronics, IEEE Transactions on, vol. 26, pp. 1022-1030, 2011.

Abstract- A new fuzzy-logic controller for maximum power point tracking of photovoltaic (PV) systems is proposed. PV modeling is discussed. Conventional hill-climbing maximum power-point tracker structures and features are investigated. The new controller improves the hill-climbing search method by fuzzifying the rules of such techniques and eliminates their drawbacks. Fuzzy-logic-based hill climbing offers fast and accurate converging to the maximum operating point during steady-state and varying weather conditions compared to conventional hill climbing. Simulation and experimentation results are provided to demonstrate the validity of the proposed fuzzy-logic-based controller.

[2] B. N. Alajmi, K. H. Ahmed, S. J. Finney, and B. W. Williams, "A Maximum Power Point Tracking Technique for Partially Shaded Photovoltaic Systems in Microgrids,"
Industrial Electronics, IEEE Transactions on, vol. 60, pp. 1596-1606, 2013.

Abstract- A modified fuzzy-logic controller for maximum power point (MPP) tracking is proposed to increase photovoltaic (PV) system performance during partially shaded conditions. Instead of perturbing and observing the PV system MPP, the controller scans and stores the maximum power during the perturbing and observing procedures. The controller offers accurate convergence to the global maximum operating point under different partial shadowing conditions. A mathematical model of the PV system under partial shadowing conditions is derived. To validate the proposed modified fuzzy-logic-based controller, simulation and experimentation results are provided.

[3] B. N. Alajmi, K. H. Ahmed, G. P. Adam, and B. W. Williams, "Single-Phase Single-Stage Transformer less Grid-Connected PV System," Power Electronics, IEEE Transactions on, vol. 28, pp. 2664-2676, 2013.

Abstract- A single-phase, single-stage current source inverter based photovoltaic system for grid connection is proposed. The system utilizes transformer-less single-stage conversion for tracking the maximum power point and interfacing the photovoltaic arrays to the grid. The maximum power point is maintained with a fuzzy logic controller. A proportional-resonant controller is used to control the current injected into the grid. To improve the power quality and system efficiency, a double tuned parallel resonant circuit is proposed to attenuate the second and fourth order harmonics at the inverter dc side. A modified carrier based modulation technique for the current source inverter is proposed to magnetize the dc link inductor by shorting one of the bridge converter legs after every active switching cycle. Simulation and practical results validate and confirm the dynamic performance and power quality of the proposed system.

[4] B. N. Alajmi, K. H. Ahmed, G. P. Adam, S. J. Finney, and B. W. Williams, "Modular multilevel inverter with maximum power point tracking for grid connected photovoltaic application," in Industrial Electronics (ISIE), 2011 IEEE International Symposium on, 2011, pp. 2057-2062.

[5] Bader Naser Alajmi, Khaled Hani Ahmed, Grain Philip Adam, Stephen Jon Finney, and Barry Williams," Modular Multilevel Inverter with Maximum Power Point Tracking for Grid Connected Photovoltaic Application," Journal of Energy and Power Engineering, vol. 6, pp. 1680-1687, October 2012.

Abstract- A single-phase modular multilevel inverter based photovoltaic system for grid connection is proposed. This photovoltaic system utilizes two conversion stages; a boost converter for tracking the maximum power point and a modular multilevel inverter used as an interfacing unit. The maximum power point tracking is achieved with a fuzzy logic controller, and the modular multilevel inverter regulates the dc link voltage and synchronizes the grid voltage and current in order to achieve unity power factor operation. The proposed system provides high dynamic performance and power quality injected into the grid. The validity of the proposed system is confirmed by simulations.

[6] G. P. Adam, B. Alajmi, K. H. Ahmed, S. J. Finney, and B. W. Williams, "New flying capacitor multilevel converter," in Industrial Electronics (ISIE), 2011 IEEE International Symposium on, 2011, pp. 335-339.

Abstract-This paper proposes an improved version of conventional flying capacitor multilevel converter known as active flying capacitor converter. The proposed converter replaces the clamping capacitor of the three-level flying capacitor converter by number of series connected half or full bridge cells, and uses these active cells to generate multilevel voltage waveform at converter output. Additionally, this converter enjoys all the features of modular multilevel converters (M2C) such as operation independent of load power factor and modulation index, and can be extended to high number of levels without capacitor voltage balancing problem. Also, it requires reduced number of capacitor to generate the same number of voltage level per phase as M2C; therefore it may have small footprint.